Master's thesis

NTNU
Norwegian University of Science and Technology
Faculty of Engineering
Department of Geoscience and Petroleum

Eirik Nilsen

Groundwater Pressure on a Partially Drained Tunnel Lining

Simulation of the Rock Joint Water Pressure behind the Sprayed Concrete Lining in the Gevingåsen Railway Tunnel, Norway, Using the Finite Element and Distinct Element Methods

Master's thesis in geotechnology
Supervisor: Karl Gunnar Holter
June 2019

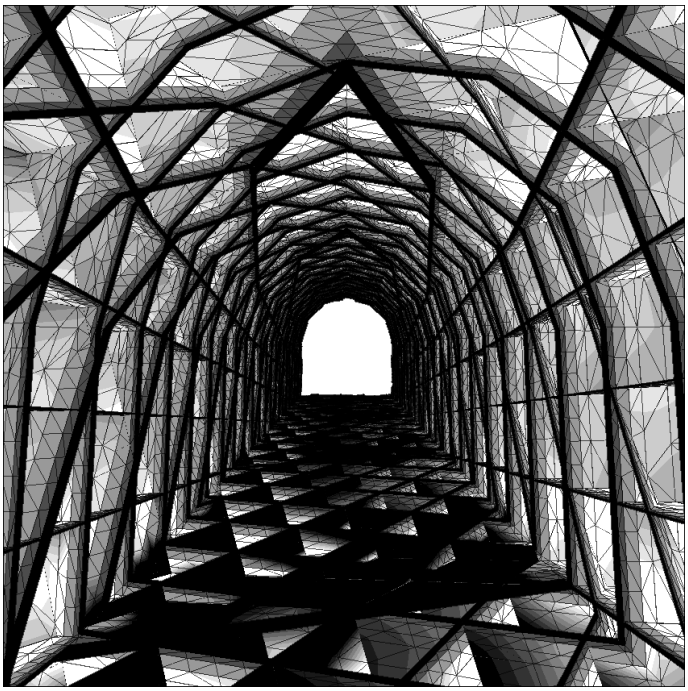

NTNU
Norwegian University of
Science and Technology

Eirik Nilsen

Groundwater Pressure on a Partially Drained Tunnel Lining

Simulation of the Rock Joint Water Pressure behind the Sprayed Concrete Lining in the Gevingåsen Railway Tunnel, Norway, Using the Finite Element and Distinct Element Methods

Master's thesis in geotechnology
Supervisor: Karl Gunnar Holter
June 2019

Norwegian University of Science and Technology
Faculty of Engineering
Department of Geoscience and Petroleum

NTNU
Norwegian University of
Science and Technology

Abstract

One way of controlling the water flowing into a tunnel is by application of an undrained waterproof tunnel lining. A concern during the design of such a lining is the possibility of high groundwater pressures in the rock mass behind it, possibly as high as the hydrostatic pressure. However, if the lining is applied only to the tunnel walls and crown, flow to the drained invert may lead to a reduction of the pressure. This effect might be enhanced by an excavation damage zone (EDZ) with higher hydraulic conductivity than the undisturbed rock mass.

This thesis studies the groundwater pressure in the rock mass surrounding the Gevingåsen tunnel, a drill-and-blast railway tunnel in Trøndelag, Norway. The tunnel is lined in the walls and crown with a sprayed concrete lining (SCL) with waterproof sprayed membrane. The study includes field and laboratory investigations of the conditions in the tunnel, two-dimensional finite element modelling in the software *RS2,* and three-dimensional distinct element modelling in the software *3DEC.* The simulation results are compared to existing measurements of the groundwater pressure behind the SCLs in the Gevingåsen tunnel and at another test site. The construction damage zone (CDZ) is included in the models, and its hydraulic properties are back-calculated using the measured values.

Based on observed water conditions in the Gevingåsen tunnel, the effective hydraulic conductivity of the undisturbed rock mass is estimated to be 1×10^{-8} m/s. This corresponds to a joint hydraulic aperture of approximately 3×10^{-5} m. Without any change in the rock mass hydraulic properties due to the tunnel excavation, the maximum rock joint water pressure immediately behind the partially drained SCL is simulated to be close to 0.5 MPa. This is lower than the hydrostatic pressure of 0.6 MPa, but higher than the measured values. The simulated pressure is lower when hydraulic aperture changes due to mechanical effects (i.e., not blasting directly) are included in the model, as joint normal displacements increase the hydraulic aperture of some natural joints. The maximum joint pressure remaining immediately behind the partially drained SCL is simulated to be in the range 0.3–0.4 MPa when joint normal displacements are allowed to affect the joint hydraulic apertures. However, this is still higher than the measured values.

A hydraulic conductivity increase in the CDZ of between one and two orders of magnitude is necessary to explain the pressures previously measured. This corresponds to a hydraulic aperture increase with a factor 2–4. Such an increase leads to a significant reduction of the simulated joint pressures, and results in a maximum pressure at the excavation boundary of approximately 0.16 MPa. This is in good agreement with the measurements. The simulations also suggest that the virgin stress field, and the type, quantity and time of installation of rock support are among the factors that influence the pressure.

Sammendrag

Én måte å kontrollere vanninnlekkasjen i en tunnel er ved bruk av en udrenert vanntett tunnelkledning. Når en slik kledning prosjekteres må man ta hensyn til muligheten for høye grunnvannstrykk i bergmassen bak kledningen. I verste fall kan trykket være lik det hydrostatiske. Dersom kledningen kun påføres tunnelens vegger og heng kan imidlertid strømning til tunnelens drenerte såle føre til en reduksjon av grunnvannstrykket. Denne effekten kan forsterkes av en sprengningsskadesone med større hydraulisk konduktivitet enn den uforstyrrede bergmassen.

Denne masteroppgaven studerer grunnvannstrykket i bergmassen rundt Gevingåstunnelen, en sprengt jernbanetunnel i Trøndelag, Norge. Tunnelen er vannsikret i vegger og heng med en sprøytebetongkledning med vanntett sprøytet membran. Studien inkluderer felt- og laboratorieundersøkelser av forholdene i tunnelen, todimensjonal endelig elementmodellering i programmet *RS2* og tredimensjonal diskontinuumsmodellering i programmet *3DEC.* Resultatene fra simuleringene sammenlignes med eksisterende målinger av grunnvannstrykket bak den delvis drenerte kledningen, samt målinger fra en annen lokalitet. Sprengningsskadesonen inkluderes i simuleringene, og dens hydrauliske egenskaper tilbakeberegnes.

Basert på observerte vannforhold i Gevingåstunnelen er bergmassens effektive hydrauliske konduktivitet estimert til 1×10^{-8} m/s. Dette tilsvarer en hydraulisk sprekkeåpning på ca. 3×10^{-5} m. Uten noen form for påvirkning fra tunneldrivingen på bergmassens hydrauliske egenskaper, resulterer simuleringene i et maksimalt sprekkevannstrykk bak tunnelkledningen på nærmere 0.5 MPa. Dette er lavere enn det hydrostatiske trykket på 0.6 MPa, men høyere enn hva som er målt. Det simulerte sprekkevannstrykket er lavere når modellen tar hensyn til endringer i sprekkenes hydrauliske åpning som følge av deformasjoner og spenningsendringer i bergmassen. Dette skyldes en økning av den hydrauliske sprekkeåpningen for enkelte naturlige sprekker. Når dette inkluderes, ligger det høyeste sprekkevannstrykket som opptrer bak kledningen i intervallet 0.3–0.4 MPa. Imidlertid er trykkene som er målt i tunnelen enda lavere.

For å oppnå samsvar med de målte grunnvannstrykkene kreves en økning av den hydrauliske konduktiviteten i sprengningsskadesonen på én til to størrelsesordener. Dette tilsvarer en økning i hydraulisk sprekkeåpning med en faktor to til fire. En slik økning av de hydrauliske spekkeåpningene i sprengingsskadesonen fører til en betydelig reduksjon av det simulerte sprekkevannstrykket bak tunnelkledningen. Trykket på kledningen simuleres til å være maksimum ca. 0.16 MPa, noe som stemmer godt overens med målingene. For øvrig indikerer simuleringene at primære bergspenninger, samt type, mengde og installasjonstidspunkt for bergsikring er blant faktorene som påvirker vanntrykket i bergmassen.

Preface

This document constitutes my master's thesis (30 ECTS credits) in engineering geology and rock mechanics. It concludes five years of studies at the Geotechnology programme at the Norwegian University of Science and Technology (NTNU).

Along the way I have depended upon the help of family, friends and mentors. I would like to thank my fellow students and friends for pleasant times and exciting discussions. Also, I need to thank the team at the Technical department of the Infrastructure Construction division at Bane NOR, who has been a collaborating partner for this thesis. Furthermore, I sincerely thank Senior Engineers Gunnar Vistnes and Jon Runar Drotninghaug at the rock mechanical laboratory at NTNU. They supervised the laboratory investigations presented in this thesis with unmatched proficiency. I also want to thank my future colleagues at NGI. NGI provided me with software, an office, and technical guidance whenever needed. Technical support has also been provided by Itasca Consulting Group, Inc.

Finally, I gratefully thank my supervisor, Karl Gunnar Holter, for valuable guidance and infectious excitement.

Eirik Nilsen
Trondheim, Norway
June 2019

Table of Contents

List of Figures xiii
List of Tables xvii
Abbreviations and Symbols xix

1 Introduction 1
1.1 Background 1
1.2 Scope 1
1.3 Outline 2

2 Background and Theory 3
2.1 Waterproofing Systems Used in Norwegian Railway Tunnels 3
2.1.1 Separate Lining Structure of Pre-Cast Concrete Segments 5
2.1.2 Separate Lining Structure with PE Foam Sheets 5
2.1.3 Drained Cast-in-Place Concrete Lining 5
2.1.4 Undrained Sprayed Concrete Lining with Sprayed Membrane 5
2.1.5 Drainage Characteristics of the Waterproofing Systems 6
2.2 The Excavation Damage Zone 6
2.3 Flow in a Rock Mass 8
2.3.1 Matrix Fluid Flow 8
2.3.2 Joint Fluid Flow 10
2.4 Mechanical Behaviour of a Rock Mass 11
2.4.1 Isotropic Linear Elasticity 11
2.4.2 Joint Behaviour and Joint Slip Models 12
2.5 Rock Mass Classification Systems 15
2.5.1 The Geological Strength Index 15
2.5.2 The Q-System 15
2.6 Numerical Modelling Methods 16
2.6.1 The Finite Element Method 16
2.6.2 The Distinct Element Method 17
2.6.3 Solid-Fluid Coupling 17

3 Working Method in This Study 19
3.1 Study of Previous Investigations 19
3.2 Field and Laboratory Investigations 20
3.3 Finite Element Modelling 20
3.4 Distinct Element Modelling 20

4 Review of Previous Investigations 23
4.1 Studies of the In-Situ Stress Field 23
4.2 Investigations of the Hydraulic Properties of the EDZ 24
4.3 Investigations of the Pressure behind Partially Drained SCLs 25
4.3.1 Investigations in the Gevingåsen Tunnel 25
4.3.2 Investigations in the Karmsund Tunnel 26

5 Field and Laboratory Investigations 27
5.1 Field Investigations 27
5.1.1 Bedrock 27
5.1.2 Rock Mass Quality 29

5.1.3 Joint Mapping 30
5.2 Laboratory Investigations 37
5.2.1 General 37
5.2.2 Method 39
5.2.3 Results 42
5.2.4 Analysis and Discussion 47
5.3 Joint Properties Estimated Based on the Investigations 49

6 FINITE ELEMENT MODELLING 51
6.1 Model Setup 51
6.1.1 Geometry 51
6.1.2 Material Properties 52
6.1.3 Back-Calculation of the Hydraulic Conductivity of the CDZ 53
6.1.4 Virgin Stress Field 54
6.1.5 Mesh Setup 55
6.1.6 Boundary Conditions 56
6.1.7 Calculation Stages 56
6.2 Results 57
6.2.1 Verification of the Estimated Effective Hydraulic Conductivity 57
6.2.2 Pore Pressures 57
6.2.3 Induced Stresses 59
6.3 Conclusions 62

7 DISTINCT ELEMENT MODEL SETUP 63
7.1 Overview of Scenarios 63
7.2 Geometry 64
7.2.1 Outer Boundaries 64
7.2.2 Joint Sets 65
7.2.3 Tunnel and CDZ 66
7.2.4 Rock Support 67
7.3 Material Properties 67
7.3.1 Block Properties 67
7.3.2 Joint Properties 69
7.3.3 Rock Support Properties 72
7.4 Virgin Stress Field 72
7.5 Mesh Setup 72
7.6 Boundary Conditions 72
7.7 Calculation Stages 72
7.8 Solid-Fluid Coupling 74
7.9 Measures to Reduce the Calculation Time 74

8 DISTINCT ELEMENT SIMULATION RESULTS 77
8.1 Reference Scenario: No Excavation Damage 77
8.2 Stress Field Scenario 1: Isotropic Virgin Stress Field 79
8.2.1 Scenario 1.1: No CDZ with Increased Hydraulic Apertures 82
8.2.2 Scenario 1.2: Increased Hydraulic Apertures in the CDZ 84
8.3 Stress Field Scenario 2: Anisotropic Virgin Stress Field 86
8.3.1 Scenario 2.1: No CDZ with Increased Hydraulic Apertures 88
8.3.2 Scenario 2.2: Increased Hydraulic Apertures in the CDZ 88

9 DISCUSSION 93
9.1 Comparison between Simulated and Measured Pressures 93
9.2 Comparison between the FE and DE Simulations 94
9.3 Comparison between the Two Virgin Stress Fields 94
9.4 Solid-Fluid Coupling 95
9.5 Representation of the CDZ 95
9.6 Inadequacies of the DE Model 96
9.6.1 Numerical Formulation of Joint Fluid Flow 96
9.6.2 Model Geometry 96
9.6.3 Geochemical Processes 97
9.6.4 Other Uncertainties 97
9.7 Further Work 97

10 CONCLUSIONS 99

REFERENCES 101

APPENDIX A: DATA FROM JOINT MAPPING IN THE FIELD

APPENDIX B: JOINT PROFILES COLLECTED IN THE FIELD

APPENDIX C: POINT LOAD TEST RESULTS

List of Figures

Figure 2.1: Schematic drawing of the waterproofing systems used in Norwegian D&B railway tunnels 4

Figure 2.2: Schematic drawing of the different excavation damage zones surrounding a tunnel 7

Figure 2.3: Effective hydraulic conductivity for different configurations of cells 10

Figure 4.1: Tunnel cross-section showing the location of the piezometers used by Holter et al. (2015) to measure groundwater pressures behind the SCL in the Gevingåsen tunnel 25

Figure 4.2: Groundwater pressures measured by Holter et al. (2015) in boreholes in the Karmsund tunnel.....26

Figure 5.1: Bedrock map of the area around the Gevingåsen tunnel.....28

Figure 5.2: Photo of the rock mass in the niche at chainage 430 of the R1.....28

Figure 5.3: Photo of the rock mass in the niche at chainage 255 of the R1.....29

Figure 5.4: Equal area stereoplot with poles and contours of the mapped joints, and three interpreted joint sets.....31

Figure 5.5: Joint surface (set J1) before (a) and after (b) testing of the Schmidt hammer rebound value. 33

Figure 5.6: Joint surface (set J2) before (a) and after (b) testing of the Schmidt hammer rebound value.....34

Figure 5.7: Joint surface (set J3) before (a) and after (b) testing of the Schmidt hammer rebound value.....35

Figure 5.8: Histograms of normalised rebound values for the three joint sets.....36

Figure 5.9: Blocks collected from the R1 for use in laboratory investigations.....37

Figure 5.10: Representative core specimens used in the laboratory investigations 40

Figure 5.11: The GCTS PLT-100 Point Load Test System, used for point load testing in the laboratory 41

Figure 5.12: The GCTS RTR-4000 Rapid Triaxial Rock Testing System, used for uniaxial compression testing in the laboratory 42

Figure 5.13: Individual value plot of the results from the diametral point load tests....43

Figure 5.14: Individual value plot of the results from the axial point load tests 43

Figure 5.15: Individual value plots of the results from the uniaxial compression tests.....45

Figure 5.16: Stress-strain curves for the uniaxial compression tests 45

Figure 5.17: Photo of specimens 1.1–1.5 (from left to right) after the uniaxial compression tests 46

Figure 5.18: Photo of specimens 4.1–4.4 (from left to right) after the uniaxial compression tests 46

Figure 5.19: Typical mode of failure for axial point load tests on specimens from block 2 47

Figure 6.1: Tunnel geometry in the FE model, including bolts and SCL 52

Figure 6.2: Flow net illustrating the flow towards the tunnel when there is no water control.....58

Figure 6.3: Pore pressure field around the tunnel when the hydraulic conductivity is uniform in the entire model, including the CDZ 58

Figure 6.4: Pore pressure field around the tunnel when the hydraulic conductivities in the CDZ are back-calculated using the pressures reported by Holter et al. (2015) 59

Figure 6.5: Major induced principal total stress for the two stress field scenarios 60

Figure 6.6: Minor induced principal total stress for the two stress field scenarios 61

Figure 7.1: DE model geometry, showing the outer model boundaries and the three joint sets 65

Figure 7.2: Tunnel geometry and rock support in the DE model 66

Figure 7.3: Young's modulus of the damaged rock after excavation of the tunnel.....68

Figure 7.4: Linearisation of the Barton-Bandis slip criterion used to obtain the instantaneous angle of friction and instantaneous cohesion in the Coulomb slip criterion 70

Figure 7.5: Hydraulic apertures in DE model for scenario 1.2 before the final stage ..71

Figure 7.6: Boundary conditions in the DE model.....73

Figure 8.1: Perspective view of the joint pressure at the excavation boundary for the reference scenario without any excavation damage.....78

Figure 8.2: Orthographic view of the joint pressure field for the reference scenario without any excavation damage 78

Figure 8.3: Cross-section showing the water pressure in distinct joints for the reference scenario without any excavation damage 79

Figure 8.4: Cross-section showing a contour plot of the major principal total stress for stress field scenario 1 80

Figure 8.5: Joint hydraulic apertures produced by the DE simulation for scenario 1.1 81

Figure 8.6: Perspective view of the joint pressure at the excavation boundary for scenario 1.1 82

Figure 8.7: Orthographic view of the joint pressure field for scenario 1.1.....83

Figure 8.8: Cross-section showing the water pressure in distinct joints for scenario 1.1 83

Figure 8.9: Perspective view of the joint pressure at the excavation boundary for scenario 1.2 84

Figure 8.10: Orthographic view of the joint pressure field for scenario 1.2.....85

Figure 8.11: Cross-section showing the water pressure in distinct joints for scenario 1.2 85

Figure 8.12: Cross-section showing a contour plot of the major principal total stress for stress field scenario 2 86

Figure 8.13: Joint hydraulic apertures produced by the DE simulation for scenario 2.1 87

Figure 8.14: Perspective view of the joint pressure at the excavation boundary for scenario 2.1 88

Figure 8.15: Orthographic view of the joint pressure field for scenario 2.1.....89

Figure 8.16: Cross-section showing the water pressure in distinct joints for scenario 1.2 89

Figure 8.17: Perspective view of the joint pressure at the excavation boundary for scenario 2.2 90

Figure 8.18: Orthographic view of the joint pressure field for scenario 2.2.....90

Figure 8.19: Cross-section showing the water pressure in distinct joints for scenario 1.2 91

List of Tables

Table 4.1: Descriptive statistics for the hydraulic conductivities measured by Ericsson et al. (2015) in the EDZ at the Äspö HRL 25

Table 4.2: Groundwater pressures measured by Holter et al. (2015) behind the SCL in the Gevingåsen tunnel 26

Table 5.1: Q-parameters for the metasandstone in R1, determined during field investigations 30

Table 5.2: Interpreted joint sets with their mean dip and dip directions.....31

Table 5.3: Descriptive statistics for the normalised Schmidt L hammer rebound values for the three joint sets in the R1 32

Table 5.4: Dimensions and weight of the specimens prepared for the uniaxial compression tests 42

Table 5.5: Summary tabulation of mean $I_{s(50)}$ values for subsamples tested perpendicular ($\perp$) and parallel ($\parallel$) to the main foliation, and the corresponding $I_{a(50)}$ values 43

Table 5.6: Results of the uniaxial compression tests 44

Table 5.7: Representative stiffness and strength properties for intact pieces of the metasandstone in the Gevingåsen tunnel 48

Table 5.8: Joint mechanical properties estimated based on the results from the field and laboratory investigations 49

Table 6.1: Rock mass properties in the FE model.....53

Table 6.2: Rock support properties in the FE model 53

Table 6.3: Hydraulic conductivities in the CDZ, back-calculated using the pressures reported by Holter et al. (2015) 54

Table 6.4: Stress field scenarios for the FE simulations 55

Table 6.5: Analytical solutions for the LDP 57

Table 7.1: Overview of scenarios included in the DE simulations.....64

Table 7.2: Material properties for the blocks of intact rock in the DE model 68

Table 7.3: Young's modulus for the damaged rock in the DE model.....68

Table 7.4: Joint properties in the DE model 70

Table 7.5: Hydraulic apertures in the CDZ in the DE model 71

Abbreviations and Symbols

A	Area
B	Bulk modulus
c	Cohesion
CDZ	Construction damage zone
d	Displacement
D	Disturbance factor
D&B	Drill-and-blast
DE	Discrete element
DFN	Discrete fracture network
d_{max}	Maximum displacement
E	Young's modulus
E_{50}	Tangent Young's modulus at 50 % axial stress level in uniaxial compression
EDZ	Excavation damage zone
EdZ	Excavation-disturbed zone (also called the excavation influence zone, EIZ)
E_i	Young's modulus of intact rock
EIZ	Excavation influence zone (also called the excavation-disturbed zone, EdZ)
E_{rm}	Young's modulus of the rock mass
FE	Finite element
g	Acceleration of gravity
G	Shear modulus
GSI	Geological strength index
h	Hydraulic head
HDZ	Highly damaged zone
HRL	Hard Rock Laboratory
$I_{a(50)}$	Point load strength anisotropy index
$I_{s(50)}$	Point load strength index
ISRM	International Society for Rock Mechanics
J_a	Joint alteration number (Q-system parameter)
JCS	Joint wall compressive strength
JCS_0	Laboratory/test scale joint wall compressive strength
J_n	Joint set number (Q-system parameter)
J_r	Joint roughness number (Q-system parameter)
JRC	Joint roughness coefficient
JRC_0	Laboratory/test scale joint roughness coefficient
J_w	Joint water reduction factor (Q-system parameter)
K	Hydraulic conductivity

K_f	Fracture hydraulic conductivity
K_n	Joint normal stiffness
$K_{n,int.}$	Normal stiffness of interlocked joint
$K_{n,mism.}$	Normal stiffness of mismatched joint
K_{ni}	Initial joint normal stiffness
K_s	Joint shear stiffness
l	Length
L	In situ block scale characteristic length
L_0	Laboratory/test scale characteristic length
LDP	Longitudinal displacement profile
m	Thickness
m_i	Hoek-Brown constant for intact rock
NGU	Geological Survey of Norway
NTNU	Norwegian University of Science and Technology
p	Groundwater pressure
PE	Polyethylene
p_i	Internal pressure
Q	Q-value according to the Q-system for rock mass classification
q	Specific discharge (i.e., flow rate per unit area)
Q	Total flow rate through a given area
q_f	Joint fluid flow (per unit width)
r	Tunnel radius
R	Schmidt hammer rebound value
REV	Representative elementary volume
r_p	Plastic radius
RQD	Rock Quality Designation (Q-system parameter)
s	Joint spacing
SCL	Sprayed concrete lining
SKB	Swedish Nuclear Fuel and Waste Management Co
SRF	Strength Reduction Factor (Q-system parameter)
T	Transmissivity
TBM	Tunnel boring machine
T_f	Fracture transmissivity
u_0	Initial mechanical aperture of joint
UCS	Uniaxial compressive strength
u_h	Hydraulic aperture
u_{h0}	Initial hydraulic aperture
u_n	Joint normal displacement

u_s	Joint shear displacement
V_m	Maximum closure of joint
z	Elevation
γ	Weight density
ϵ	Strain
μ	Dynamic viscosity
ν	Poisson ratio
ν_{50}	Tangent Poisson ratio at 50 % axial stress level in uniaxial compression
ρ	Density
σ	Normal stress
σ'	Effective normal stress
σ_0	Virgin isotropic stress
σ_{ci}	Uniaxial compressive strength of intact rock
τ	Shear stress
τ_{max}	Shear strength
ϕ	Angle of friction
ϕ_b	Basic angle of friction
ϕ_r	Residual angle of friction

1 Introduction

1.1 Background

Control of water inflow is an important challenge during tunnel excavation and in the tunnel's operational phase. One way of providing such control is the application of an undrained tunnel lining. However, the possibility of high groundwater pressures behind such a lining is of concern.

According to the current specification, new Norwegian drill-and-blast (D&B) railway tunnels should be lined with either a cast-in-place concrete lining with a sheet membrane and drainage geotextile, or a sprayed concrete lining (SCL) waterproofed with a sprayed membrane (Bane NOR, 2018b). The cast-in-place concrete lining results in a drained tunnel, while the SCL can be designed as either drained or undrained. This thesis will focus on a D&B tunnel with an undrained waterproof lining in the walls and crown, and a drained invert. This situation will be referred to as *partially drained*. The theoretical maximum groundwater pressure acting on the lining is the hydrostatic pressure given by the elevation of the groundwater table relative to the tunnel. However, the drained invert will likely lead to a certain reduction of the groundwater pressure behind the lining. This effect might be enhanced by a higher hydraulic conductivity in the excavation damage zone (EDZ). Therefore, it might not be necessary to design for the theoretical maximum groundwater pressure.

To investigate the groundwater pressures behind partially drained lining structures, Holter (2014) and Holter et al. (2015) conducted measurements of the groundwater pressure in the rock mass behind SCLs waterproofed with sprayed membrane. The measurements revealed that the groundwater pressure was approximately hydrostatic some metres from the tunnel contour, but significantly lower immediately behind it. These observations suggest that the drainage in the invert might prevent high groundwater pressures from acting on the SCL. If this is true, it might be possible to design slim tunnel lining constructions, not designed for the full hydrostatic pressure. More specifically, partially drained SCLs might in many cases replace cast-in-place concrete linings. This will reduce material consumption, time expenditure, and costs. However, more knowledge about the loads that act on partially drained linings is necessary. As a part of that work, this thesis has been written in collaboration with Bane NOR, the Norwegian state-owned company responsible for the national railway infrastructure in Norway.

1.2 Scope

This thesis investigates, by numerical modelling, the effects of a partially drained lining structure on the groundwater pressure field around a tunnel. As the study is carried out in cooperation with Bane NOR, the thesis will focus on railway tunnels. The effect of the EDZ is of particular interest. Previous numerical modelling studies of the EDZ have largely been concerned with the development of the EDZ, depth prediction, and permeability changes. Different approaches have been used, including continuum models (Hou, 2003, Rutqvist et al., 2009, Perras and Diederichs, 2016), discontinuum models (Poteri and Laitinen, 1999, Fabian et al., 2007, Hudson et al., 2009), and hybrid models (Zhu and Bruhns, 2008, Lisjak et al., 2015, 2016, Huaming et al., 2017). This study uses two-dimensional finite element

modelling in the software *RS2* (Rocscience Inc., 2019) and three-dimensional distinct element modelling in the software *3DEC* (Itasca Consulting Group Inc., 2016a) to simulate the groundwater pressure behind a partially drained tunnel lining. The Gevingåsen railway tunnel in Trøndelag, Norway is used in a case study for this purpose.

The specific objective of the study is to use existing measurements of the groundwater pressure behind the partially drained SCL in the Gevingåsen tunnel to back-calculate the hydraulic properties of the construction damage zone (CDZ). The pressure that would be expected if the hydraulic properties of the rock mass were completely unaffected by the excavation is simulated. Then it is investigated whether the measured pressures can be explained considering only excavation damage that is not caused by blasting directly but rather by stress redistribution and deformations. If such damage alone is not sufficient to explain the measured pressures, it is investigated how large the hydraulic conductivity increase within the CDZ needs to be in order to obtain agreement with the measurements.

The study also briefly examines how variations in the virgin stress field affect the groundwater pressure behind the partially drained SCL. The study is unable to encompass an extensive parametric analysis, as this would not have been possible within the given time frame due to long calculation times in *3DEC*. Consequently, a full discussion of factors that might influence the groundwater pressures behind a partially drained lining lies beyond the scope of this study.

1.3 Outline

The thesis has been divided into ten chapters. Chapter 2 gives an overview of waterproofing systems currently used in Norwegian railway tunnels, defines the EDZ, and reviews relevant theoretical principles. Chapter 3 will then describe the working method used in this study. Next, Chapter 4 reviews the results of selected previous investigations, while Chapter 5 presents field and laboratory investigations performed in this study. Together, Chapters 4 and 5 establish necessary input parameters for the numerical modelling. The remaining part of the thesis deals with the modelling, and proceeds as follows: Chapter 6 presents preliminary finite element modelling, Chapter 7 presents the model setup for the distinct element model, and Chapter 8 presents the results of the distinct element simulations. The results are further discussed in Chapter 9, while Chapter 10 summarises the main findings.

Throughout the thesis, the term *joint pressure* will refer to the water pressure in joints in the rock mass, and also in joints in the distinct element model. The term *pore pressure* will refer to the water pressure in primary pores or in an equivalent continuous porous medium, that is, a continuous medium representing the combined properties of intact rock and joints. *Pore pressure* is, therefore, the term that will be used for the finite element modelling, as this is the established term in finite element programs for geotechnical engineering. The term *groundwater pressure* will be used as a general term that includes joint pressure and/or pore pressure. However, as the study focuses on the conditions in hard rock where the primary porosity is practically negligible, the terms *groundwater pressure* and *joint pressure* will mostly be equivalent, and the porosity of the equivalent porous medium to which the term *pore pressure* applies will represent discontinuities.

2 Background and Theory

In this chapter, some important topics and principles are reviewed to establish the theoretical background. Firstly, the waterproofing systems used in Norwegian railway tunnels are presented. Then, the excavation damage zone is defined. Finally, some theoretical principles governing water flow in a jointed rock mass and the mechanical rock mass behaviour in numerical software are reviewed. Details regarding the implementation of the equations in the software will not be discussed. Rather, only a brief introduction to the numerical methods used in this study is given.

2.1 Waterproofing Systems Used in Norwegian Railway Tunnels

Dripping and running water may damage constructions of concrete or steel, and is, therefore, unfavourable in railway tunnels. A combination of water and frost is particularly unfavourable. Some kind of waterproofing and thermal insulation system is therefore necessary.

The waterproofing systems can be divided into two categories: 1) structures detached from the rock support system, and 2) constructions in direct contact with the rock support. Four different systems are common in Norwegian D&B railway tunnels (Fig. 2.1). These are (Bane NOR, 2018a):

1) Separate drainage and insulation lining structure of pre-cast concrete segments
2) Separate drainage and insulation lining structure of polyethylene (PE) foam sheets
3) Cast-in-place concrete lining with sheet membrane and drainage geotextile
4) Sprayed concrete lining (SCL) with sprayed waterproofing membrane

The former two are detached constructions, while the latter two are in direct contact with, and may be part of, the permanent rock support.

Traditionally, Norwegian rail and road tunnels have been constructed with detached waterproofing and thermal insulation systems. This makes the rock support and the inner waterproofing system functionally separate. The rock support, commonly consisting of fibre-reinforced sprayed concrete and rock bolts designed according to the Q-system (Barton et al., 1974, Grimstad et al., 2002), provides the geomechanical stability, while the separate inner lining provides the waterproofing and thermal insulation.

According to Bane NOR's current specifications (Bane NOR, 2018b), the detached waterproofing constructions are not accepted anymore. The main reason is the need for extensive maintenance. Therefore, in new D&B railway tunnels the waterproofing system will consist of either a cast-in-place concrete lining with sheet membrane and drainage geotextile or an undrained SCL with sprayed waterproofing membrane. As a side note, TBM tunnels may be waterproofed with concrete segmental linings, making a third accepted waterproofing system in new railway tunnels in Norway. Below, the waterproofing systems commonly employed in Norwegian D&B railway tunnels are briefly presented, including, for completeness, the no longer accepted detached systems.

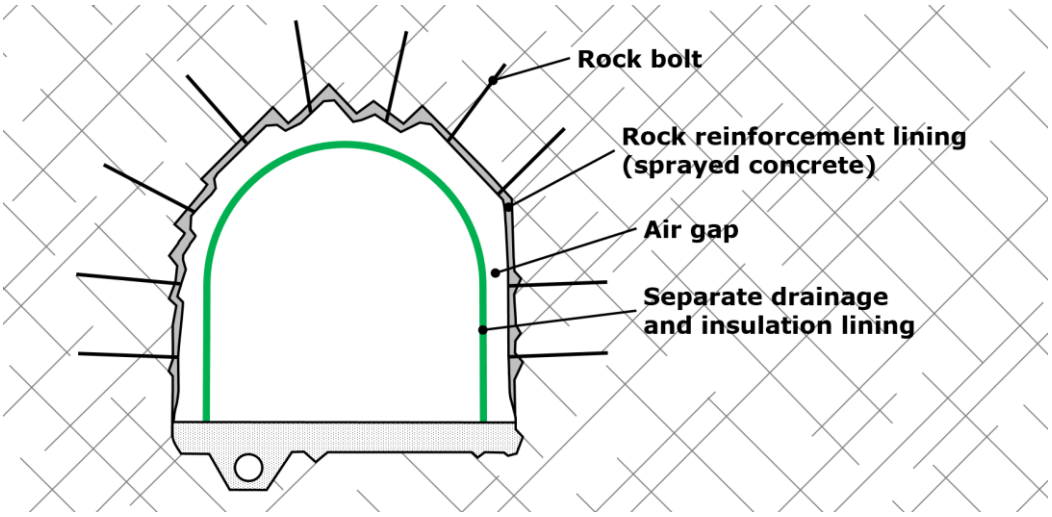

a) Separate drainage and insulation lining

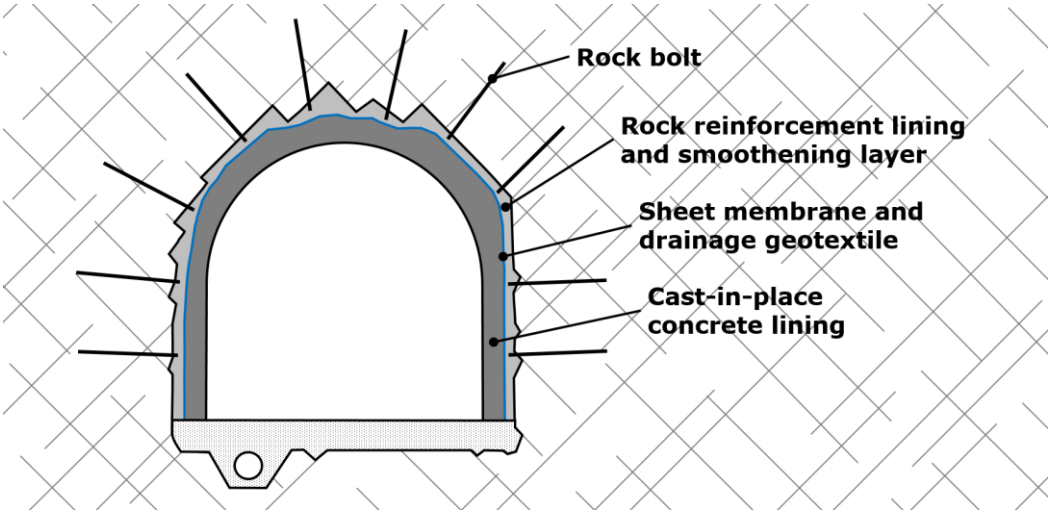

b) Cast-in-place concrete lining

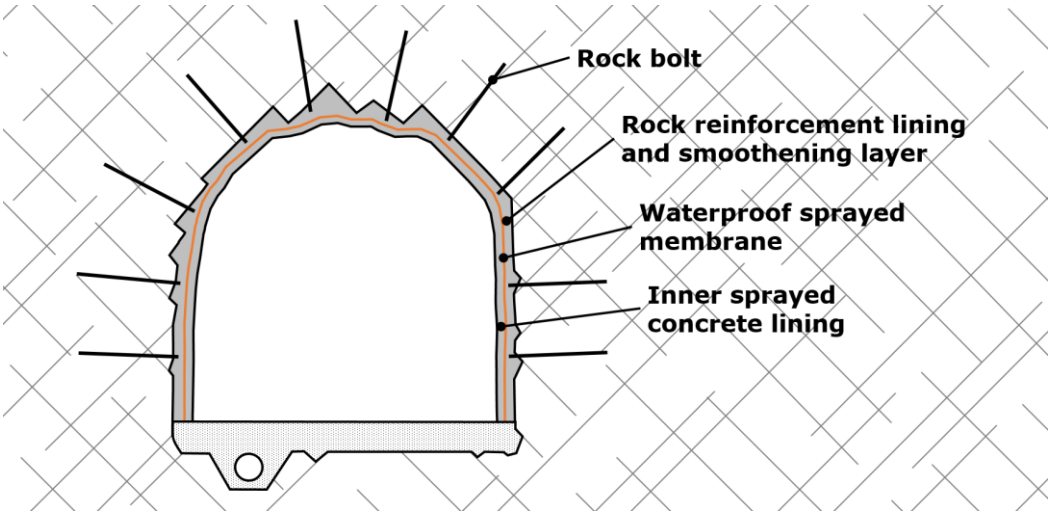

c) Partially drained SCL waterproofed with sprayed membrane

Figure 2.1: Schematic drawing of the waterproofing systems used in Norwegian D&B railway tunnels. The systems are: a) separate lining (green) of either pre-cast concrete segments or PE foam sheets and sprayed concrete, b) cast-in-place concrete lining (dark grey) with sheet membrane and drainage geotextile (blue), and c) SCL waterproofed with sprayed membrane (orange).

2.1.1 Separate Lining Structure of Pre-Cast Concrete Segments

The drainage and insulation structure consisting of pre-cast concrete segments is a detached structure, mounted to the rock mass by bolts. Between the segments and the rock, there is an air gap (thickness of decimetres to more than 1 m). Waterproofing is achieved by a membrane on the back of the segments, along with isolation for frost proofing. Due to the mechanical strength of the concrete segments, there is little need for inspections behind the lining during the tunnel's operational phase. However, some maintenance is necessary. Furthermore, the elements are bulky, which makes the construction process challenging. Hydraulically, this system is drained, and there is zero groundwater pressure at the tunnel contour.

2.1.2 Separate Lining Structure with PE Foam Sheets

The drainage and insulation system based on PE foam sheets is also a detached structure mounted to the rock mass by bolts. This system consists of PE foam sheets coated by a layer of sprayed concrete reinforced with wire mesh. The PE foam sheets provide water and frost proofing, while the sprayed concrete is necessary for fire protection. This system is practical during construction. However, the PE foam is highly flammable. Therefore, there are strict requirements regarding the installation of the sprayed concrete layer. Additionally, this system requires extensive maintenance, and its lifetime is uncertain. Identically to the lining structure of pre-cast concrete segments, the structure with PE foam sheets is drained, with zero groundwater pressure at the contour.

2.1.3 Drained Cast-in-Place Concrete Lining

The cast-in-place concrete lining system is in direct contact with the rock support, with only a sheet membrane and a drainage geotextile between the cast-in-place concrete and the smoothened rock support. The construction of this lining is more costly than the systems above, and the contour quality needs to be good in order to reduce the amount of smoothening necessary before installation of the membrane. In return the lining is very reliable. The need for maintenance is minimal. An additional advantage is that the lining can be part of the permanent rock support. According to the current specifications, the concrete lining should have a thickness of minimum 300 mm. As the sheet membrane and drainage geotextile allow water flow, this structure creates a drained system with zero groundwater pressure behind the lining.

2.1.4 Undrained Sprayed Concrete Lining with Sprayed Membrane

Waterproofing by sprayed membrane integrated in an SCL is a relatively new solution for waterproofing of tunnels. In Norway this system has been used in the Gevingåsen tunnel and the Holmestrand tunnel (Bane NOR, 2018a). The system is in direct contact with the rock mass, and consists of a layer of sprayed concrete for smoothening, a copolymer-based layer of spayed membrane, and finally another layer of sprayed concrete. The membrane bonds mechanically to the sprayed concrete on either side, thus creating a continuous waterproof structure. The advantage of this system is the flexibility during construction, as well as easy maintenance. However, problems arise in tunnels with severe leakages, as these need to be temporarily controlled during application of the membrane. Also, the membrane may be damaged by repeated cycles of severe freezing. This problem may be overcome either by using a thicker layer of sprayed concrete on top of the membrane, or by using a mortar with lower thermal conductivity. The sprayed waterproofing membrane does not allow water to flow along the tunnel lining. Therefore, in its basic form, without any measures for drainage embedded in the lining, this waterproofing system will be either undrained or partially drained, depending on whether the lining is applied to the entire

tunnel contour or only to the walls and crown. The completely undrained system will be subject to the full static groundwater pressure, while the partially drained system will allow water to flow into the tunnel through the drained invert. This may lead to a certain reduction of the groundwater pressure.

2.1.5 Drainage Characteristics of the Waterproofing Systems

The drainage characteristics of the four waterproofing systems are repeated here, to highlight the difference between them in this regard:

- Detached structures, whether they consist of pre-cast concrete segments or PE foam sheets, give a hydraulically drained system. There will be zero groundwater pressure at the tunnel contour.
- Cast-in-place concrete linings with sheet membrane and drainage geotextile are also drained, with no groundwater pressure behind the lining.
- SCLs with waterproof sprayed membrane are, in the basic form, either undrained or partially drained. When the lining is only applied to the walls and crown, there will be a flow of water into the tunnel through the invert. This results in zero groundwater pressure in the invert, but an unknown, non-zero pressure behind the lining.

The system with undrained SCL in the walls and crown and drained invert is the one that will be studied in this thesis. With this system, water inflow through the tunnel invert is allowed, but the amount may be controlled by pre-excavation grouting.

2.2 The Excavation Damage Zone

During excavation of tunnels and caverns in rock, the rock mass surrounding the excavation may be adversely affected with respect to, for example, fracture density, tightness and interconnectivity. The mechanisms leading to excavation damage can be categorised as follows (Rutqvist et al., 2009):

- Micro and macro fracturing due to increased deviatoric stress.
- Opening of existing fractures due to decreased joint normal stress.
- Elastic compression or expansion of the primary pore volume due to changes in mean stress.
- Damage from drilling and blasting.

The effects of the excavation decrease when moving outward from the excavation contour. Undisturbed conditions are encountered at a distance where the excavation no longer has any influence.

A traditional way of describing the damage zone surrounding an excavation involves distinguishing between an excavation damage zone (EDZ) and an excavation-disturbed zone (EdZ) (e.g., Martino and Chandler, 2004, Tsang et al., 2005, Ericsson et al., 2015). Tsang et al. (2005) define the EDZ as the "zone in which hydromechanical and geochemical modifications induce significant changes in flow and transport properties", while the EdZ is defined as the "zone with hydromechanical and geochemical modifications, without major changes in flow and transport properties".

Other authors use a more finely divided set of terms (Fig. 2.2). Harrison and Hudson (2000) distinguish between damage caused directly by the excavation works and damage that is independent of the excavation method. Following the terminology used by Perras and Diederichs (2016), the former results in a zone called the construction damage zone (CDZ)

and might, for example, comprise fractures generated by blasting. The extent and characteristics of the CDZ are dependent upon the excavation method. Damage that is not directly caused by the excavation works is due to stress redistribution and deformations in the rock mass. It is, therefore, dependent upon the geometry of the tunnel or cavern, but independent of the excavation method. Among the damage zones that are independent of the excavation method, the highly damaged zone (HDZ) is closest to the excavation surface. The HDZ is characterised by damage in the form of macro-scale fractures. The hydraulic conductivity in this zone is generally higher than in the undisturbed rock; often by several orders of magnitude (Bossart et al., 2002, Ericsson et al., 2015). Outside the HDZ comes the EDZ, characterised by micro-scale crack damage. Finally, as before, comes the EdZ. Perras and Diederichs (2016) call this zone the excavation influence zone (EIZ), to avoid confusion between the EDZ and the EdZ. The EIZ/EdZ suffers elastic strains only. In this thesis the term *EDZ* will generally be used as a collective term that includes the CDZ, HDZ, and EDZ. This in conformity with most literature. The more specific terms used by Perras and Diederichs (2016) and others are used when necessary.

The EDZ has been studied since the 1980s, and its hydraulic properties have been a topic of primary interest. Several studies have shown that the hydraulic conductivity of the EDZ is significantly higher than that of the undisturbed rock mass (Chandler et al., 1996, Bossart et al., 2002, Bäckblom, 2008, Ericsson et al., 2015, Tveit, 2018). Whether or not the EDZ is continuous is, however, a topic under debate. Olsson et al. (2009) investigated the fracturing in blocks sampled from the EDZ around a tunnel at the Äspö Hard Rock Laboratory (HRL). Their main conclusions are: 1) that there is no evidence of a continuous network of blast-induced fractures, 2) that the blast-induced fractures are influenced strongly by natural fractures, and 3) that the longer natural fractures control the water flow. Similarly, Ericsson et al. (2015), in a study of the same area, conclude that the interconnectivity between the induced fractures is limited, with transmissive areas no longer than 7 m. Chandler et al. (1996), on the other hand, conclude that the connected hydraulic conductivity of the EDZ at the Underground Research Laboratory in Canada is at least two orders of magnitude higher than that of the undisturbed rock mass.

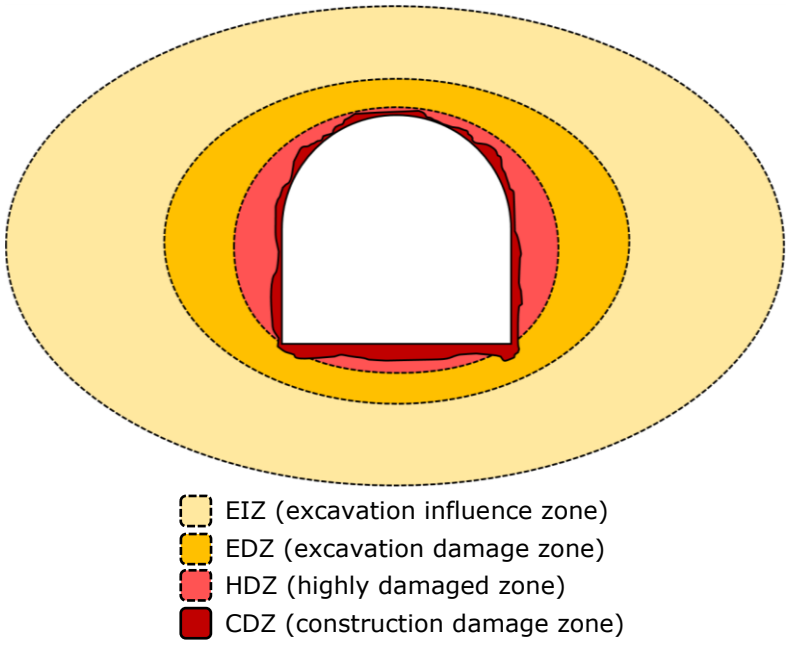

Figure 2.2: Schematic drawing of the different excavation damage zones surrounding a tunnel. The shape and size of the different zones will vary from case to case.

2.3 Flow in a Rock Mass

In general, a rock mass consists of blocks or fragments of intact rock separated by discontinuities such as joints. Therefore, the porosity of a rock mass can be divided into two categories: 1) primary porosity, and 2) secondary porosity. Primary porosity is the porosity of the intact rock, originating from its formation. One example of primary porosity is the pore space between individual grains in a sandstone. The secondary porosity, on the other hand, consists secondary features, created not during the formation of the rock but during later processes. Secondary porosity can, for example, be joints or dissolution features.

The Norwegian mainland is a typical hard rock province dominated by crystalline rocks. Intact pieces of most of these rocks can be considered impermeable for most practical purposes. Water transport will, therefore, mainly take place in the fractures. There exist, of course, rocks that have significant permeability also when intact, for example, highly porous sedimentary rocks and some types of volcanic rocks. In Norway, the Brumunddal sandstone is one example.

The two types of porosity calls for two different approaches when it comes to describing and modelling flow. On one hand, there is the flow through intact rock, which is best described by a continuum approach where the rock is considered a three-dimensional continuum. On the other hand, flow through a single joint is not well described by such an approach. Joint fluid flow is better described as two-dimensional. *3DEC* supports both types of flow, and denotes them matrix fluid flow and joint fluid flow, respectively. These terms are adopted here. However, it should be kept in mind that matrix fluid flow (i.e., flow in a continuum) might also be used to describe flow through a jointed medium, if the scale of the problem is sufficiently large. In such a case the jointed medium is treated as an equivalent continuum. This is the approach that must be used when a jointed rock mass with joint fluid flow as the dominating mode of fluid transport, is modelled in a continuum software such as *RS2*. Some basic equations for matrix fluid flow and joint fluid flow are presented below.

2.3.1 Matrix Fluid Flow

2.3.1.1 Darcy's law

Laminar steady state flow of a single-phase incompressible fluid through a continuous porous medium was found by Darcy (1856) to be proportional to the gradient of the hydraulic head h. This is expressed by Darcy's law:

$$q = \frac{Q}{A} = -K\frac{dh}{dl} \tag{2.1}$$

where q is the flow per unit area, called the specific discharge. The proportionality constant K, expressing how easily a fluid flows through the porous medium, is called the hydraulic conductivity, and dh/dl is the hydraulic gradient in the direction of flow, that is, the change in hydraulic head per unit length. The hydraulic head is given by:

$$h = \frac{p}{\rho g} + z \tag{2.2}$$

where p is the pressure, ρ is the density of the fluid, g is the acceleration of gravity, and z is the elevation above some reference level. Equation (2.2) illustrates that the hydraulic head is the sum of two terms: the pressure head and the elevation head, representing the pressure energy and the potential energy respectively. Kinetic energy is neglected as the velocity of the flow will often be of a magnitude that makes the kinetic energy negligible.

Darcy's law can also be expressed on vector form:

$$\boldsymbol{q} = -K\nabla h \tag{2.3}$$

where $\boldsymbol{q}$ is the flux vector, and ∇h is the gradient of the hydraulic head field.

A quantity related to the hydraulic conductivity, is the transmissivity. The transmissivity expresses the amount of water that can flow through a unit width of an aquifer along its entire thickness. In other words, whereas the hydraulic conductivity solely describes how easily a fluid can flow through a porous medium, the transmissivity also includes the thickness m of the flow area:

$$T = Km \tag{2.4}$$

2.3.1.2 The continuity equation and the Laplace equation

Another important equation for stationary seepage is the continuity equation. This equation is a conservation law, stating that there can be no accumulation of water in any element, that is, the amount of flow into an element must be equal to the flow out of the element. The continuity equation can be written as follows:

$$\nabla \cdot \mathbf{q} = 0 \tag{2.5}$$

where $\nabla \cdot \boldsymbol{q}$ is the divergence of the flux vector $\boldsymbol{q}$.

Combining Darcy's law and the continuity equation (i.e., Eqs. (2.3) and (2.5)), the Laplace equation describing isotropic seepage is obtained:

$$\nabla^2 h = 0 \tag{2.6}$$

Equation (2.6) is valid for laminar steady state flow of an incompressible fluid through an isotropic continuous medium. In principle, this is the equation that must be solved by the numerical software in order to find the flow and pore pressure fields resulting from a set of given flow boundary conditions.

2.3.1.3 Flow in an equivalent continuum

On a sufficiently large scale, a jointed rock mass may also modelled by the continuum approach, even though flow in fractures may be the dominant mode of fluid transport. The rock mass is then treated as an equivalent continuum, characterised by an effective hydraulic conductivity. The effective hydraulic conductivity represents the properties of the entire rock mass, taking into account both the intact rock and the discontinuities. When the rock mass is considered an equivalent continuum, the basic equations outlined above (i.e., Darcy's law and the continuity equation) are applicable. Determining the effective hydraulic conductivity may include statistical treatment of data from injection tests (Fransson, 2002, Gustafson and Fransson, 2005, Gustafson, 2009).

One approach for calculating the effective hydraulic conductivity involves dividing the rock mass into a grid of cells, assigning a hydraulic conductivity to each cell, and calculating the mean for the rock mass using the appropriate equation. Palmström and Stille (2015) summarise equations for the effective hydraulic conductivity for different flow regimes (Fig. 2.3). For one-dimensional flow through a parallel configuration of cells the effective hydraulic conductivity is equal to the arithmetic mean of the hydraulic conductivities of the cells. For one-dimensional flow through a series of cells, on the other hand, the effective hydraulic conductivity is equal to the harmonic mean, while for two-dimensional flow the effective hydraulic conductivity is equal to the geometric mean. Equations have also been developed for a three-dimensional network of cells (e.g., Matheron, 1967).

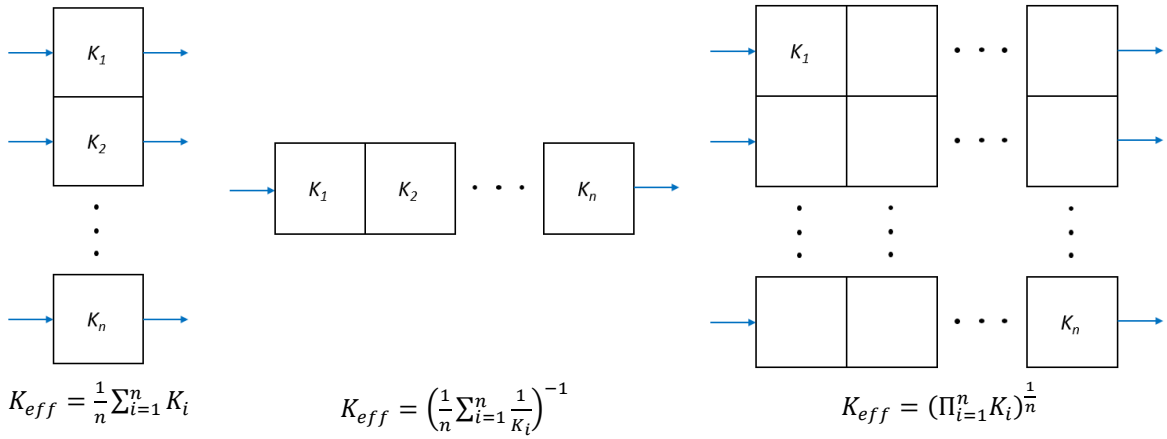

Figure 2.3: Effective hydraulic conductivity for different configurations of cells. For a 1D parallel (a) the effective hydraulic conductivity is the arithmetic mean, for a 1D series (b) it is the harmonic mean, and for 2D flow (c) it is the geometric mean. Flow is indicated with blue arrows. K_i denotes the hydraulic conductivity of cell i, while n is the total number of cells.

As mentioned above, the equivalent continuum approach is only valid at a sufficiently large scale. More precisely, this approach is only valid if the characteristic length of the problem considered is large compared to the dimensions of the representative elementary volume (REV) of the rock mass. The REV is defined as the smallest volume of rock mass that has properties that will not change with small changes in volume or position (Furbish, 1996, Odling, 1997). The size of the REV has been studied by many authors (e.g., Kulatilake and Panda, 2000, Chen et al., 2008, Esmaieli et al., 2010, Zhang et al., 2012, Rong et al., 2013, Zhang et al., 2013, Song et al., 2017). Often it is found to be in the range of some tens of metres, but this will vary. Some of the most important factors determining the size of the REV seem to be fracture spacing and persistence, the number of joint sets, and the volumetric fracture density (the area of fracture per unit volume of rock mass). Generally, the size of the REV is smaller for a heavily fractured rock mass than for a rock mass with a low fracture density.

2.3.2 Joint Fluid Flow

Flow through an open joint with no infilling can be considered two-dimensional. Such flow is described by similar properties as matrix fluid flow, that is, transmissivity and hydraulic conductivity, but now expressing joint properties. Consider the flow q_f per unit width. This flow is given by an equation similar to Darcy's law:

$$q_f = -T_f \frac{dh}{dl} \tag{2.7}$$

where T_f is called the fracture transmissivity. A hydraulic conductivity for the fracture can also be defined. Analogous to Eq. (2.4), the fracture hydraulic conductivity is defined as:

$$K_f = \frac{T_f}{u_h} \tag{2.8}$$

where u_h is a quantity called the hydraulic aperture of the fracture. The hydraulic aperture is generally not equal to the mechanical aperture, due to the roughness of the joint walls. Rather, it is a mathematical quantity, used in the so-called parallel plate model. This model considers the fracture as an infinite slit between smooth parallel walls. The hydraulic aperture is the separation between the walls.

The parallel plate model has the advantage of being mathematically simple. The model considers flow between parallel, infinite, and perfectly smooth plates. The flow is assumed to be stationary, laminar, and incompressible. For a Newtonian fluid under such conditions, the Navier-Stokes equation simplifies to an equation describing so-called plane Poiseuille flow (Huitt, 1956, Snow, 1965, Louis, 1969, Witherspoon et al., 1980):

$$q_f = -\frac{\rho g}{\mu}\frac{u_h^3}{12}\frac{dh}{dl} \tag{2.9}$$

where μ is the dynamic viscosity of the fluid.

Combining Eqs. (2.7) and (2.9), the equation known as the cubic law is obtained. This law states that the fracture transmissivity is directly proportional to the cube of the hydraulic aperture:

$$T_f = \frac{\rho g}{\mu}\frac{u_h^3}{12} \tag{2.10}$$

The proportionality with the cube of the hydraulic aperture makes the aperture the most important parameter determining the amount of joint fluid flow.

Despite that the parallel plate model contains simplifications, it is important not only conceptually, but also for practical applications. For example, it can be used for calculating the joint fluid flow in numerical software. Joint fluid flow in *3DEC* is based on this model. The joints are assigned a hydraulic aperture that may change in response to the changes in the normal stress acting on the joint. The hydraulic aperture is given by:

$$u_h = u_{h0} + \Delta u_n \tag{2.11}$$

where u_{h0} is the joint hydraulic aperture at the initial joint normal stress, and Δu_n is the joint normal displacement. The joint normal displacement is determined by the joint normal stiffness and the change in joint normal stress. In the *3DEC*, the minimum and maximum hydraulic apertures might also be specified. Beyond these limits, mechanical deformations do not lead to any change in the hydraulic aperture.

2.4 Mechanical Behaviour of a Rock Mass

For numerical modelling purposes, intact rock and/or the rock mass are usually described as either elastic or elastoplastic. Elastoplastic material models combine elastic and plastic behaviour, with a failure/yield criterion defining the transition. Plastic behaviour of the bulk materials is not considered in the numerical simulations in this study, for the reason that the extent of failure is minimal for the studied case. Consequently, the mechanical behaviours of the intact rock in the DE model and the rock mass in the FE model are governed by elasticity, the concepts of which are presented briefly below. Yielding and a yield criterion are, however, included in the constitutive model used for the joints in the DE model.

2.4.1 Isotropic Linear Elasticity

The isotropic linear elastic model is the one that will be used in the modelling presented in this thesis. The isotropic linear elastic model describes continuous materials that are isotropic and have a linear stress-strain behaviour with no hysteresis. For isotropic linear elastic materials the stress increases linearly and reversibly with strain according to Hooke's law:

$$\Delta\sigma_{ij} = 2G\Delta\epsilon_{ij} + \left(B - \frac{2}{3}G\right)\Delta\epsilon_{kk}\delta_{ij} \tag{2.12}$$

where $\Delta\sigma_{ij}$ is stress increment corresponding to the strain increments $\Delta\epsilon_{ij}$ and $\Delta\epsilon_{kk}$, B is the bulk modulus of the material, and G is the shear modulus. δ_{ij} is the Kronecker delta, which is equal to 1 for $i = j$ and equal to 0 for $i \neq j$. B is used for the bulk modulus instead of the more commonly used symbol K to avoid confusion with the hydraulic conductivity. The indices $i, j, k \in \{1, 2, 3\}$ refer to three orthogonal directions in space. For $i = j$, σ_{ij} is the normal stress in the i-direction, while for $i \neq j$, it is the shear stress acting in the j-direction on a plane with normal vector pointing in the i-direction. Similarly, for $i = j$, ϵ_{ij} is the normal strain in the i-direction. Otherwise, it is the shear strain between i-oriented and j-oriented planes. ϵ_{kk} is the normal strain in the k-direction.

The two elastic moduli B and G are the only parameters that are needed to describe the deformation behaviour of an isotropic linear elastic material, in response to a given increment in stress. The deformation behaviour can also be described by any other pair of elastic moduli, for example, the Young's modulus E and the Poisson ratio ν, which are commonly encountered in rock engineering literature. In terms of B and G, these moduli are given by:

$$E = \frac{9BG}{3B + G} \tag{2.13}$$

$$\nu = \frac{3B - 2G}{2(3B + G)} \tag{2.14}$$

2.4.1.1 Rock mass deformation modulus

Hoek and Diederichs (2006) propose a method for estimating the Young's modulus E_{rm} of a rock mass. They suggest the following equation, known as the generalised Hoek-Diederichs equation:

$$E_{rm} = E_i \left(0.02 + \frac{1 - \frac{D}{2}}{1 + \exp\left[\frac{60 + 15D - \mathrm{GSI}}{11}\right]} \right) \tag{2.15}$$

where E_i is the Young's modulus of the intact rock, *D* is the disturbance factor, and the GSI is the geological strength index (Section 2.5.1).

The disturbance factor describes the disturbance of the rock mass due to excavation damage. This factor was introduced in the 2002–edition of the Hoek-Brown failure criterion (Hoek et al., 2002). The factor applies to the EDZ, and varies between zero for no disturbance, and one for very disturbed rock mass. A value of zero might be achieved by excellent quality control blasting or excavation by road header or TBM, while a value of one may, for example, result from poor control of blasting during tunnel excavation or production blasting in a mine.

2.4.2 Joint Behaviour and Joint Slip Models

The stress state at which slip along a joint in the rock mass occurs can be described by a joint slip criterion. One of the slip criteria featured in *3DEC* is the Coulomb criterion. The Coulomb slip criterion is the one that has been used in the DE modelling in this study. The Barton-Bandis criterion, another slip criterion that is widely used in rock engineering, is used indirectly, as parameters in this criterion have been used to arrive at parameters in the Coulomb criterion.

2.4.2.1 The Coulomb slip model

The Coulomb slip model is the basic joint constitutive law featured in *3DEC*. In the elastic range the behaviour of the joint is governed by the joint normal stiffness K_n and the joint shear stiffness K_s. These stiffness parameters determine the normal displacement u_n and the shear displacement u_s resulting from changes in, respectively, the effective normal stress σ' and the shear stress τ:

$$d\sigma' = -K_n du_n \tag{2.16}$$

$$d\tau_i = -K_s du_{s,i} \tag{2.17}$$

where index i indicates the component of the shear stress and the shear displacement. Note that the effective normal stress σ' is defined as the total stress σ minus the fluid pressure p:

$$\sigma' = \sigma - p \tag{2.18}$$

The joint will deform according to Eqs. (2.16) and (2.17) until a state of failure is reached. The tensile normal stress is limited by the joint tensile strength, which is a constant. If the joint normal stress exceeds this value in tension, failure by separation will occur. The maximum shear stress, on the other hand, is described by the Coulomb slip criterion. The Coulomb slip criterion can be written as follows:

$$\tau_{max} = c + \sigma' \tan \phi \tag{2.19}$$

where c and ϕ are respectively the cohesive strength and the angle of friction of the discontinuity. If the shear stress on the joint exceeds τ_{max}, shear failure will occur. The cohesion should be regarded as a curve fitting parameter, describing the intercept on the τ-axis. It might be a result of true cohesion created by cementation of the discontinuity surfaces, or it might be related to the surface roughness and thereby not a true cohesion in the mechanical sense. After failure, the strength parameters are reduced to residual values. The residual cohesion is often assumed to be zero.

2.4.2.2 The Barton-Bandis slip model

The Barton-Bandis slip model (Barton and Bandis, 1990) is popular in rock engineering as an alternative to the Coulomb slip model. The main difference between the two models is that whereas in the Coulomb slip criterion the shear strength increases linearly with the joint normal stress, the Barton-Bandis slip criterion is curvilinear.

At high normal stresses, the strength of the intact material in a discontinuity wall may be exceeded. The result may be that the surface roughness of the discontinuity is destroyed. Therefore, a strength criterion for discontinuities should depend upon the strength of the intact material as well as the friction properties of the discontinuity surfaces. It is expected that high normal stresses should lead to a lower angle of friction due to failure of the intact rock material. Barton (1973, 1976) and Barton and Choubey (1977) studied joint strength data and arrive at the following failure criterion that describes such behaviour in the form of a non-linear slip criterion:

$$\tau_{max} = \sigma' \tan\left(\phi_r + \mathrm{JRC} \log_{10}\left[\frac{\mathrm{JCS}}{\sigma'}\right]\right) \tag{2.20}$$

where ϕ_r is the residual angle of friction, JRC is the joint roughness coefficient and JCS is the joint wall compressive strength. Equation (2.20) is not valid for $\sigma' = 0$. Also, it has no practical meaning for $\phi_r + \mathrm{JRC} \log_{10}[\mathrm{JCS}/\sigma'] > 70°$ (which gives a lower limit for σ') and for $\sigma' \geq$ JCS (upper limit).

There are different methods for estimating the JRC and the JCS. In this thesis the JRC will be determined by comparison with standard profiles found in the paper by Barton and Choubey (1977), and the JCS will be determined by correlation with the Schmidt hammer rebound value using the method proposed by Barton (1978). The residual angle of friction may be determined by a combination of tilt tests to determine the basic angle of friction ϕ_b of an unweathered surface, and Schmidt hammer rebound measurements to adjust this value to ϕ_r for the weathered surface (Barton and Choubey, 1977). In this thesis, the residual angle of friction is determined using Schmidt hammer rebound values, but ϕ_b is obtained from tables, rather than from tilt tests.

When the JRC and the JCS are determined by the methods outlined above, the resulting values may not be directly applicable to the scale of in situ blocks. The JRC and the JCS must then be corrected in order to be relevant for the problem at hand. Barton and Bandis (1982) propose the following equations for scale correction of the JRC and JCS:

$$\mathrm{JRC} = \mathrm{JRC}_0 \left(\frac{L}{L_0}\right)^{-0.02\mathrm{JRC}_0} \tag{2.21}$$

$$\mathrm{JCS} = \mathrm{JCS}_0 \left(\frac{L}{L_0}\right)^{-0.03\mathrm{JRC}_0} \tag{2.22}$$

where parameters with subscript 0 refers to the laboratory/test scale L_0, and parameters without subscript applies to the in situ block scale L.

In addition to the slip criterion, the Barton-Bandis model includes guidelines for estimating the joint normal stiffness and the joint shear stiffness when the JRC and the JCS are known. The tangent joint normal stiffness $K_{n,int.}$ of interlocked joints can be estimated by the equation proposed by Bandis et al. (1983):

$$K_{n,int.} = K_{ni}\left[1 - \frac{\sigma'}{V_m K_{ni} + \sigma'}\right]^{-2} \tag{2.23}$$

where K_{ni} is the initial joint normal stiffness and V_m is the maximum closure. These parameters can be estimated based on the JRC_0 and the JCS_0. Laboratory scale values are used because small-scale roughness is most critical in controlling normal stiffness. The normal stiffness is, therefore, not scale-dependent. K_{ni} and V_m for the first cycle of loading are calculated by the following equations:

$$K_{ni} = -7.15 + 1.75\mathrm{JRC}_0 + 0.02\left(\frac{\mathrm{JCS}_0}{u_0}\right) \tag{2.24}$$

$$V_m = -0.296 - 0.0056\mathrm{JRC}_0 + 2.241\left(\frac{\mathrm{JCS}_0}{u_0}\right)^{-0.245} \tag{2.25}$$

$$u_0 = \frac{\mathrm{JRC}_0}{5}\left(0.2\frac{\sigma_{ci}}{\mathrm{JCS}_0} - 0.1\right) \tag{2.26}$$

where u_0 is the initial mechanical aperture (in mm) under self-weight stress (~1 kPa). Equation (2.24) gives the initial normal stiffness in MPa/mm, while Eq. (2.25) gives maximum closure V_m in mm. Both equations apply to the first loading cycle. For subsequent loading cycles the coefficients in Eqs. (2.24) and (2.25) are different.

Experience shows that the normal stiffness $K_{n,mism.}$ of mismatched joints is lower than that of a corresponding interlocked joint. Bandis et al. (1983) propose the following equation for estimating the ratio between the two:

$$\frac{K_{n,int.}}{K_{n,mism.}} = 2 + \frac{\mathrm{JRC}_0 \times \mathrm{JCS}_0 \times \sigma'}{2500} \tag{2.27}$$

In contrast to the normal stiffness, experience shows that the shear stiffness of a joint have a distinct size dependency (Barton, 1982). Barton and Bandis (1982) propose the following equation for estimating peak shear stiffness K_s of a joint:

$$K_s = \frac{\sigma' \tan\left[\mathrm{JRC}\log\left(\frac{\mathrm{JCS}}{\sigma'}\right) + \phi_r\right]}{\frac{L}{500}\left(\frac{\mathrm{JRC}}{L}\right)^{0.33}} \tag{2.28}$$

where K_s will have units MPa/m if σ' is given in MPa, and L is given in metres. Equations (2.21)–(2.28) will all be used to calculate input parameters for the numerical distinct element modelling presented in this thesis.

2.5 Rock Mass Classification Systems

Rock mass classification systems are useful for a number of purposes ranging from general description of geological conditions to performing calculations and making design decisions. One example of a rock mass classification system is the geological strength index (GSI), which, as seen above, can be used to estimate the rock mass Young's modulus. Another commonly used rock mass classification system that will be used in this thesis is the Q-system.

2.5.1 The Geological Strength Index

The geological strength index (GSI) was introduced by Hoek (1994), and describes the character of the rock mass. The latest major revision of the index was made by Hoek et al. (2002). The GSI is determined from charts based on the lithology, structure, and discontinuity surface conditions of the rock mass. Two main factors are considered, namely the structure/blockiness of the rock mass, and the condition of the joints. The GSI is a value between zero (laminated/sheared structure and very poor surface conditions) and 100 (intact or massive structure and very good surface conditions). Different charts have been developed for blocky rock masses (Hoek and Marinos, 2000), heterogeneous and tectonically deformed rocks (Marinos and Hoek, 2001), molassic rocks (Hoek et al., 2005), and ophiolites (Marinos et al., 2005).

2.5.2 The Q-System

The Q-system was developed at the Norwegian Geotechnical Institute (NGI) in the early 1970's (Barton et al., 1974). Since its introduction there have been two major revisions, the latest in 2002 (Grimstad et al., 2002). The Q-system is developed for use in underground openings, for rock support design and for documentation of rock mass quality.

The Q-value can be used to obtain recommendations regarding the appropriate type and quantity of rock support. The recommendations, provided by a schematic support chart, are based on the support that has been applied in previous projects in rock masses of various qualities. The majority of the experience has been obtained from projects in hard, jointed rock, including weakness zones. One should, therefore, be careful if the Q-system is applied to soft rock.

Determination of the Q-value is based on inspection of the rock mass to determine six parameters. These are:

- RQD = Rock Quality Designation (degree of jointing)
- J_n = Joint set number
- J_r = Joint roughness number
- J_a = Joint alternation number
- J_w = Joint water reduction factor
- SRF = Stress Reduction Factor

Guidelines for determining these six parameters are found in the handbook published by NGI (2017).

The Q-value is calculated using the following equation:

$$Q = \frac{RQD}{J_n} \times \frac{J_r}{J_a} \times \frac{J_w}{SRF} \tag{2.29}$$

The result will be a value between 0.001 and 1000. A high Q-value indicates good rock mass quality, while a low value indicates poor quality.

2.6 Numerical Modelling Methods

Various computer-based numerical methods giving approximate solutions to engineering problems have been developed over the past decades. Two such methods will be used in this study, namely the finite element method and the distinct element method.

2.6.1 The Finite Element Method

The finite element method (FE method) is a numerical method that can be used to solve a wide range of engineering problems. Applications include static structural analysis, dynamic problems, heat flux, fluid flow, and coupled problems. In the case of static structural analysis, forces are applied on, for example, a rock body, and the response in terms of stresses and deformations is calculated. In fluid flow problems hydraulic potentials and flow rates are calculated.

The basic principle behind the finite element method is the division of the rock volume into finite elements. The deformations of the finite elements, which can be triangular, square or otherwise, are described by the deformations in a set of nodal points. To describe the behaviour of the entire rock volume, the behaviours of all elements are integrated. The rock mass is treated as a continuum, but discontinuities can, to some degree, be represented explicitly by so-called interface elements.

The solution technique can be either implicit or explicit. An implicit solution algorithm involves a loop of load steps where the load is incrementally increased. The unbalanced forces introduced by each load increment are redistributed by solving the system of linear equations describing the integrated behaviour of all elements. Another nested loop provides convergence for each load step. Alternatively, time steps can be used in an explicit solution scheme. Unbalanced forces acting on an integration point will then lead to an acceleration. Newton's law of motion is used to calculate incremental displacements, which produce new forces according to the constitutive relation of the material. This process of updating displacements and forces continues until a convergence criterion is satisfied. Solution of flow problems is similar, with flow rates replacing stresses and hydraulic gradients replacing strains. The finite element simulations presented in this thesis are performed with the software *RS2* (Rocscience Inc., 2019), using an implicit solution algorithm.

2.6.2 The Distinct Element Method

The distinct element method is a type of discrete element method (DE method). The distinguishing characteristic of discrete element programs is their ability to model the mechanisms in a discontinuous medium. Although some finite element programs, boundary element programs and finite difference programs feature interface elements that enable them to model discontinuities to some extent, this ability is limited. Firstly, the logic may fail when many interfaces intersect. Secondly, there is often no scheme for identifying new contacts automatically. Thirdly, the logic is often restricted to small displacements and/or rotations. The discrete element method, on the other hand, is characterised by: 1) its ability to model displacements and rotations, and even complete detachment, of discrete bodies, and 2) its ability to automatically recognise new contacts during the calculation. The first ability enables the program to model important mechanisms that govern the behaviour of a discontinuous rock mass. The second ability enables it to model a large number of blocks whose interactions are initially unknown.

The distinct element programs are a subgroup of the discrete element programs. Distinct element programs use deformable contacts and an explicit time-marching solution scheme to solve the equations of motion (Cundall and Strack, 1979). The software that has been used for the distinct element simulations presented in this thesis is the three-dimensional software *3DEC* (Itasca Consulting Group Inc., 2016a). Distinct element programs are able to model the response of a discontinuous medium during loading or unloading. The medium is represented as discrete blocks, separated by discontinuities that provide the boundary conditions for each block. Large displacements along the discontinuities are allowed, and the blocks may rotate. The blocks are modelled as either rigid or deformable. In the latter case, the blocks are subdivided into a mesh of elements. The elements and their interactions are modelled using the finite difference method, which is similar to the finite element method.

2.6.3 Solid-Fluid Coupling

Different types of interaction or coupling between pore and/or joint pressure and solid stresses and deformations are available in the numerical software, including no coupling, one-way coupling and full coupling.

The uncoupled or flow-only analysis does not consider the effect of groundwater pressure on deformations, or the effect of deformations on the groundwater pressure. Rather, the groundwater pressure field is calculated independently of the solid deformations. Any mechanical calculations, if present, do not affect the hydraulic properties (hydraulic conductivities and/or hydraulic apertures), and deformations are calculated on a total stress basis.

Sequential execution of flow-only and mechanical calculations on an effective stress basis allows an interaction called one-way coupling. With one-way coupling, the groundwater pressure affects the deformations, but deformations do not affect the groundwater pressure. One-way coupling is achieved by performing a mechanical calculation after completion of a flow-only calculation. The groundwater pressures obtained from the flow-only calculation will then affect the mechanical behaviour as the effective stresses are dependent upon the groundwater pressures. However, the solid deformations are not allowed to affect the hydraulic properties or the groundwater pressures. The hydraulic conductivities and/or hydraulic apertures remain constant.

Another type of simplified coupling is used in a so-called undrained analysis. In such an analysis, deformations are assumed to be induced by mechanical loading on time-scales

so short that diffusion of groundwater pressures is negligible. There is no dissipation or drainage, which means that the change in groundwater pressure is directly and uniquely given by the change in total mean stress. No flow calculations are performed during an undrained analysis, but the groundwater pressure field will change as the solid material deforms.

Finally, there is the fully coupled hydromechanical analysis. In this analysis, solid deformations and groundwater pressures mutually affect each other. This type of coupling can be achieved by alternating frequently between flow calculations and mechanical calculations, and allowing hydraulic properties to change in response to solid deformations.

In this study, one-way coupling has been used in the FE modelling, and full coupling has been used in the DE modelling, but with certain limitations (Sections 7.8 and 9.4).

3 Working Method in This Study

In this thesis the Gevingåsen tunnel in Trøndelag, Norway is chosen for a case study. The Gevingåsen tunnel is a railway tunnel connecting Hommelvik and Hell on the Nordland line. The tunnel is 4.4 km long and has four emergency exit tunnels. The construction works started in spring 2009 and the tunnel was put into operation in August 2011. Excavation was done by drilling and blasting. The waterproofing system with SCL and sprayed membrane is used for a length of 1.8 km. The undrained SCL is applied to the walls and crown, while the invert is drained. In other parts of the tunnel, the detached lining with PE foam sheets is used for waterproofing. The Gevingåsen tunnel is an ideal case to study because: 1) partially drained SCL has been used, 2) groundwater pressure measurements from behind this lining are available, and 3) emergency exit tunnels are available for field investigations and sampling of material for laboratory investigations. The main parts of the work presented in this thesis are as follows:

1) Study of previous investigations. The study includes the following parts:
    i) Investigations of the in situ stress field in the relevant area
    ii) Investigations of the hydraulic properties of the EDZ
    iii) Investigations of the groundwater pressure behind partially drained SCLs
2) Field and laboratory investigations, including:
    i) Field investigations of bedrock conditions, rock mass quality and jointing
    ii) Laboratory investigations to obtain intact rock properties:
        a. Point load test
        b. Uniaxial compression test
3) FE modelling in *RS2*
4) DE modelling in *3DEC*

The main purpose of each of these parts is presented below.

3.1 Study of Previous Investigations

The study of previous investigations provides input parameters for the numerical simulations, and a basis for validating the results by comparison with existing measurement data.

The stress field prior to excavation (the *virgin* stress field) is an important input to numerical simulations for rock engineering purposes. Here, stress redistribution is expected to lead to changes in the hydraulic apertures of the joints in the vicinity of the tunnel. The changes in hydraulic apertures might have an effect on the groundwater pressure field. In situ stress measurements performed by SINTEF Building and Infrastructure were used to assess the virgin stress field in the relevant area. The effect of variations in the virgin stress field was then investigated by varying the input to the numerical models.

To get an idea about the hydraulic conductivity increase expected due to construction damage, injection test results from the Äspö HRL, performed by the Swedish Nuclear Fuel and Waste Management Co (SKB) and published by Ericsson et al. (2015), were reviewed. The study was carried out in hard crystalline rock, in a D&B tunnel with requirements for blasting similar to those in public tunnels. It is one of the few studies where injection tests have been used to investigate the hydraulic conductivity of the EDZ under such conditions. The

results were used as reference for determining the increase in hydraulic conductivity within the CDZ implemented in the numerical models.

To conclude the study of previous investigations, results of groundwater pressure measurements performed by Holter (2014) and Holter et al. (2015) behind partially drained SCLs at two different test sites were reviewed. The measurements were performed in the Gevingåsen tunnel and the Karmsund tunnel. The results are used for numerical back-calculation purposes in order to find the actual hydraulic conductivity increase within the CDZ.

3.2 Field and Laboratory Investigations

In order to determine remaining input parameters for the numerical models, field and laboratory investigations were carried out. The field investigations were carried out in an emergency exit tunnel connected to the Gevingåsen tunnel, while the laboratory investigations were performed at the rock mechanical laboratory at the Norwegian University of Science and Technology (NTNU) using specimens collected from the emergency exit tunnel.

The field investigations aimed at mapping bedrock conditions, rock mass quality and jointing. The joint mapping was the primary focus as distinct element modelling, which constitutes the most important part of this thesis, allows explicit representation of joints. Parameters in the Barton-Bandis slip model were collected, including strength and stiffness properties. Later these were converted to equivalent parameters in the Coulomb slip model.

The properties of the intact rock at the site were investigated in the laboratory by point load testing and uniaxial compression testing. Additionally, the density and p-wave velocity were measured using respectively the calliper method and the ultrasonic pulse technique. The uniaxial compression tests were important for establishing stiffness and strength properties. These were used both in the FE model and in the DE model.

3.3 Finite Element Modelling

Two-dimensional finite element modelling, performed with the software *RS2*, was used as an aid in setting up and interpreting the distinct element model. The FE simulations were used for two purposes. Firstly, the hydraulic conductivities within the CDZ were back-calculated using the results reviewed in the study of previous investigations. The hydraulic conductivities providing the best agreement with the available groundwater pressure measurements were identified, and later used during implementation of the CDZ in the DE model. Secondly, the induced stress field around the tunnel was investigated. The results were used to identify areas where changes in the hydraulic aperture in the DE model were expected. For this purpose, two different scenarios for the virgin stress field were included in the simulations.

3.4 Distinct Element Modelling

Finally, three-dimensional distinct element modelling in the software *3DEC* was performed. Distinct element modelling was used because it is believed that matrix fluid flow in an equivalent continuum is an inadequate way of describing the groundwater flow (which for all practical purposes will consist solely of joint fluid flow) in the jointed hard rock in the Gevingåsen tunnel. Three-dimensional modelling was chosen despite the fact that the excavated geometry can be satisfactorily described in two dimensions, because the joint sets explicitly included in the distinct element model makes the problem three-dimensional. The joint pressure behind the partially drained SCL in the tunnel was simulated, assuming first that there is no change in hydraulic apertures due to construction damage and then using

hydraulic apertures estimated based on the back-calculation performed in *RS2*. Both stress field scenarios included in the FE simulations were also included in the DE simulations. Calculation times in the order of weeks prohibited any extensive parametric analysis.

4 Review of Previous Investigations

This chapter reviews relevant investigations previously carried out by other authors. Firstly, investigations of the stress field in the Trøndelag region are reviewed. Next, the results of investigations of the hydraulic properties of the EDZ at the Äspö HRL are presented. Finally, the results of groundwater pressure measurements performed behind partially drained SCLs in the Gevingåsen tunnel and the Karmsund tunnel are summarised.

4.1 Studies of the In-Situ Stress Field

SINTEF Building and Infrastructure has provided information regarding the in situ stresses in the Trøndelag region. The reports on which the information is based are confidential, and not publicly available. The following points summarise the information relevant to the stress field at Gevingåsen:

- At the Leirfossene hydroelectric power plant near Trondheim, hydraulic fracturing tests in sub-horizontal holes (plunge of 5°) resulted in shut-in pressures in the range 1.7–3.9 MPa, with a mean of 2.5 MPa. The direction of the boreholes was chosen such that it coincided with the assumed direction of either the major or the intermediate principal stress. The shut-in pressure should then represent the minor principal stress. The gravitational vertical stress at the location of the measurements was calculated to be 1.2 MPa, 1.3 MPa lower than the mean shut-in pressure. As the shut-in pressures were not very different from the gravitational vertical stress, SINTEF concludes that the minor principal stress is sub-vertical. Furthermore, the difference between the shut-in pressures and the theoretical vertical stress agrees with SINTEF's experience that in situ stress measurements at shallow depths often result in a vertical stress that is larger than the theoretical one. The information from the Leirfossene hydroelectric power plant is based on an excerpt of a report passed on by Chief Scientist Eivind Grøv.

- At Ladehammeren, in a former underground cold storage, hydraulic fracturing was performed in two boreholes in the 1990s. One borehole had a plunge of 60°, while the other had a plunge of 70°. The shut-in pressures were measured to be 3.2–3.3 MPa. If the orientation of the boreholes coincide with the major or intermediate principal stress, the shut-in pressure represents the minor principal stress, which in that case would be sub-horizontal. Whether or not the boreholes were oriented in the direction of either the major or the intermediate principal stress is not known. However, as the theoretical gravitational stress in the area is calculated to be 1.8–2.3 MPa in the vertical direction and, using the Poisson ratio, approximately 0.4 MPa in the horizontal direction, the results of the hydraulic fracturing indicate that there is a significant tectonic component to the stresses in the area. The above information is obtained from a report by Neby (1990).

- During works related to the excavation of the Ladehammeren purification plant in the 1990s, O.T. Blindheim AS estimated the minor principal stress to be approximately 4 MPa (compared to 2.3 MPa gravitationally) and they assumed a horizontal to vertical stress ratio of one (E. Grøv, 2019, personal communication, 12 February).

4.2 Investigations of the Hydraulic Properties of the EDZ

Ericsson et al. (2015) present results of injection tests performed at the Äspö HRL. Their study is used in this thesis because it is one of the few studies that include injection tests to investigate the hydraulic conductivity of the EDZ in hard crystalline rock. Their tests were performed in borehole sections with short lengths, thus providing high spatial resolution. The measurement equipment used in their investigations is similar to equipment that SINTEF is currently preparing for Bane NOR, whose aim is to collect data on the hydraulic conductivity in the EDZ in Norwegian tunnels. Consequently, data similar to those presented by Ericsson et al. may shortly be available from Norwegian tunnels.

The rock mass at the Äspö test site consists of fine-grained granite, diorite and granodiorite, intersected by pegmatite dykes. The rock mass has three dominant fracture sets. The rock overburden is approximately 400 m. The investigations included injection tests in short boreholes in the tunnel invert, in order to investigate the transmissivity in the EDZ. The equipment used was specifically designed for use in short boreholes in a tunnel. No grouting had been performed at the test site, which nevertheless displayed only minor leakages into the tunnel (0.54 l/min along a 20 m long tunnel section). The test sections were, in terms of depth below the tunnel invert: 0.0–0.1 m, 0.1–0.2 m, 0.2–0.4 m, 0.4–0.6 m, and 0.6–1.0 m (in some boreholes 0.6–2.0 m). In total, 210 injection tests were performed, and used to calculate section transmissivities and hydraulic conductivities. They also used interpolation by kriging to investigate the spatial transmissivity pattern at different depths. Their conclusions include:

- The depth of the EDZ in the tunnel invert extended on average 0.3 m into the rock mass in column charge areas and 0.5 m in bottom charge areas.
- Blast-induced fractures, and an increase in the aperture of natural fractures led to a higher transmissivity in the EDZ than in the undisturbed rock mass. Measurement sections 0.0–0.1 m and 0.1–0.2 m were more transmissive than sections at depths exceeding 0.4 m. The section 0.2–0.4 m seemed to constitute a transition zone. In the depth interval 0.0–0.1 m, there were areas with a transmissivity of magnitude 10^{-4} m^2/s, while at depth 0.4–0.6 m the most transmissive areas had a transmissivity of 10^{-7} m^2/s. However, the zones of low transmissivity displayed values of similar order of magnitude in the different depth intervals.
- The interconnectivity between the induced fractures was limited, with transmissive areas no longer than 7 m. The characteristic size of transmissive and less transmissive areas seemed to be 2–7 m.

Table 4.1 presents descriptive statistics for the measured hydraulic conductivities. The arithmetic, harmonic and geometric means are shown, as these represent the effective hydraulic conductivity for cells arranged in respectively a 1D parallel, a 1D series and a 2D configuration (Section 2.3.1.3). Note that the arithmetic and geometric means decrease by several orders of magnitude when moving from highly disturbed rock mass close to the tunnel periphery, into less disturbed rock mass farther away. Based on the results from the Äspö HRL, it is decided to represent the CDZ in the Gevingåsen tunnel by modifying the hydraulic properties in the region within 0.4 m from the excavation boundary.

Table 4.1: Descriptive statistics for the hydraulic conductivities measured by Ericsson et al. (2015) in the EDZ at the Äspö HRL.

Section	Sample size	Minimum	Median	Maximum	Arithmetic Mean	Harmonic mean	Geometric mean
m		m s^{-1}					
0.0–0.1	42	1.5×10^{-9}	1.1×10^{-5}	6.5×10^{-4}	1.1×10^{-4}	1.8×10^{-8}	3.3×10^{-6}
0.1–0.2	42	1.4×10^{-9}	4.6×10^{-8}	1.4×10^{-4}	1.0×10^{-5}	6.7×10^{-9}	8.1×10^{-8}
0.2–0.4	42	5.0×10^{-10}	8.2×10^{-9}	1.8×10^{-6}	2.0×10^{-7}	2.4×10^{-9}	1.2×10^{-8}
0.4–0.6	42	4.9×10^{-10}	1.1×10^{-9}	1.3×10^{-6}	6.1×10^{-8}	1.1×10^{-9}	3.1×10^{-9}
0.6–1.0	37	3.1×10^{-10}	4.8×10^{-10}	5.9×10^{-8}	3.4×10^{-9}	5.2×10^{-10}	8.0×10^{-10}
0.6–2.0	5	1.4×10^{-10}	1.0×10^{-9}	2.3×10^{-9}	1.1×10^{-9}	4.7×10^{-10}	7.9×10^{-10}

4.3 Investigations of the Pressure behind Partially Drained SCLs

4.3.1 Investigations in the Gevingåsen Tunnel

Holter et al. (2015) present measurements of the groundwater pressure behind the partially drained SCL at a test site in the Gevingåsen tunnel. The rock mass at the test site consists of poor to good quality (Q = 3–17, with a typical value of 5) dark mica schist. The overburden at the site is 40–50 m, and the groundwater table is estimated to be located 40 m above the tunnel crown. No grouting has been carried out at the test site.

The measurements were conducted using three vibrating wire piezometers. The piezometers were installed in boreholes extending 200–250 mm from the internal surface of the lining. The boreholes were sealed in the outer end with resin and mortar. One piezometer was installed at the centre of the tunnel crown, while the two remaining were installed on either side, 2 m down (Fig. 4.1). The monitoring revealed very stable pressures throughout the entire monitoring period of nine months. The groundwater pressure was significantly lower than the hydrostatic pressure of approximately 400 kPa (Table 4.2). The pressure was highest at the centre of the crown. The pressures measured by the two other piezometers were lower, and quite similar to each other.

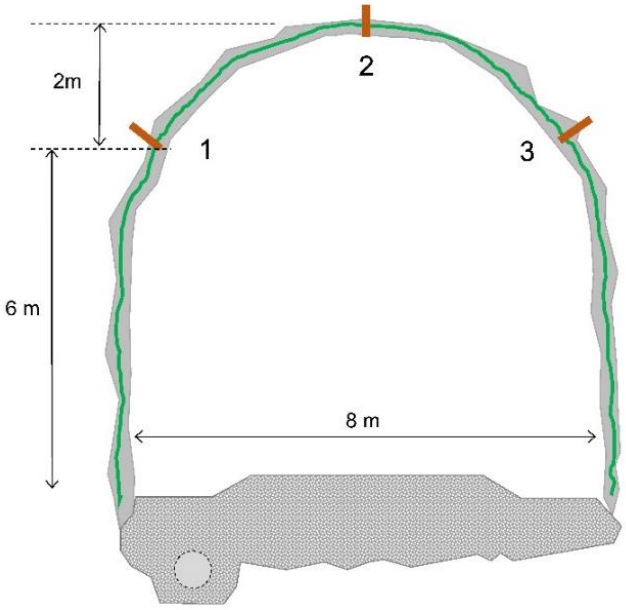

Figure 4.1: Tunnel cross-section showing the location of the piezometers used by Holter et al. (2015) to measure groundwater pressures behind the SCL in the Gevingåsen tunnel. Reprinted from Holter et al. (2015) with permission.

Table 4.2: Groundwater pressures measured by Holter et al. (2015) behind the SCL in the Gevingåsen tunnel. The pressures are significantly lower than the hydrostatic pressure. The groundwater table is assumed to be 40 m above the crown of the tunnel.

Piezometer	Groundwater pressure	Fraction of the hydrostatic pressure
	kPa	
1	60	0.15
2	135	0.34
3	50	0.13

4.3.2 Investigations in the Karmsund Tunnel

Measurements of the groundwater pressure behind a partially drained SCL have also been conducted in a ventilation cavern in the Karmsund tunnel near Haugesund, Norway, by Holter (2014). Similar to the Gevingåsen tunnel, this test site is also a D&B tunnel in jointed hard rock. The rock mass consists of fair to very good quality (Q = 6–66, with a typical value of 23) massive mylonitic gneiss. The rock cover is approximately 130 m, and the in situ static head is estimated to be 80–90 m at the level of the tunnel invert. The test site is located approximately 50 m from the main highway tunnel. Pressures were measured in three boreholes in the tunnel wall, each with a length of 9 m.

The measurements revealed that the pressure is almost hydrostatic at the innermost points in the boreholes, while it is significantly lower close to the tunnel contour (Fig. 4.2). However, there are large differences between the three boreholes. In the borehole sections closest to the contour, the pressure varied from 36 kPa to 505 kPa. In distant sections, the pressures generally decreased slightly with time.

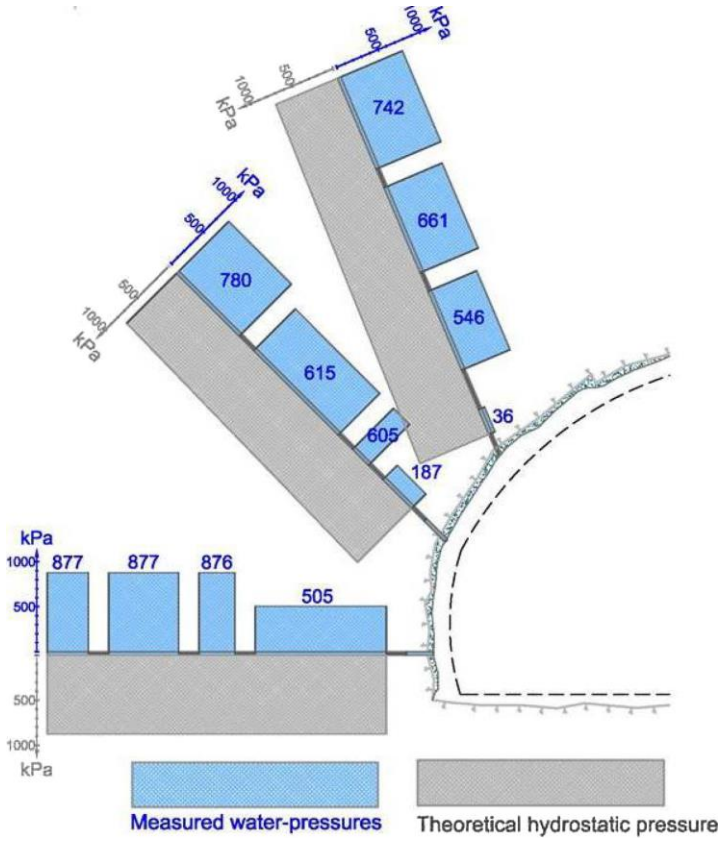

Figure 4.2: Groundwater pressures measured by Holter et al. (2015) in boreholes in the Karmsund tunnel. Reprinted from Holter (2014) with permission.

5 Field and Laboratory Investigations

To obtain necessary input data for the numerical modelling, field and laboratory investigations have been executed. Section 5.1 presents the field investigations, while Section 5.2 presents the laboratory investigations.

5.1 Field Investigations

This thesis focuses on the conditions in emergency exit tunnel R1 (hereafter referred to simply as the R1), which runs parallel to the Gevingåsen railway tunnel for approximately 520 m. The R1 branches off from the main tunnel approximately 915 linear metres from the Hommelvik portal to the southwest, and ends where it merges with the emergency exit tunnel R2. The overburden in the investigated area is in the range 55–75 m. The emergency exit tunnels are, as the main tunnel, largely covered with sprayed concrete. There are, however, a few niches in the north-western wall of the R1 where sprayed concrete has not been applied. Field investigations were mainly performed in three such niches, located 120, 255 and 430 linear metres from the point where the R1 branches off from the main tunnel. Field investigations were carried out on 1 February 2019. Joint orientations, characteristics and conditions (including JRC and JCS) and rock mass quality (including GSI and Q-value) were investigated. The investigations were carried out using pen and notebook, a geological compass, a profile gauge, an L-type Schmidt hammer, and a digital camera. Large scale folds, faults and weakness zones were not considered, as such structural features are outside the scope of this thesis.

5.1.1 Bedrock

The bedrock in the area is part of the Støren Nappe in the upper Caledonian allochthon. The rocks belong to the Lower Hovin and Ekne groups, and consist mainly of conglomerates, sandstones, slates, and phyllites. The rocks were deposited in the Ordovician, and were later subject to Caledonian regional metamorphism. The rock units in immediate proximity to the tunnel, according to the Geological Survey of Norway (NGU), are (Fig. 5.1):

- Metagreywacke (Lower Hovin Group): greenish grey with thin layers of shale
- Rhyolitic tuff (Lower Hovin Group)
- Metasandstone, slate and phyllite (Ekne Group): The metasandstone is greenish grey and thinly banded, while the slate and phyllite are dark grey and thinly laminated. The three rock types occur in alternation.
- Rhyolitic tuffite (Ekne Group)
- Conglomerate and greywacke (Ekne Group)

The rock in the R1 was, during the field investigations, found to be a strong to very strong, pale greenish grey and fine-grained rock, possibly a metasandstone with interbedded layers of phyllite. The rock is assessed to be low-grade metamorphosed and mostly unaltered. It is folded on centimetre to metre scale, and has a sub-horizontal layering or foliation. Figure 5.2 shows the rock mass in the niche at chainage 430 of the R1. In some places the rock mass is heterogeneous, with bands and lenses of nearly pure quartz, and folds at both the micro and macro scales. Figure 5.3 shows the rock mass in the niche at chainage 255, where the quartz bands and lenses are prominent.

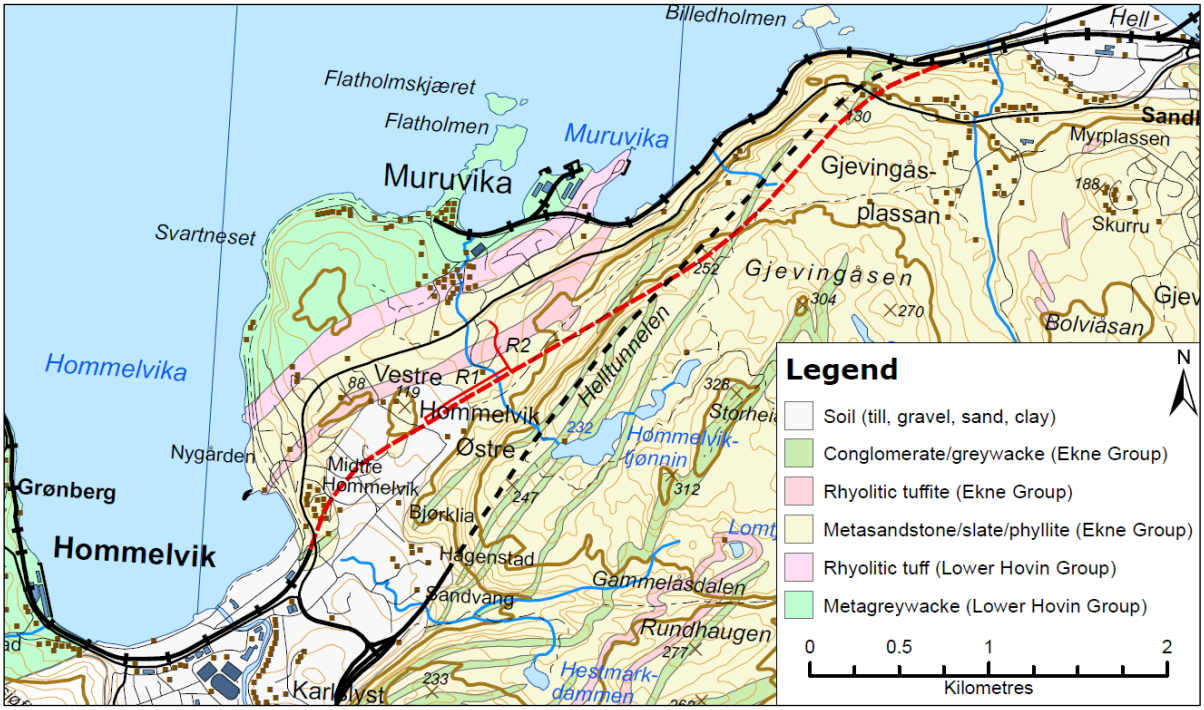

Figure 5.1: Bedrock map of the area around the Gevingåsen tunnel. The tunnel is shown with a dashed red line, while the two emergency exit tunnels are shown with solid red lines. The rock units have the colours used by the NGU. The map contains data under the Norwegian Licence for Open Government Data (NLOD) made available by the NGU, and data under the CC BY 4.0 license made available by the Norwegian Mapping Authority.

Figure 5.2: Photo of the rock mass in the niche at chainage 430 of the R1. The rock is a greenish grey, fine-grained metasandstone. Glove for scale.

Figure 5.3: Photo of the rock mass in the niche at chainage 255 of the R1. The rock is more fine-grained and heterogeneous than at chainage 430, with more frequent quartz bands and folds. Pen for scale.

5.1.2 Rock Mass Quality

The rock mass quality has been mapped according to the Q and GSI systems. The GSI is used directly later, in the calculation of stiffness parameters.

5.1.2.1 Q-value

In terms of Q-value, the rock mass varies from poor to good quality. Table 5.1 shows the values for the different Q parameters, evaluated during the field investigations. The typical Q-value lies in the range defined as fair. Two controlling factors are the joint set number and the joint roughness number. Whereas most of the other parameters are quite favourable, the joint set number of 9–12 and the typical joint roughness number of 1–1.5 are relatively unfavourable, leading to a lower Q-value.

The Q-values found during the field investigations are in good agreement with the values found by Holter et al. (2015), in relation to the monitoring of the groundwater pressure behind the SCL (Section 4.3.1). The typical value is found to be slightly higher in this study, while the worst and best values are evaluated to be slightly lower.

5.1.2.2 GSI

The rock mass is generally blocky, and the condition of the discontinuity surfaces is generally good. In areas where the rock mass is more heterogeneous with veins and small-scale folds, the GSI is in the range 50–60, while in relatively homogeneous areas, the GSI is in the range 65–75. The typical value is approximately 70.

Table 5.1: Q-parameters for the metasandstone in R1, determined during field investigations. The worst, best, and typical values are shown.

Parameter	Worst	Best	Typical	Comment
RQD	65	80	75	
J_n	12	9	9	Worst: three joint sets plus random joints Best: three joint sets
J_r	1	1.5	1.5	Worst: smooth, planar Best: rough, irregular, planar
J_a	2	1	1.2	Worst: slightly altered joint walls with sandy particles Best: unaltered joint walls, surface staining only
J_w	0.66	1	0.85	Worst: medium inflow (many drips/"rain") Best: Dry excavation or minor inflow (a few drips)
SRF	1.5	1	1	Worst: low to medium stress Best: medium stress, favourable stress conditions
Q	1.2	13	9	Poor to good rock mass quality. Typically fair.

5.1.3 Joint Mapping

Mapping of the joints, indicates that there are three joint sets plus additional random joints. The most dominant set is sub-horizontal and parallel with the foliation. The typical spacing of the joints in this set is 0.5–1 m, while the persistence is typically approximately 2 m or more. Another set is sub-vertical and strikes approximately north-south. This set has a typical spacing of 0.2–1.5 m, and a persistence of 0.5–2 m. The last, and least dominant set is steeply dipping and strikes approximately east-west. The joints in this set are more closely spaced with a spacing of 5–50 cm. However, the persistence is less than for the other sets; typically less than one metre. The joints are unaltered or with a sparse filling of sand grains. The surfaces are generally rough and planar with immediate rock-wall contact. Some joints, however, are smooth on the small scale and some are stepped or undulating on the intermediate scale.

5.1.3.1 Joint orientations

The orientation of a total of 33 joints were measured. All measurements are shown in Appendix A. Joint orientations are reported as dip/dip direction. The dip direction is measured in degrees east of north. The pole vectors of the joints are presented and contoured in a lower hemisphere equal area stereoplot in Fig. 5.4. The joints are interpreted to belong to three joint sets: a sub-horizontal set, a north-south striking sub-vertical set, and an east-west striking steeply dipping set. In addition there are random joints that do not belong to any set.

The sub-horizontal set have a higher variability than the other two, possibly with a dependency upon the spatial location along the tunnel. There is one cluster dominated by measurements from chainage 120 with dip and dip direction of approximately 30°/270°. Another cluster, consisting entirely of measurements from chainage 255 have dip and dip direction of 08°/054°. Finally, the measurements from chainage 430 indicate that the sub-horizontal joint set have dip and dip direction of approximately 30°/154° at this location. The overall mean orientation of the set is 06°/211°. This is the orientation that will be used in the numerical DE model. It is expected that the simulation results, at least when it comes to joint pressures, are not very sensitive to the exact orientation of the joint sets. However, the number of joint sets, and also their general orientations relative to the tunnel are expected to be important.

The two other joint sets have a more constant orientation, with the three spatial locations represented seemingly at random within both sets. Table 5.2 shows the mean dip and dip directions of the three joint sets, as well as the standard deviation, and the typical spacing and persistence.

5.1.3.2 Joint roughness coefficient (JRC)

The roughness of the joints was investigated using a profile gauge to determine the JRC_0 of selected joints visible on the excavation surface. The profiles were all aligned with the cross-sectional plane of the tunnel, in order to represent the roughness in (approximately) the direction of potential displacement. Two representative profiles were obtained for each of the three joint sets. The profiles drawn in the field are shown in Appendix B. The roughness of the three joint sets does not vary very much. For the numerical modelling purposes of this study it is judged sufficient to use the same value for the JRC_0 for all joint sets. The representative JRC_0 is estimated to be eight. For joints with rough small scale features, this JRC_0 suggests that the intermediate scale features are somewhere between planar and undulating/stepped (Barton, 1988). This corresponds to a value of J_r somewhat higher than the value found during assessment of the Q-parameters.

Table 5.2: Interpreted joint sets with their mean dip and dip directions. Typical spacing and persistence as observed in the field are shown in the two final columns.

Set	Dip	Dip direction	Standard deviation	Spacing	Persistence
				m	m
J1	06°	211°	31°	0.5–1	>2
J2	80°	076°	18°	0.2–1.5	0.5–2
J3	67°	349°	20°	0.05–0.5	<1

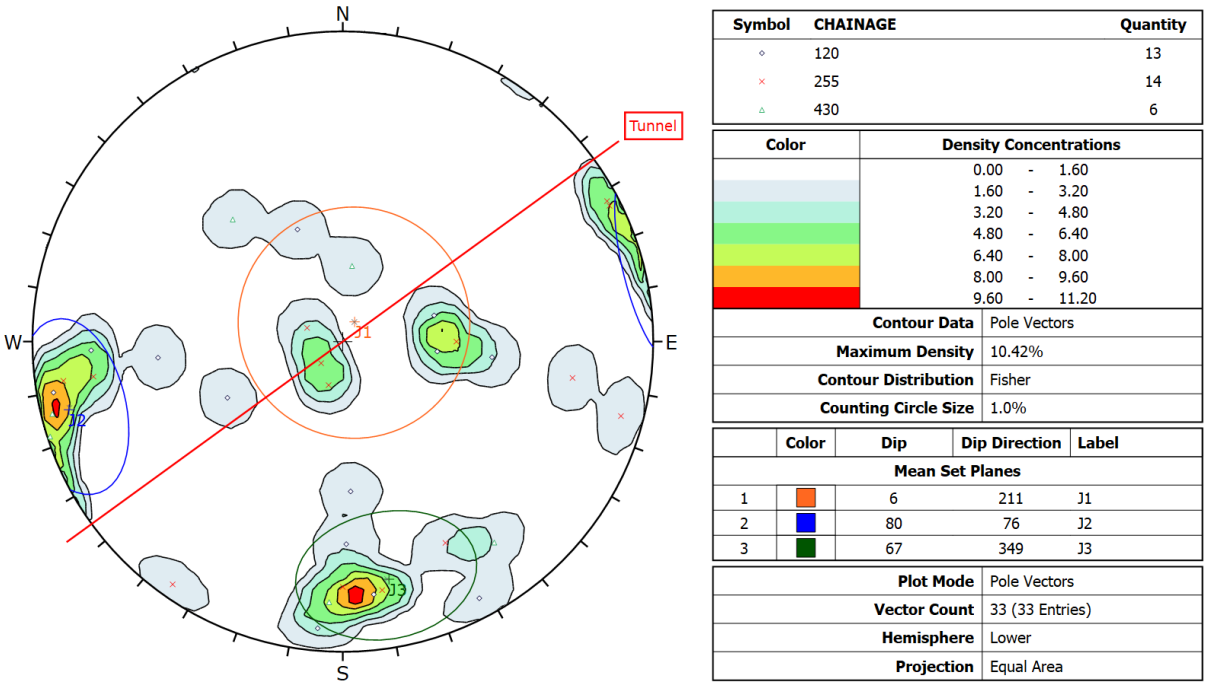

Figure 5.4: Equal area stereoplot with poles and contours of the mapped joints, and three interpreted joint sets. There is a sub-horizontal set (J1), a north-south striking sub-vertical set (J2), and a east-west striking steeply dipping set (J3). The joint sets are shown with their one standard deviation variability cones.

5.1.3.3 Joint wall compressive strength (JCS)

The compressive strength of the joint walls was measured using a Proseq Original Schmidt L Hammer. The rebound value was measured directly on joints of suitable dimensions (tens of centimetres) visible on the excavation surface. Measurements were performed on one joint from each joint set, with a direction of impact that was perpendicular to the joint plane. The orientation of the hammer axis was +46° for the joint belonging to set J1, -4° for the joint belonging to set J2, and -19° for the joint belong to set J3 (downward is +90° and upward is -90°). Clamping and steel base support were not used. Figures 5.5, 5.6, and 5.7 show the joints before and after testing (a detail view of an impact point is shown in Fig. 5.6b).

One sample was collected for each joint set. The sample size was 20 as recommended in the method suggested by the International Society for Rock Mechanics (ISRM) (Aydin, 2009). The values have been normalised according to the method described by Basu and Aydin (2004). Table 5.3 shows the mean, median, mode, and range statistics of the normalised rebound values for the three joint sets. In accordance with the current ISRM suggested method, no reading is discarded. Figure 5.8 present the same data in the form of histograms.

The Schmidt hammer rebound values are used to estimate the JCS_0 in the Barton-Bandis criterion. As suggested by Barton (1978), the correlation proposed by Deere and Miller (1966) is used for this purpose:

$$\log_{10} \sigma_{ci} = 0.00088\gamma R + 1.01 \tag{5.1}$$

where σ_{ci} is the uniaxial compressive strength (UCS) of intact rock, γ is the weight density of the rock and R is the rebound value in the vertically downward direction. Using this equation, combined with the corrections provided by Barton (1978) for hammer directions other than vertically downward, the following JCS_0-values are obtained:

- Joint set J1: JCS_0 = 123 MPa
- Joint set J2: JCS_0 = 56 MPa
- Joint set J3: JCS_0 = 66 MPa

Table 5.3: Descriptive statistics for the normalised Schmidt L hammer rebound values for the three joint sets in the R1.

Set	Mean	Median	Mode	Minimum	Maximum	Range
J1	49	50	56	32	64	32
J2	35	37	37	22	46	24
J3	38	40	43	26	53	27

a) Before testing. Folding rule for scale.

b) After testing. Impact points are seen as white marks.

Figure 5.5: Joint surface (set J1) before (a) and after (b) testing of the Schmidt hammer rebound value.

a) Before testing. Folding rule for scale.

b) After testing (detail view). The impact point is seen as a white mark.

Figure 5.6: Joint surface (set J2) before (a) and after (b) testing of the Schmidt hammer rebound value.

a) Before testing

b) After testing. Impact points are seen as white marks.

Figure 5.7: Joint surface (set J3) before (a) and after (b) testing of the Schmidt hammer rebound value.

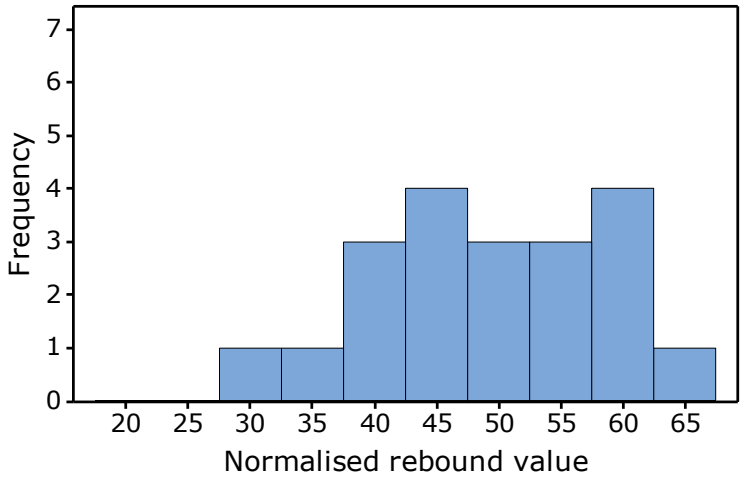

a) Joint set J1

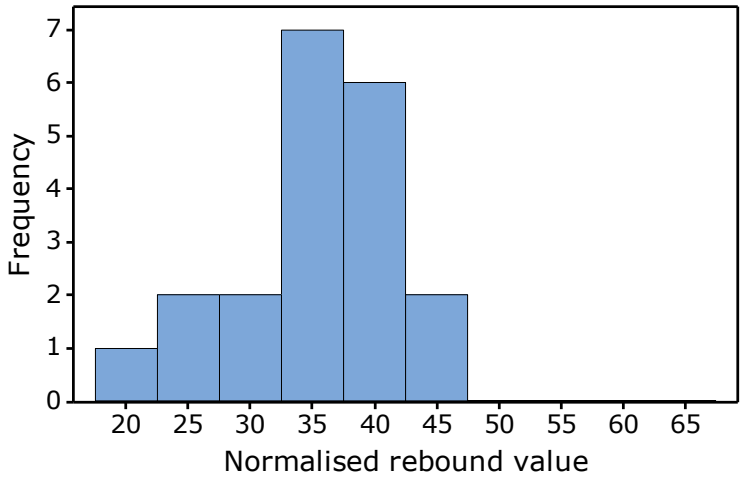

b) Joint set J2

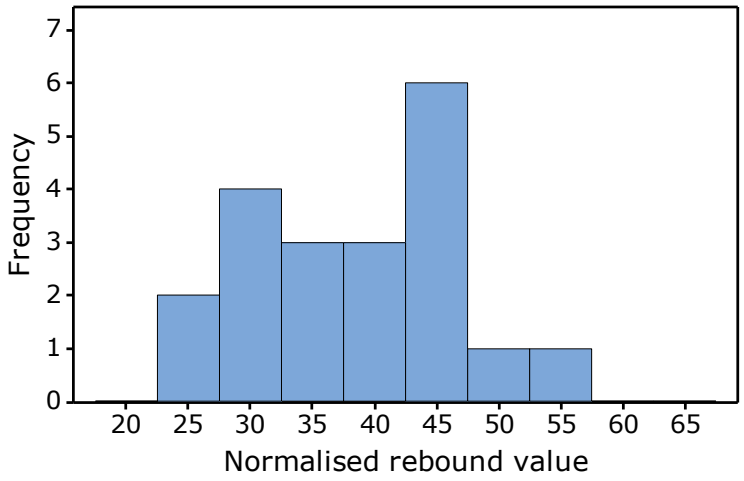

c) Joint set J3

Figure 5.8: Histograms of normalised rebound values for the three joint sets. The figure shows: a) joint set J1, b) joint set J2, and c) joint set J3.

5.2 Laboratory Investigations

Complementary to the field investigations, laboratory investigations were performed to obtain rock mechanical properties. The investigations were performed at the rock mechanical laboratory at the NTNU, and include point load tests and uniaxial compression tests.

5.2.1 General

Specimens for the laboratory investigations were collected in the R1 on 11 February 2019. The sample consisted of blocks collected directly from unlined parts of the tunnel walls, as well as blocks collected from the loose material lying along the walls of the tunnel. Although most of the loose material must be assumed to be aggregate delivered to the tunnel from another location, it is reasonable to assume that this is not the case for the collected blocks as these were significantly larger than the rest of the loose material and larger than any grain size that would be part of an aggregate. The site engineer during the excavation of the Gevingåsen tunnel confirms that this is indeed a reasonable assumption (T. Rise, 2019, personal communication, 12 February). The assumption is also verified by the fact that the blocks are of similar rock type as the tunnel walls. However, a reservation is made for the chance that the blocks collected from the loose material may not represent the conditions at the exact location they were collected. The blocks might originate from other parts of the tunnel. Anyhow, as the rock type is similar, this is probably of little importance. Twelve blocks were collected in total, but only four of these were used for testing (Fig. 5.9). Hereafter, these blocks are numbered 1 to 4. Block 1 was collected directly from the wall of the tunnel at chainage 345 of the R1, while the remaining three blocks were collected from the loose material between the point where the R1 branches off from the main tunnel (chainage 0) and chainage 345. The water content at the time of testing is, due to the short time of storage, assumed to be close to, but a little lower than, the in situ water content.

Figure 5.9: Blocks collected from the R1 for use in laboratory investigations. The four blocks that were used are the ones from which core specimens have been drilled. From left to right: block 2 (three cores), block 4 (four cores), block 1 (eight cores) and block 3 (two cores).

5.2.1.1 Lithology

The bedrock in the area where the blocks were collected was assessed to consist of metasandstone and phyllite in alternation. The general impression from the field investigations is that the metasandstone is the most dominating in the R1. The lithology of the four blocks tested in the laboratory is as follows:

- Block 1: pale grey, fine-grained rock with scattered lenses and bands (millimetres to approximately 1 cm thick) of nearly pure quartz. The quartz bands appear at a moderate angle (~30°) to the main foliation. The rock is assessed to be a fine-grained metasandstone.
- Block 2: greenish grey rock with alternating light and dark bands (with thickness of millimetres or less) parallel to the main foliation. The light bands are dominated by quartz. The banded structure is cut by another set of quartz rich bands (1–2 mm thick) with millimetre-scale folding. These bands make a small to moderate angle (<30°) with the dominating banded structure. The rock contains numerous pyrite crystals of millimetre size, and the foliation planes have a glossy sheen and an almost greasy feel. The greenish shade of colour might be caused by chlorite. The rock is assessed to be a phyllite.
- Block 3: Similar to block 1 in appearance, but with a darker, greenish colour, a more fine-grained texture, and a higher content of mica. The rock is schistose with glossy layering surfaces. Contains abundant quartz bands and lenses (0.2–1 cm thick) in a disorderly/chaotic pattern. Block 3 is classified as a fine-grained metasandstone bordering on a phyllite.
- Block 4: similar to block 1 with additional thin layers of clay (<1 mm to ~1 cm thick), parallel to the dominating foliation. Also, block 4 appears marginally more fine-grained than block 1. Similar to blocks 1 and 3, block 4 is classified as a metasandstone.

The four blocks are metamorphosed to different degrees, with increasing degree of metamorphism in the order 1, 4, 3, 2. The protoliths were probably arenaceous to argillaceous sedimentary rocks. Specimens retrieved from all four blocks are included in the point load tests, while only blocks 1 and 4 are represented in the uniaxial compression tests.

5.2.1.2 Description of tests

The point load test is an index test used for classification of the strength of intact rock, including potential strength anisotropy. The measured parameters are the point load strength index $I_{s(50)}$ and the strength anisotropy index $I_{a(50)}$. The latter is the ratio between the point load strengths in the strongest and weakest directions, respectively. The test might also be used to estimate other strength parameters such as the uniaxial compressive strength and the tensile strength. The test can be performed on core specimens, blocks or irregular lumps, and may be performed using portable equipment. This makes it a highly versatile test that can be performed in the field as well as in the laboratory. The principle of the test is that a concentrated load is applied to the specimen through a pair of spherically truncated, conical steel platens. The load is increased until failure occurs. The load at failure and the specimen dimensions are registered and used to calculate the point load strength index. Repeating the test in a direction perpendicular to the first one, enables calculation of the anisotropy index.

The uniaxial compression test measures the uniaxial compressive strength of a rock specimen with regular geometry. If suitable deformation measuring devices are used, the test may also yield the stress-strain curve, the Young's modulus, and the Poisson ratio of the specimen. The test is used for classification and characterization of intact rock, and is

performed by applying a uniform load at opposite end faces of the specimen. The load is increased until the specimen fails. The load at failure is measured and the deformation history is monitored.

5.2.2 Method

The tests were conducted according to the methods proposed by the ISRM. The suggested methods include:

- Franklin (1985): "Suggested Method for Determining Point Load Strength"
- Bieniawski and Bernede (1979): "Suggested Methods for Determining the Uniaxial Compressive Strength and Deformability of Rock Materials"

In addition to the point load test and the uniaxial compression test, the density and the P-wave velocity of the specimens used for the uniaxial compression tests were determined. The densities were determined with the calliper method, while the P-wave velocities were determined with the ultrasonic pulse technique. The ISRM suggested methods describing these techniques are:

- Franklin et al. (2007): "Suggested Methods for Determining Water Content, Porosity, Density, Absorption and Related Properties and Swelling and Slake-Durability Index Properties. Part 1: Suggested Methods for Determining Water Content, Porosity, Density, Absorption and Related Properties"
- Aydin (2014): "Upgraded ISRM Suggested Method for Determining Sound Velocity by Ultrasonic Pulse Transmission Technique"

Deviations from the suggested methods will be explicitly stated.

5.2.2.1 Specimen preparation

The blocks were retrieved from the field on 11 February 2019. They were stored indoors in the laboratory for one day before core specimens were drilled from four blocks with suitable size and shape. Drilling was performed with a radial coring machine with an Ø 44 mm drill bit on 12 February. The diameter was chosen such that it was possible to obtain sufficiently many cores of acceptable length for the uniaxial compression test. Representative specimens from the four blocks are shown in Fig. 5.10. The cores were oriented such that their axes were perpendicular to the main foliation.

After drilling, the cores for the uniaxial compression tests were sawn and grinded. Sawing was performed immediately after coring (i.e., 12 February) using a diamond specimen lab saw. The next day, the cores were grinded with a specimen grinder, to obtain loading faces that were flat and parallel in agreement with the ISRM specifications. During grinding a piece chipped of the end of a specimen from block 4. Therefore, this specimen had to be sawn and grinded again, resulting in a specimen that was shorter than 2.5 times the diameter, which is the lower limit for this ratio suggested by the ISRM. Due to the sparsity of test material, this core was still included in the uniaxial compression tests.

5.2.2.2 Point load test

Point load testing was performed on 13 February 2019. Diametral tests were performed first, producing specimens that were subsequently used for axial testing. The tests were performed using a portable GCTS PLT-100 Point Load Test System (Fig. 5.11), with an axial load capacity of 100 kN. Dimensions were measured using a digital calliper.

a) Specimen from block 1: pale grey, fine-grained metasandstone with quartz bands

b) Specimen from block 2: phyllite with pyrite crystals and folded quartz bands

c) Specimen from block 3: metasandstone with quartz bands in a chaotic pattern

d) Specimen from block 4: similar to block 1, with additional dark bands

Figure 5.10: Representative core specimens used in the laboratory investigations. The specimens originate from: a) block 1, b) block 2, c) block 3, and d) block 4. The core axes are perpendicular to the main layering or foliation.

Figure 5.11: The GCTS PLT-100 Point Load Test System, used for point load testing in the laboratory.

5.2.2.3 Uniaxial compression test

For the uniaxial compression test, only cores from blocks 1 and 4 were used, as these were the only blocks from which it was possible to obtain cores with a satisfying ratio between the length and the diameter. Five cores from block 1 and four cores from block 4 were used. Hereafter, these are numbered 1.1–1.5 and 4.1–4.4, where the first digit is the block number, and the second digit is used to distinguish between specimens from the same block.

The final preparations for the uniaxial compression tests included measurements of specimen dimensions, density and P-wave velocity. The dimensions of the cores (Table 5.4) were measured using a digital calliper. The diameter was measured in two perpendicular directions at the top, middle and bottom of each specimen (i.e., six measurements in total), while one measurement was made of the length of each specimen. The specimens were weighed using a Mettler Toledo PB4002-S laboratory balance. The P-wave velocity in the axial direction was determined by the ultrasonic pulse technique with a Proseq Pundit Lab instrument with a frequency of 54 kHz. Contact gel was used to improve the contact between the sensors and the specimen surfaces.

The uniaxial compression tests were carried out on 14 February using a GCTS RTR-4000 Rapid Triaxial Rock Testing System (Fig. 5.12), with servo control and an axial load capacity of 4000 kN. The radial strain rate was controlled manually such that the load rate remained approximately 0.8 MPa/s throughout all tests. Strains were measured with a GCTS DEF-5100-A Rock Deformation Device with three sensors: two axial sensors for measuring axial strains and one circumferential sensor for measuring radial strains. During the tests, each specimen was covered with a plastic sleeve to prevent uncontrolled disintegration.

Table 5.4: Dimensions and weight of the specimens prepared for the uniaxial compression tests. The length to diameter ratio of specimen 4.4 is highlighted by red font colour as the ratio is below the lower limit suggested by the ISRM.

Specimen	Diameter	Length	Length/diameter	Weight
	mm	mm		g
1.1	43.82	112.11	2.558	458.61
1.2	43.81	112.10	2.559	458.42
1.3	43.82	112.09	2.558	458.33
1.4	43.80	112.09	2.559	458.21
1.5	43.80	112.82	2.576	460.91
4.1	43.79	111.79	2.553	463.80
4.2	43.81	111.79	2.552	464.59
4.3	43.79	111.81	2.553	463.43
4.4	43.80	101.65	2.321	421.59

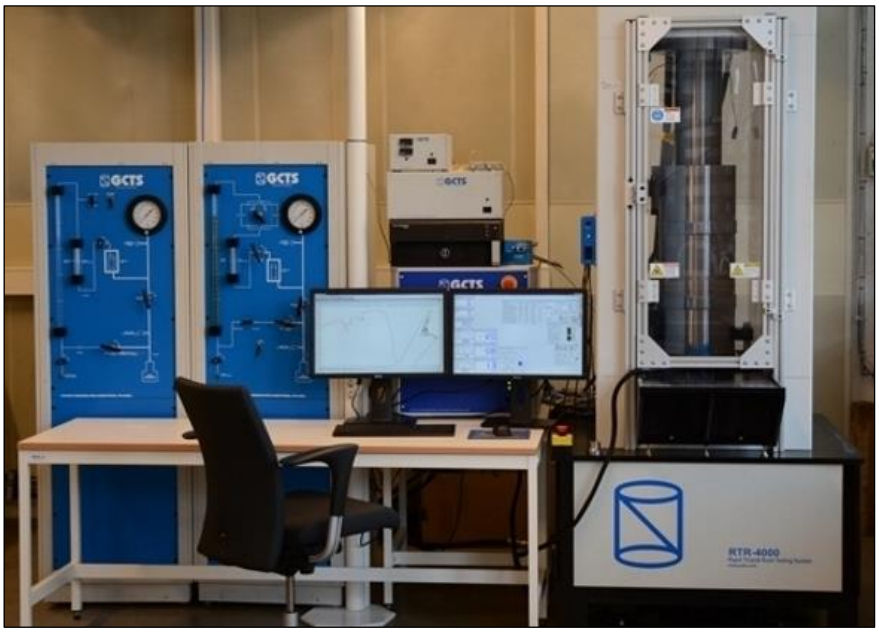

Figure 5.12: The GCTS RTR-4000 Rapid Triaxial Rock Testing System, used for uniaxial compression testing in the laboratory. Reprinted from *Bergmekanisk laboratorium*, by Department of Geoscience and Petroleum, NTNU, n.d., retrieved 12 March 2019, from https://www.ntnu.no/igp/lab/bergmekanisk. Reprinted with permission.

5.2.3 Results

5.2.3.1 Point load test

The results of the point load tests are shown in Table 5.5, in the form of a summary tabulation for subsamples tested perpendicular and parallel to the main foliation. The mean size-corrected point load indices and the anisotropy index for each block are shown. The values obtained when combining the results from blocks 1 and 4 are also shown due to the similarity between these blocks, both in physical appearance and in test results. The means are calculated as suggested by the ISRM suggested methods. Figures 5.13 and 5.14 show individual value plots of the size-corrected point load indices. The complete results are presented in Appendix C.

The axial tests proved difficult in the sense that numerous tests on specimens from blocks 1 and 3 resulted in invalid modes of failure. The resulting failure surface was often oblique, going through only one of the loading points.

Table 5.5: Summary tabulation of mean $I_{s(50)}$ values for subsamples tested perpendicular (⊥) and parallel (‖) to the main foliation, and the corresponding $I_{a(50)}$ values. The results are organised per block, and additionally the combined results for blocks 1 and 4 are shown.

Block(s)	Mean $I_{s(50)\perp}$	Mean $I_{s(50)\parallel}$	$I_{a(50)}$
1	8.4	3.2	2.7
2	5.7	1.9	3.0
3	5.8	1.8	3.2
4	7.5	3.1	2.4
1 and 4	8.0	3.1	2.5

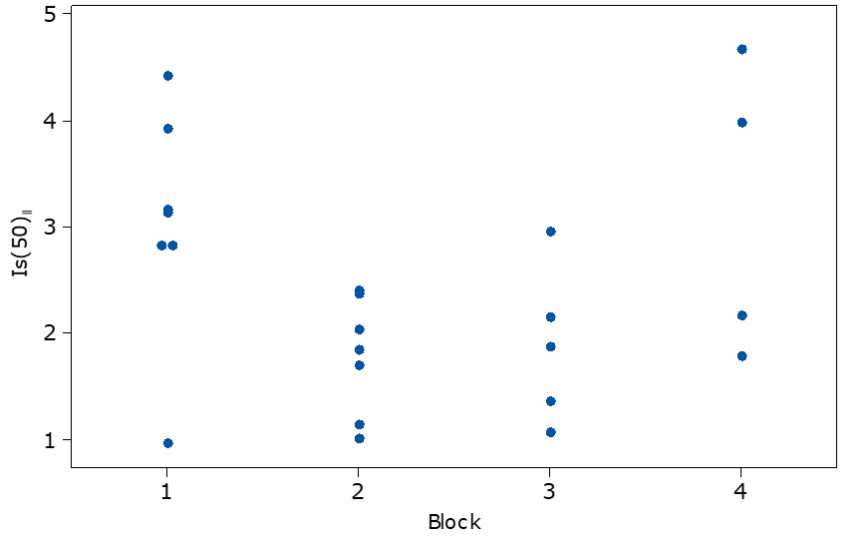

Figure 5.13: Individual value plot of the results from the diametral point load tests. The results of invalid tests are not shown. The size-corrected point load index $I_{s(50)\parallel}$ for specimens tested parallel to the main foliation is plotted versus the block number.

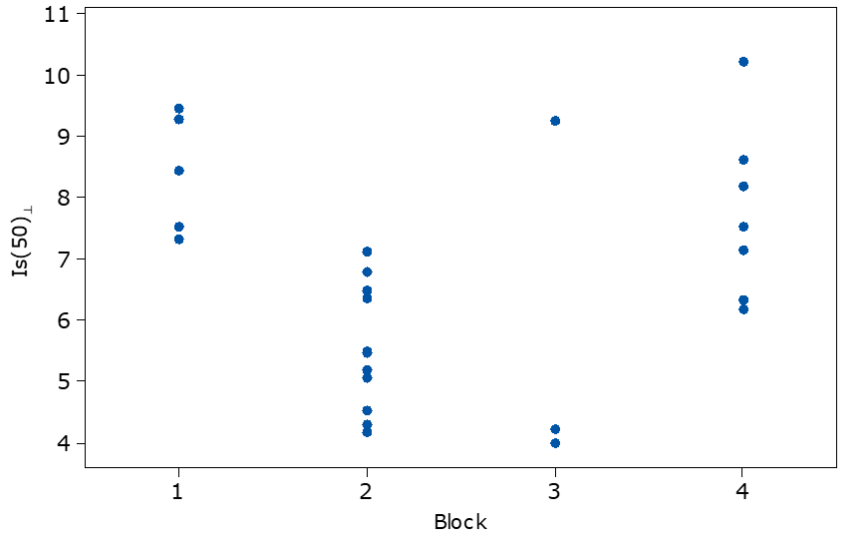

Figure 5.14: Individual value plot of the results from the axial point load tests. The results of invalid tests are not shown. The size-corrected point load index $I_{s(50)\perp}$ for specimens tested perpendicular to the main foliation is plotted versus the block number.

5.2.3.2 Uniaxial compression test

The results of the uniaxial compression tests are summarised in Table 5.6. The same results are shown graphically in Fig. 5.15, while Fig. 5.16 shows the stress-strain curves for all tests. Figures 5.17 and 5.18 show the specimens after the tests were completed. The Young's modulus and Poisson ratio are tangent values at 50 % axial stress level. At this stress level, the stress-strain curves are straight, indicating that the specimens behave linear elastically. In addition to the uniaxial compressive strength and deformability properties, the density and P-wave velocity were also determined, with results as shown in Table 5.6.

The specimens generally failed in shear, but the failures were influenced by the presence of a second foliation. Specimen 1.3 failed in a combination of shear and axial cleavage. Specimen 1.4 failed along a surface that did not cut the entire specimen. This specimen remained one piece after the test. The remaining specimens failed in shear, along surfaces with orientations that seemed to be influenced to various degrees by a second foliation. The angle of failure stated in Table 5.6 refers to the angle between the failure surface and the core axis of the specimen. For specimen 1.3 the angle was measured on the parts of the failure surface that failed in shear (i.e., it is not the average angle due to a combination of shear and axial cleavage). Most specimens behaved in a brittle manner, fairly typical to metasandstone. Failure occurred suddenly, and was accompanied by a loud cracking sound. Also, the graph of axial stress versus axial strain displayed little curving prior to failure.

Table 5.6: Results of the uniaxial compression tests. The results include failure angle, tangent Young's modulus and Poisson ratio at 50 % axial stress level, and UCS. Density and P-wave velocity are shown in the final columns. The two final rows show the means and standard deviations for each block. The crossed out value is regarded an outlier, and is not included in the calculation of the mean and standard deviation.

Specimen	Failure angle	Young's modulus E_{50}	Poisson ratio ν_{50}	UCS	Density	P-wave velocity
		GPa		MPa	kg m^{-3}	m s^{-1}
1.1	24°	48.7	0.38	151	2.712	5239
1.2	43°	48.8	0.26	115	2.713	5119
1.3	54°	50.0	0.23	104	2.711	5213
1.4	-	51.3	0.32	123	2.713	5118
1.5	31°	53.9	0.33	129	2.711	4781
4.1	40°	43.5	0.32	122	2.755	5224
4.2	35°	40.3	0.35	129	2.757	5224
4.3	46°	44.3	0.41	112	2.752	5200
4.4	44°	46.3	0.32	~~72.4~~	2.753	5108
Block 1	38°±13°	50.5±2	0.30±0.06	124±18	2.712±0.001	5094±183
Block 4	41°±5°	43.6±2	0.35±0.04	121±25	2.754±0.002	5189±55

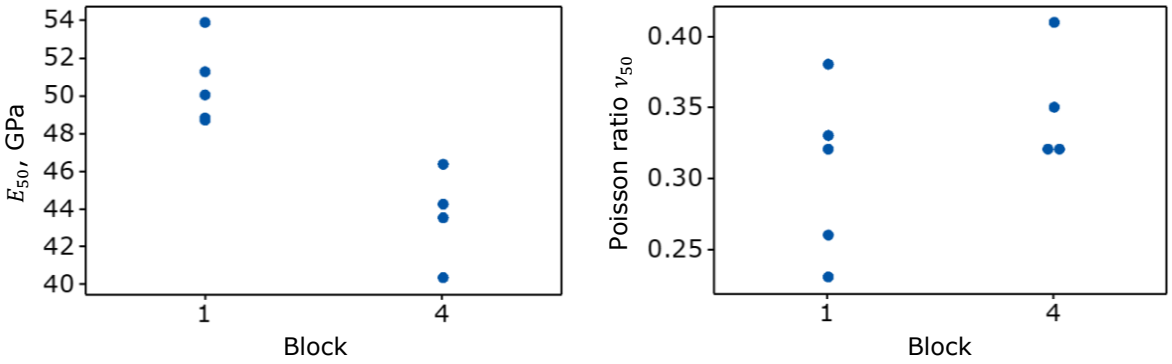

a) Tangent Young's modulus **b) Tangent Poisson ratio**

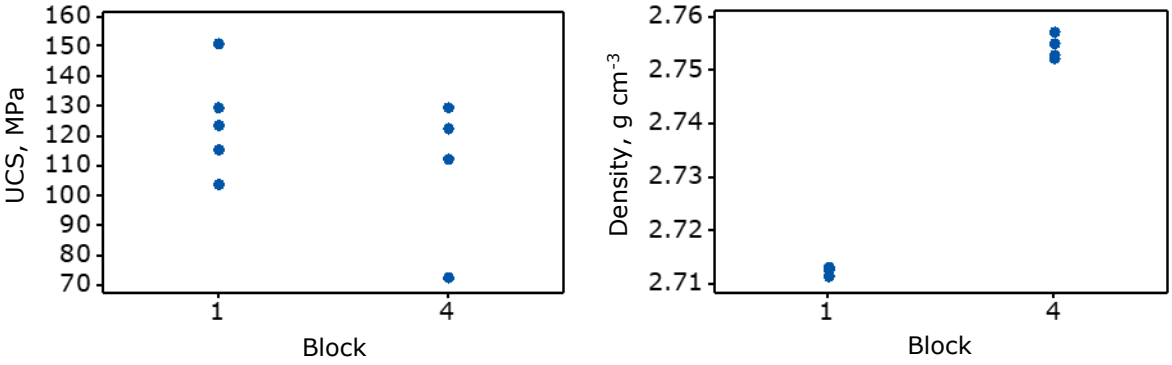

c) Uniaxial compressive strength **d) Density**

Figure 5.15: Individual value plots of the results from the uniaxial compression tests. The figure shows: a) tangent Young's modulus at 50 % axial stress level, b) tangent Poisson ratio at 50 % axial stress level, c) uniaxial compressive strength, and d) density.

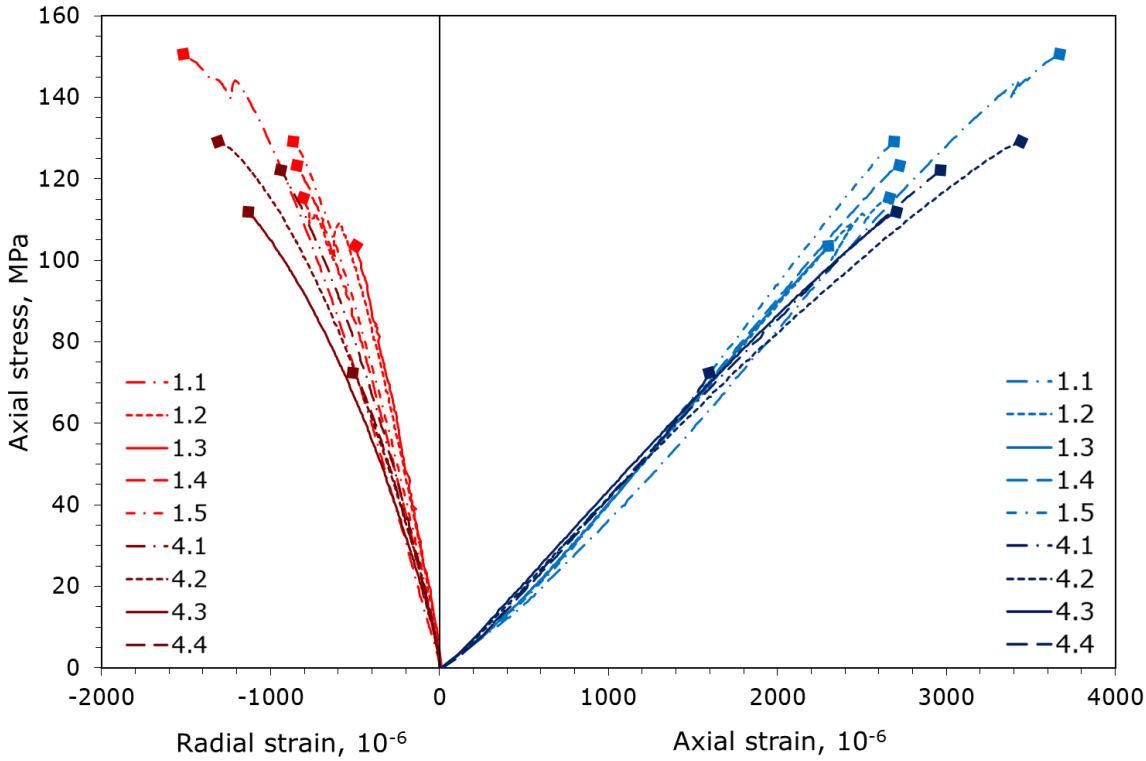

Figure 5.16: Stress-strain curves for the uniaxial compression tests. Failure is indicated by a square at the end of each curve.

Figure 5.17: Photo of specimens 1.1–1.5 (from left to right) after the uniaxial compression tests. The specimens have generally failed in shear along surfaces influenced to various degrees by a second foliation. Specimen 1.3 failed in a combination of shear and axial cleavage. Note the scarcely visible failure surface down the centre of specimen 1.4.

Figure 5.18: Photo of specimens 4.1–4.4 (from left to right) after the uniaxial compression tests. The specimens have generally failed in shear along surfaces influenced to various degrees by a second foliation.

5.2.4 Analysis and Discussion

5.2.4.1 Point load test

The results from the point load tests illustrate that there are differences between the strengths of the rocks found in the R1. Blocks 1 and 4 seem to have similar strength properties, while block 2 is weaker. There are not enough valid results for block 3 in the axial direction to draw firm conclusions regarding this block, but based on the diametral tests, this block seems to have properties more similar to block 2 than to blocks 1 and 4. These results are not very surprising, as blocks 1 and 4 were very similar in appearance, while block 2 was more schistose and had a higher content of mica. The appearance of block 3 was somewhere between block 2 and blocks 1 and 4. The strength anisotropy index indicates significant anisotropy for all blocks.

The axial tests proved difficult to carry out successfully, as a large portion of the tests resulted in invalid modes of failure. This was particularly the case for specimens from blocks 1 and 3. The axial tests on specimens from these blocks tended to result in a failure surface that did not go through both loading points. Instead the failure surface intersected one loading point and went at an angle to the perimeter of the core. The consistency in the mode of failure indicates that a second direction of weakness, non-perpendicular to the axis of the core, was present. Under close inspection this direction of weakness could be observed with the naked eye as vague stripes. In block 1, this second foliation tended to be parallel or sub-parallel to the quartz bands, and some of the failure surfaces followed these bands. Tests on specimens from blocks 2 and 4 resulted mostly in valid modes of failure. However, the failure surfaces in specimens from block 2 tended to be jagged, partly following the small-scale folds (Fig. 5.19). Overall, these observations suggest that there are at least two directions of weakness. It is uncertain whether the orientation of the cores is such that the test captured the strongest and weakest directions.

Figure 5.19: Typical mode of failure for axial point load tests on specimens from block 2.

5.2.4.2 Uniaxial compression test

The uniaxial compression tests support the conclusion drawn from the point load tests that blocks 1 and 4 have similar strength properties. When the result from specimen 4.4 is discarded as an outlier, the means for the two blocks differ by only 2 %. The stiffness and the density, however, seem not to be equal for the two blocks, as illustrated by the individual value plots in Fig. 5.15.

The results of the uniaxial compression tests are used for selection of undisturbed intact rock properties for the DE model. The parameters chosen are assumed to be representative for the low-grade metamorphosed metasandstone. The values will not apply to the more schistose rock represented by block 2. The representative values from the uniaxial compression tests are not calculated by averaging the values for the individual specimens, as this would make block 1 more influential than block 4. Rather, the means for the two blocks are averaged, such that both blocks have the same influence. The representative values are shown in Table 5.7.

As was the case for the point load test, the results from the uniaxial tests raises the question of whether it is really the strongest direction that has been tested. For one thing, the angle between the failure surface and the axis of the cores was very high for several of the specimens. Usually one would expect this angle to be approximately 30°, while here the average is 40°. Also, parts of the failure surfaces were quite smooth. These observations suggest that the failures were influenced by a foliation that was not perpendicular to the core axes. Furthermore, dividing the uniaxial compressive strength with the point load index, a ratio of 15 is obtained when the results for blocks 1 and 4 are combined. If the results are not combined, a ratio of 15 is obtained for block 1, and a ratio of 16 is obtained for block 4. These numbers are low, as the ratio is typically in the range 20–25 (Franklin, 1985). One reason for the low ratio might be that the results of the uniaxial compression tests were influenced by the non-perpendicular foliation. In contrast, the results of the point load tests that were most severely influenced by this foliation were discarded due to an invalid mode of failure. The invalid modes of failure resulted in rejection of some of the lowest values of the point load index. Overall, the conclusion is that the rock contain at least two directions of weakness. There exist a possibility that a higher UCS would have been measured if the orientation of the cores had been rotated such that the influence of the second direction of weakness had been reduced. Combined with the anisotropy expressed through the strength anisotropy index, this makes the representativeness of the stiffness properties and the UCS in Table 5.7 uncertain.

Finally, a comment is made on the excellent agreement between the results from the uniaxial compression tests and the Schmidt hammer rebound tests. The JCS_0 calculated for the joint set with the highest mean rebound value (i.e., joint set J1) is exactly equal to the mean UCS. This gives credibility to the Schmidt hammer rebound test, and indicate that joint set J1 is virtually not weathered at all, while the two other joint sets are somewhat altered.

Table 5.7: Representative stiffness and strength properties for intact pieces of the metasandstone in the Gevingåsen tunnel. The values are determined based on the uniaxial compression tests.

Property	Value
Density, g cm^{-3}	2.73
Young's modulus, GPa	47
Poisson ratio	0.33
UCS, MPa	123

5.3 Joint Properties Estimated Based on the Investigations

Now that the JRC_0, the JCS_0, and the UCS of the metasandstone in the R1 are known, parameters of the Barton-Bandis joint slip model can be calculated. Firstly, the joint roughness coefficient and the joint wall compressive strength must be scaled so they apply to the scale of in situ blocks. This is done using Eqs. (2.21) and (2.22). A test scale of L_0 = 0.1 m is assumed, based on 1) the length of the profiles used to determine the JRC_0, and 2) the spatial density of the Schmidt hammer rebound measurements used to determine the JCS_0. Also the JCS_0 of joint set J1 is identical to the UCS determined in the laboratory, which applies to such a scale. An in situ block size of L = 2 m is assumed, based on the observations made in the field. This results in the in situ scale JRC and JCS shown in Table 5.8. Next, the residual angles of friction can be estimated. A residual angle of friction of 30° is assumed for joint set J1. This value is obtained from tables published by NGI (2017), based on the observed joint alteration number J_a. The value is typical for unaltered joints with surface staining only. Residual angles of friction of 24° and 25° are obtained for joint sets J2 and J3 respectively, calculated as suggested by Barton and Choubey (1977) with the normalised Schmidt hammer rebound value relative to that of set J1, whose angle of friction is assumed to be equal to the basic angle of friction. Finally, the joint normal stiffnesses and joint shear stiffnesses are estimated by Eqs. (2.23)–(2.28). Assuming that the effective joint normal stress is 2.3 MPa, the results are as shown in Table 5.8. The normal stress level will be discussed later, together with other input parameters for the simulations.

Table 5.8: Joint mechanical properties estimated based on the results from the field and laboratory investigations. The table shows in situ scale JRC and JCS, residual angle of friction, tangent normal stiffness for interlocked and mismatched joints, and peak shear stiffness.

Set	JRC	JCS	ϕ_r	$K_{n,int.}$	$K_{n,mism.}$	K_s
		MPa		GPa m^{-1}	GPa m^{-1}	GPa m^{-1}
J1	5	60	30°	93	32	0.32
J2	5	27	24°	25	10	0.24
J3	5	32	25°	30	12	0.25

6 Finite Element Modelling

Preliminary numerical modelling has been performed with the two-dimensional FE software *RS2 9* (Rocscience Inc., 2019). As *RS2* is a FE software, the rock mass is modelled as a continuum, and flow is modelled by matrix fluid flow (Section 2.3.1). Joints can be represented with interface elements, but with certain limitations (Section 2.6). Here, joints will not be included explicitly. Rather, their effect will be incorporated in the rock mass stiffness, using the GSI of the rock mass.

The aim of the FE modelling is to: 1) back-calculate the hydraulic conductivity increase within the CDZ in order to later implement this in the DE model, and 2) make preliminary assessments regarding the induced stress field around the tunnel. Although, the reason for using DE modelling in this study is the belief that FE modelling is inadequate for simulating the groundwater flow in the jointed hard rock in the Gevingåsen tunnel, results from the FE modelling is still expected to be useful for preliminary assessments. Also, the calculation times in *3DEC* are too long to rely only on DE modelling for calibration of the model with respect to the hydraulic properties of the CDZ.

This chapter has three parts. The first section, Section 6.1, describes the FE model setup. Next, Section 6.2 presents the results. Finally, Section 6.3 summarises the main findings of relevance to the DE modelling.

6.1 Model Setup

6.1.1 Geometry

The basis of the FE model is a rectangle with dimensions 200×170 m. The longest axis points in the horizontal direction. The upper boundary is assumed to coincide with the terrain surface, situated 60 m above the tunnel crown. This overburden is representative for the area investigated during the field investigations, but it is slightly larger than the overburden in the area where Holter et al. (2015) performed their groundwater pressure measurements.

The tunnel geometry is based on the guidelines for single-track railway tunnels in the technical design basis for intercity routes published by Bane NOR (2017). Simplifications are made to ease the implementation in the numerical software (both *RS2* and *3DEC*). The tunnel width is 9.3 m. The walls of the tunnel are vertical to a height of 5.35 m. Above this level, the tunnel is closed by a semi-circular crown. The height of the tunnel at the centre line is 10 m. The centre of the tunnel invert is positioned at the model origin.

The tunnel is surrounded by a set of material boundaries. These are used to assign different material properties to the CDZ than to the rest of the model. The material boundaries are concentric with the tunnel, have similar shape, and are positioned 0.1, 0.2 and 0.4 m from the excavation boundary. Additional boundaries are used to control the mesh density.

The rock support comprises bolts and SCL in the tunnel walls and crown. The spacing between each bolt is 2 m (both in-plane and out-of-plane), and the bolt length is 3 m (Fig. 6.1). This bolt pattern is typical for the support in the Gevingåsen tunnel in sections with fair rock mass quality (NNRA, 2009). It also agrees with the bolt pattern suggested by the Q-system for the conditions found during the field investigations (Section 5.1.2.1).

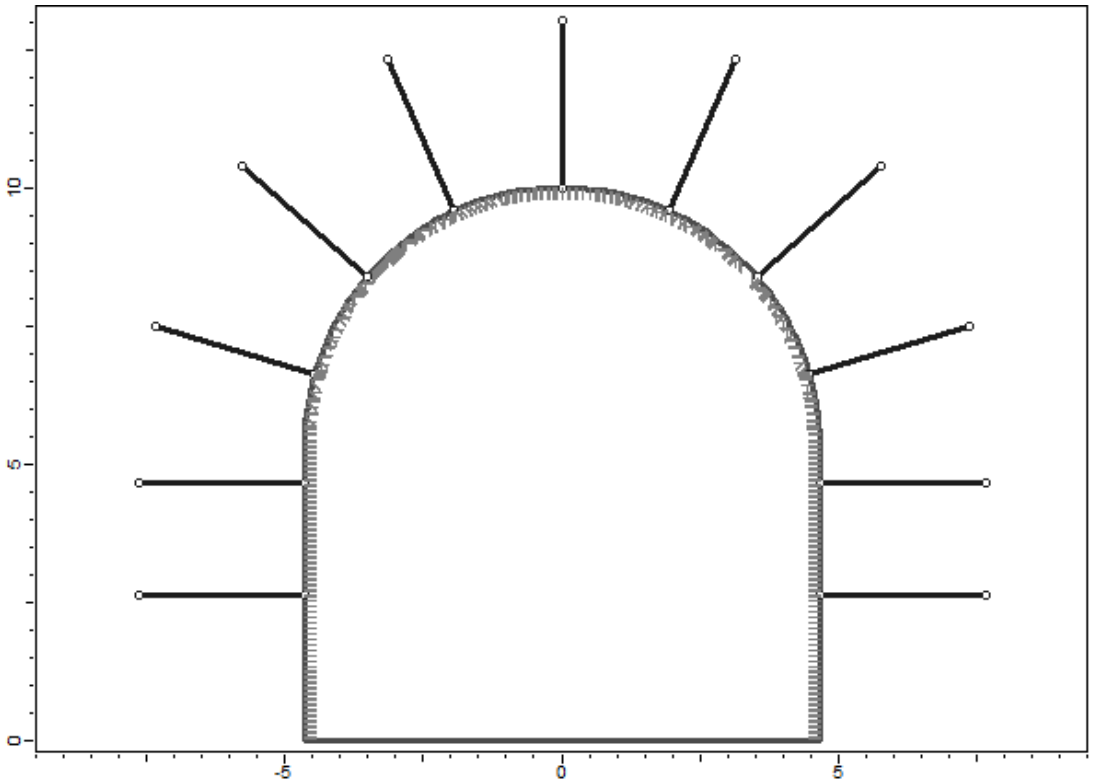

Figure 6.1: Tunnel geometry in the FE model, including bolts and SCL. Dimensions are in metres.

6.1.2 Material Properties

6.1.2.1 Rock mass properties

As the rock mass is of fair quality and the in situ stresses are relatively low, elastic behaviour is expected to dominate. Also, the rock mass contains three joint sets with similar friction characteristics, creating near compact (equidimensional) blocks. This suggests that the behaviour might be nearly isotropic (although, as seen in Section 5.2.4.1, the strength anisotropy index suggests some anisotropy). Therefore, the rock mass is modelled as an isotropic linear elastic material, with properties as shown in Table 6.1. The consequence of using an elastoplastic material with the generalised Hoek-Brown failure criterion was initially also investigated in order to verify the assumption that elasticity dominates. The result was as expected: the rock mass behaved elastically, with little or no yielding.

The Young's modulus of the rock mass is estimated using the generalised Hoek-Diederichs equation (Eq. (2.15)). With an intact Young's modulus of 47 GPa, and a GSI of 70, the rock mass Young's modulus is estimated to be 34 GPa. Whereas many authors have investigated equations for the rock mass Young's modulus, there is relatively little literature on estimation of the rock mass Poisson ratio. Also, this author's impression is that the equations that do exist tend to give results that vary widely. For the case at hand, equations proposed in the literature gave rock mass Poisson ratios ranging from 0.25 to 0.40. Therefore, the Poisson ratio is simply assumed to be 0.33, identical to that of intact rock.

6.1.2.2 Rock support properties

The rock support properties are shown in Table 6.2. The bolts are modelled as fully bonded with no pre-tensioning force, as most of the bolts in the Gevingåsen tunnel are fully grouted bolts. The SCL is modelled as standard beams with the Timoshenko beam element formulation. Interface elements are used to represent the concrete-rock interface.

Table 6.1: Rock mass properties in the FE model. The values are obtained from field and laboratory investigations.

Property	Value
Density, kg m^{-3}	2730
Young's modulus, GPa	34
Poisson ratio	0.33

Table 6.2: Rock support properties in the FE model. Additionally, information on where the values are obtained is included.

Property	Value	Obtained from
Bolt properties		
Diameter, mm	20	DYWIDAG Norge AS (2016)
Young's modulus, GPa	210	Modulus of steel
Tensile capacity, kN	157	DYWIDAG Norge AS (2016)
Residual tensile capacity, kN	0	Assumption based on bolt type
Liner properties		
Young's modulus, GPa	29	K. G. Holter (2019, pers. comm., 15 Feb.)
Poisson ratio	0.25	Windsor and Thompson (1999)
Peak compressive strength, MPa	70	Holter (2016)
Residual compressive strength, MPa	0	Assumption
Peak tensile strength, MPa	5	Saw et al. (2013)
Residual tensile strength, MPa	0	Assumption
Thickness, m	0.1	Example value for Norwegian hard rock
Unit weight, kN m^{-3}	22	Holter (2015)
Concrete-rock interface properties		
Tensile strength, MPa	1	Bryne et al. (2014)
Peak cohesion, MPa	1.3	EPRI (1992)
Peak angle of friction	54°	EPRI (1992)
Residual tensile strength, MPa	0	Assumption
Residual cohesion, MPa	0.08	EPRI (1992)
Residual angle of friction	34°	EPRI (1992)
Normal stiffness, GPa m^{-1}	5	Mouzannar et al. (2017)
Shear stiffness, GPa m^{-1}	5	Mouzannar et al. (2017)

6.1.2.3 Effective hydraulic conductivity of the undisturbed rock mass

The effective hydraulic conductivity of the undisturbed rock mass is estimated to be approximately 1×10^{-8} m/s. This is calculated with the equation proposed by El Tani (2003). The calculation is based on the observed water conditions in the tunnel, which are assessed to be equivalent to an inflow of 5–10 l/min/100 m (K. G. Holter, 2019, personal communication, 15 February).

6.1.3 Back-Calculation of the Hydraulic Conductivity of the CDZ

The representation of the EDZ with respect to hydraulic conductivity is based on the discussion in Section 4.2, and involves an increase in the hydraulic conductivity within 0.4 m from the excavation boundary. The increase is meant to represent the damage in the HDZ and CDZ, where there is generally a significant increase in the hydraulic conductivity. Considering the relatively low in situ stresses compared to the strength of the intact rock and the rock mass, the CDZ is probably more important than the HDZ. Therefore, the term *CDZ* will be used for the region within 0.4 m from the excavation boundary, both in the FE modelling and the DE modelling.

The model CDZ is divided into regions extending 0.0–0.1, 0.1–0.2, and 0.2–0.4 m from the excavation boundary. The hydraulic conductivities of these regions are back-calculated by trial and error. Table 6.3 presents the hydraulic conductivities that result in the best agreement with the groundwater pressure measurements presented by Holter et al. (2015). The back-calculation was performed under the constraint that the relative differences between the hydraulic conductivities in the different regions (i.e., the relative differences between the values in Table 6.3) were kept constant and equal to the corresponding relative differences between the values in the seventh column of Table 4.1. In other words, the relative differences between the hydraulic conductivities in the model CDZ are equal to the ones obtained using the harmonic means of the injection test results presented by Ericsson et al. (2015). The harmonic mean was used rather than the arithmetic mean or the geometric mean because the relative difference between the hydraulic conductivities obtained by back-calculation and the hydraulic conductivity of the undisturbed rock mass (i.e., the relative difference between the values in Table 6.3 and the value 1×10^{-8} m/s) is more similar to the relative difference between the maximum and minimum values in the seventh column of Table 4.1, than to the relative difference between the values in the sixth or eighth column. However, the use of the harmonic mean should probably not be subject to extensive physical interpretation, as the investigation reviewed in Section 4.2 was executed at a different location, with other site conditions.

The damage is assumed to be equal in the invert, walls, and crown. Scenarios with lower hydraulic conductivity in the walls and crown than in the invert were initially investigated. Such a difference is plausible as the blast damage is expected to be less severe in the walls and crown than in the invert, due to less heavy explosive charging during excavation. However, the observed effect was found to be due, mostly, to the reduction in the walls and crown, rather than to any difference as such between walls/crown and invert. The reason is that the water enters the tunnel after only a short distance of flow in the invert-part of the CDZ, thus making the hydraulic conductivity in the invert less important than the one in the walls and crown. Therefore, it was found to be unnecessary to distinguish between the hydraulic conductivities in the walls/crown and the invert.

6.1.4 Virgin Stress Field

In both the FE modelling and the DE modelling, two scenarios regarding the virgin stress field are included (Table 6.4):

1) An isotropic stress field where the stresses are higher than the gravitational vertical stress. Specifically they are equal to 3 MPa at the origin (i.e., at the level of the tunnel invert), with a gravitational gradient in the z-direction.
2) A stress field where the vertical stress is gravitational while the horizontal stress is twice the vertical (both in-plane and out-of-plane).

Table 6.3: Hydraulic conductivities in the CDZ, back-calculated using the pressures reported by Holter et al. (2015).

Region	Hydraulic conductivity
m	m s^{-1}
0.0–0.1	8×10^{-7}
0.1–0.2	3×10^{-7}
0.2–0.4	1×10^{-7}

Table 6.4: Stress field scenarios for the FE simulations. Two scenarios are defined: one with an isotropic stress field with elevated vertical stress compared to the gravitational one, and one with gravitational vertical stress and a total stress ratio of two.

Property	Stress field scenario	
	1	2
Vertical stress at the origin, MPa	3	1.9
Horizontal stress at the origin, MPa	3	3.8
Unit weight of overburden, MPa/m	0.0273	0.0273
Total stress ratio (in-plane and out-of-plane)	1	2

Scenario 1 was chosen based on the information presented in Section 4.1. The topography of the studied area has reasonably low relief, and is assumed to have little influence on the stress field. The studied tunnel section is located west of the Hommelvikvollen ridge, in gentle terrain. The gravitational vertical stress at the location studied in this thesis is calculated by assuming an average overburden density of 2730 kg/m^3. The theoretical vertical stress at the level of the tunnel invert is then 1.9 MPa. Based on the discussion in Section 4.1, this value may be too low. It is assumed that the vertical stress is approximately 1 MPa higher than the theoretical one, and that the horizontal stress is of similar magnitude (as assumed by O.T. Blindheim AS in relation to the excavation of the Ladehammeren purification plant). Therefore, an isotropic stress of 3.0 MPa at the level of the tunnel invert was chosen for scenario 1. Stress field scenario 2 has a higher deviatoric stress than scenario 1, but the mean stress is approximately equal. Scenario 2 constitutes a reasonable stress field based on general knowledge about the stresses at shallow depths in the earth's crust (e.g., Hoek, 2006a). The mean stress is kept unchanged from scenario 1, as a higher mean stress would lead to higher joint normal stiffnesses in the DE model (Section 7.1).

The stress magnitude and principal stress directions may, in reality, deviate from the ones assumed above for a number of reasons. For example, there is a pronounced weakness zone defining the valley of the river Homla that might influence the stress field. Accurately determining the in situ stress field is not possible without performing in situ stress measurements.

The virgin pore pressure is assumed to be hydrostatic from a groundwater table at terrain level, that is, 60 m above the tunnel crown. This is a reasonable assumption as the studied tunnel section is situated in gentle terrain to the west of the Hommelvikvollen ridge. Southeast of the ridge there are marshy regions and a lake (Hommelviktjønnin), indicating that the groundwater table may be located close to the terrain surface. In general, the groundwater table will be close to the terrain below valleys, and relatively deeper below hills. With the assumption that the groundwater table coincides with the terrain surface, the hydrostatic pore pressure at tunnel depth is 0.6–0.7 MPa.

6.1.5 Mesh Setup

The mesh in the FE model consists of six-noded triangular elements. Different mesh densities are used in the different model regions, with decreasing density when moving from the tunnel boundary towards the outer model boundary. More specifically the element length is uniformly 0.05 m within 0.6 m from the tunnel periphery, and uniformly 0.1 m between 0.6 and 2 m from the tunnel periphery. It then increases gradually to 0.7 m in the region with outer boundaries at a distance of 10 m from the excavation boundary. In the remaining model the mesh is graded with a gradation factor of 0.02. The effect of small changes in the mesh density was investigated, and found to be unimportant.

6.1.6 Boundary Conditions

The mechanical boundary conditions are chosen such that the upper model boundary represents the terrain surface, which is approximated as flat. The upper boundary is free, the side boundaries are normally fixed, and the lower boundary is fully fixed.

The flow boundary conditions have been chosen such as to represent no drawdown of the groundwater table, that is, constant head on all boundaries. To model the partly drained situation, a zero pore pressure boundary condition is applied to the excavation boundary in the tunnel invert, while a zero discharge boundary condition is applied to the excavation boundary in the walls and crown.

6.1.7 Calculation Stages

The simulations are performed in three stages:

- Stage 1: Initial stage. Initial mechanical equilibrium is established.
- Stage 2: Tunnel advancement stage. The tunnel is excavated and replaced by an internal pressure equal to 75 % of the field stress vector, to model the effect of tunnel advancement (Section 6.1.7.1).
- Stage 3: Final stage. Lining and bolts are installed and the internal pressure is removed (i.e., the excavation face no longer provides any support).

Each of these main stages include some manner of pore pressure calculation. In the first two stages, the pore pressure field is hydrostatic and generated directly based on the groundwater table. In the final stage the pore pressures are calculated by a steady state flow calculation. There is one-way coupling between pore pressures and deformations: the pore pressure affect the deformations, but not vice versa. Consequently, the results of the flow calculations will be independent of the mechanical calculations, and also independent of the virgin stress field.

6.1.7.1 Simulating tunnel advancement

During the tunnel advancement stage, a pressure is applied to the interior of the excavation boundary, to allow some deformation to occur before the rock support is installed. The magnitude of the internal pressure is chosen based on consideration of the behaviour of a circular tunnel in an elastic medium with isotropic virgin stress σ_0. Before excavation the stress σ_0 acts on the excavation boundary from both sides (i.e., internally and externally). Assume that the internal pressure is then reduced to some value p_i. According to elastic theory, the inward radial displacement d of the tunnel wall is linearly dependent upon p_i:

$$\frac{d}{d_{max}} = 1 - \frac{p_i}{\sigma_0} \tag{6.1}$$

where d_{max} is the maximum displacement, obtained when the internal pressure is completely removed.

Equations for the radial displacement of a tunnel as a function of the distance x from the tunnel face are readily available in the literature (Table 6.5). Such equations describe the so-called longitudinal displacement profile (LDP). It is here assumed that the rock support is installed close to the tunnel face. Therefore, the value d/d_{max} at the tunnel face is of interest. This deformation is converted to an internal pressure using Eq. (6.1). Using, for example, the solution by Panet (1995), the relative displacement is 25 % at the tunnel face. For an elastic medium, this corresponds to $p_i = 0.75\sigma_0$. Note that this value is conservative. The support is rarely applied immediately behind the tunnel face. Often deformations will be in the range 35–45 % before support is installed (Rocscience Inc., n.d.).

Table 6.5: Analytical solutions for the LDP. The LDP is expressed as relative displacement as a function of the distance x from the face. $x < 0$ is the region in front of the face (not excavated), while $x > 0$ is behind the face (excavated). r is the tunnel radius, and r_p is the plastic radius. Adapted from Paraskevopoulou and Diederichs (2018) with permission.

Reference(s)	Deformation (LDP)	Medium	Value at face
Panet and Guenot (1982), Panet (1993)	$\frac{d_x}{d_{max}} = 0.28 + 0.72\left[1 - \left(\frac{0.84}{0.84+x/r}\right)^2\right]$	Elastoplastic	0.28
Corbetta et al. (1991)	$\frac{d_x}{d_{max}} = 0.29 + 0.71\left[1 - \exp\left(-1.5\left\{\frac{x}{r}\right\}^{0.7}\right)\right]$	Elastic	0.29
Panet (1995)	$\frac{d_x}{d_{max}} = 0.25 + 0.75\left[1 - \left(\frac{0.75}{0.75+x/r}\right)^2\right]$	Elastic	0.25
Chern et al. (1998), Carranza-Torres and Fairhurst (2000)	$\frac{d_x}{d_{max}} = \left[1 + \exp\left(-\frac{x}{1.1r}\right)\right]^{-1.7}$	Elastoplastic	0.31
Unlu and Gercek (2003)	$\frac{d_x}{d_{max}} = \begin{cases} \frac{d_0}{d_{max}} + A_a\left[1 - \exp\left(B_a\frac{x}{r}\right)\right] & \text{for } x < 0 \\ \frac{d_0}{d_{max}} = 0.22\nu + 0.19 & \text{for } x = 0 \\ \frac{d_0}{d_{max}} + A_b\left[1 - \left(\frac{B_b}{B_b+x/r}\right)^2\right] & \text{for } x > 0 \end{cases}$ $A_a = -0.22\nu - 0.19,\ B_a = 0.73\nu + 0.81$ $A_b = -0.22\nu + 0.81,\ B_b = 0.39\nu + 0.65$	Elastic	0.26 for $\nu = 0.33$
Vlachopoulos and Diederichs (2009)	$\frac{d_x}{d_{max}} = \begin{cases} \frac{d_0}{d_{max}} e^{x/r} & \text{for } x < 0 \\ \frac{d_0}{d_{max}} = \frac{1}{3}e^{-0.15r_p/r} & \text{for } x = 0 \\ 1 - \left(1 - \frac{d_0}{d_{max}}\right)\exp\left(\frac{-3x/r}{2r_p/r}\right) & \text{for } x > 0 \end{cases}$	Elastoplastic	0.29 for $r_p = r_0$

6.2 Results

Three types of results from the FE simulations are presented. Firstly, the hydraulic conductivity assigned to the undisturbed rock mass is verified by calculating the inflow to an imaginary tunnel with no water control. Next, the pore pressure in the area immediately surrounding the SCL are presented. Finally, induced stresses are investigated.

6.2.1 Verification of the Estimated Effective Hydraulic Conductivity

Figure 6.2 illustrates that the hydraulic conductivity assigned to the undisturbed rock mass gives the correct magnitude of inflow. The figure shows a flow net with equipotential lines and flow lines. Four discharge sections that together enclose the tunnel are shown. The sum of the discharge through the four sections gives a total inflow of 8.5 l/min/100 m (i.e., as intended). In Fig. 6.2, the increased hydraulic conductivities in the CDZ have not yet been included. Including the CDZ leads to a slight increase in the inflow. However, the inflow is still of the intended order of magnitude.

6.2.2 Pore Pressures

Based on the measurements performed by Holter et al. (2015), a pressure of 0.05–0.2 MPa is expected in the crown and upper walls of the tunnel. Without any hydraulic conductivity increase within the CDZ, the steady state pore pressure after excavation is too high, with a value of 0.37 MPa at the centre of the crown (Fig. 6.3). Acceptable agreement is obtained with the back-calculated hydraulic conductivities (Table 6.3), although the pressure at the centre of the crown is slightly too low (Fig. 6.4). Simultaneously obtaining both the low values at the springline, and the higher value at the centre of the crown was not possible without varying the hydraulic conductivity along the length of the crown.

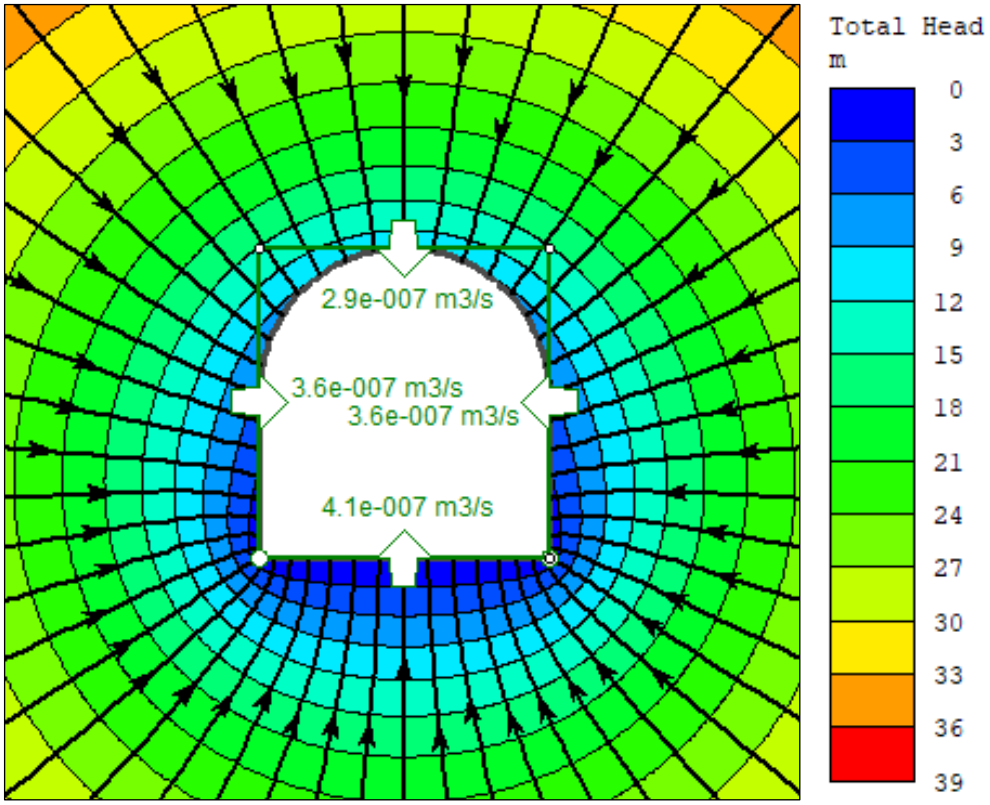

Figure 6.2: Flow net illustrating the flow towards the tunnel when there is no water control. The discharge sections reveal that the total inflow to the tunnel is 8.5 l/min/100 m. Flow directions are indicated with arrows.

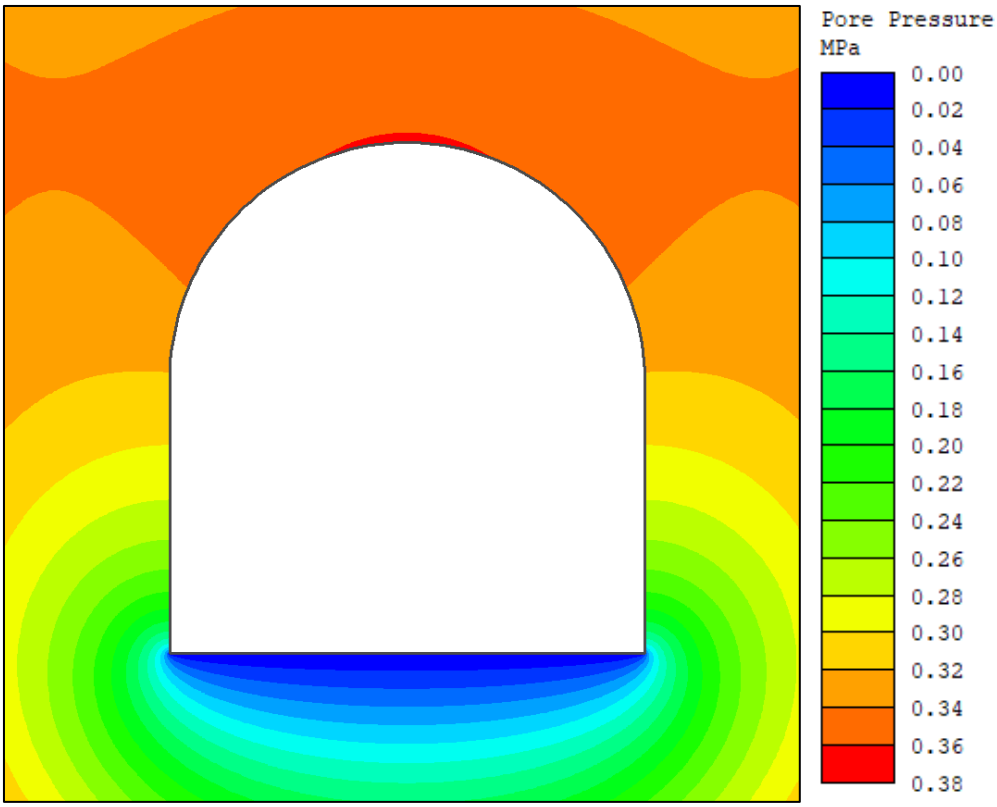

Figure 6.3: Pore pressure field around the tunnel when the hydraulic conductivity is uniform in the entire model, including the CDZ. The maximum value at the excavation boundary is 0.37 MPa at the centre of the crown.

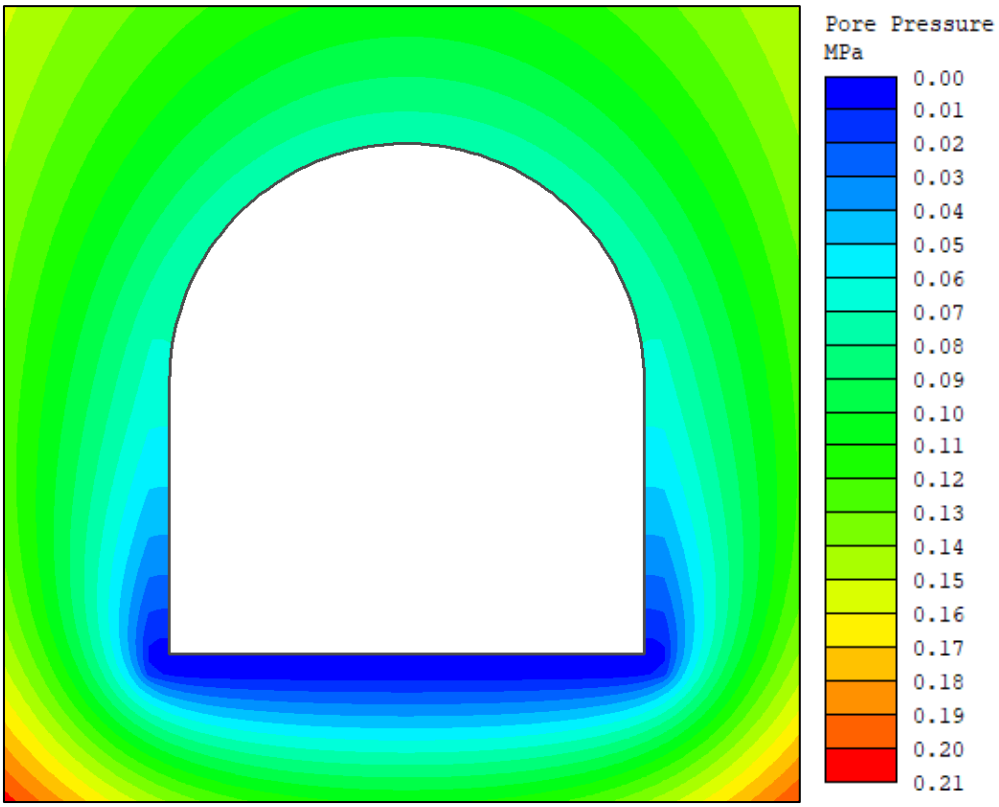

Figure 6.4: Pore pressure field around the tunnel when the hydraulic conductivities in the CDZ are back-calculated using the pressures reported by Holter et al. (2015). The hydraulic conductivities are shown in Table 6.3.

6.2.3 Induced Stresses

Figures 6.5 and 6.6 show respectively the major and minor induced principal total stress fields resulting from the FE simulations. To arrive at the presented results, the hydraulic conductivities shown in Table 6.3 were used in the CDZ. These gave the pore pressure field shown in Fig. 6.4, used for the effective stress-based mechanical analysis.

There are stress concentrations around the corners of the tunnel for both stress field scenarios (Fig. 6.5). The corners are the only areas where the stresses are sufficiently high to potentially cause any plastic rock mass behaviour, had this been allowed. There is also stress concentration in the crown. For scenario 1, which have an isotropic virgin stress field, the induced stress is relatively uniform along the entire length of the crown (Fig. 6.5a). For scenario 2, with a total stress ratio of two, the stress concentration is more severe at the centre of the crown (Fig. 6.5b). Stress concentration and resulting joint closure at the centre of the crown may explain the higher groundwater pressure measured by Holter et al. (2015) at this location.

Stress field scenario 2, which has the most pronounced stress concentration in the crown, also has large low-stress areas in the walls (Figs. 6.5 and 6.6). The low-stress areas extend several metres into the surrounding rock mass. For scenario 1, the low-stress areas are less prominent, and extend a comparably short distance into the surrounding rock mass. The differences between the induced stress fields obtained by FE modelling indicate that different induced groundwater pressure fields should be expected when both stress fields are included in the DE simulations.

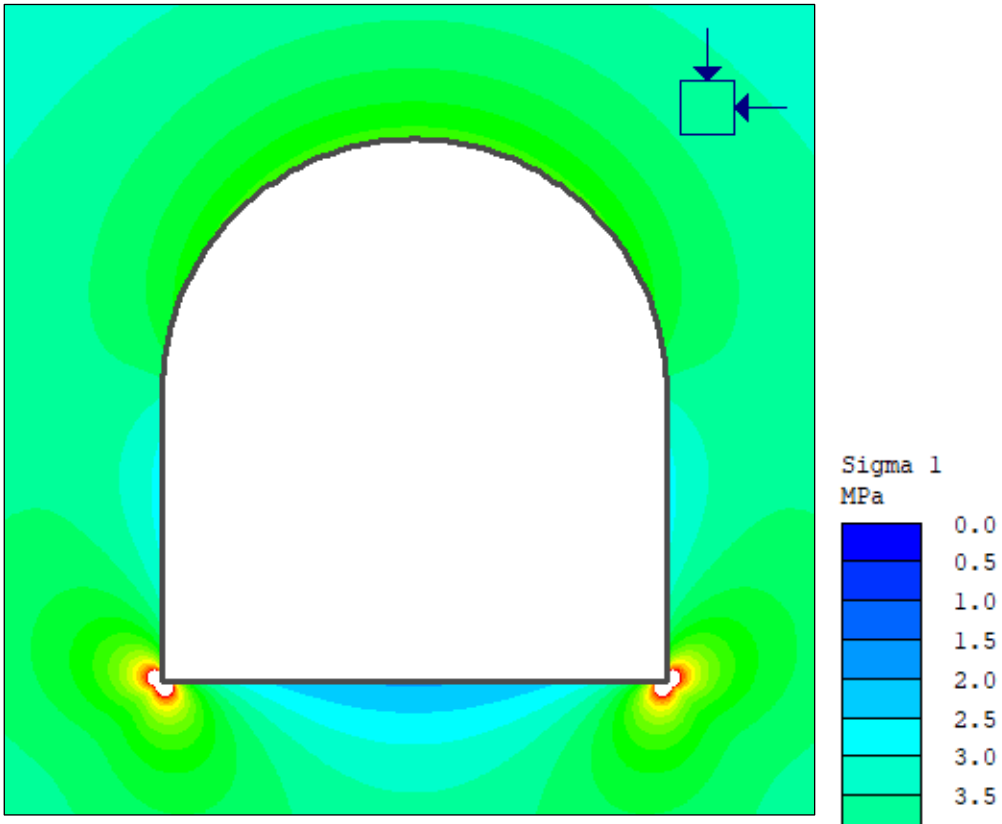

a) Stress field scenario 1. Maximum value: 43.1 MPa.

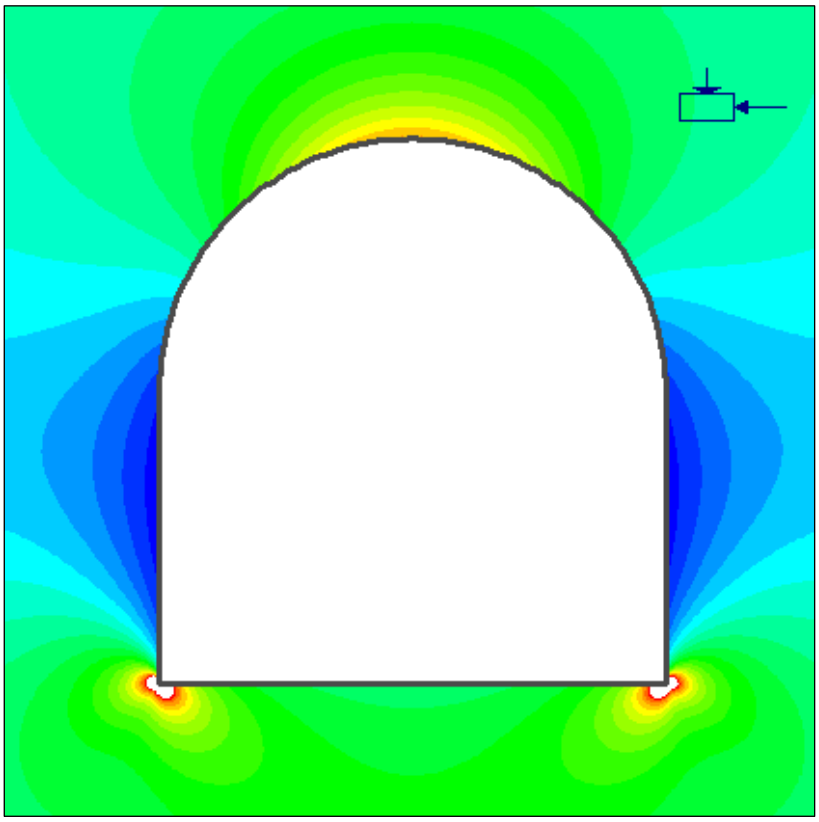

b) Stress field scenario 2. Maximum value: 39.8 MPa.

Figure 6.5: Major induced principal total stress for the two stress field scenarios. The figure shows: a) scenario 1 and b) scenario 2. The relative magnitude of the virgin stresses is indicated by the stress block in the upper right corner of each figure.

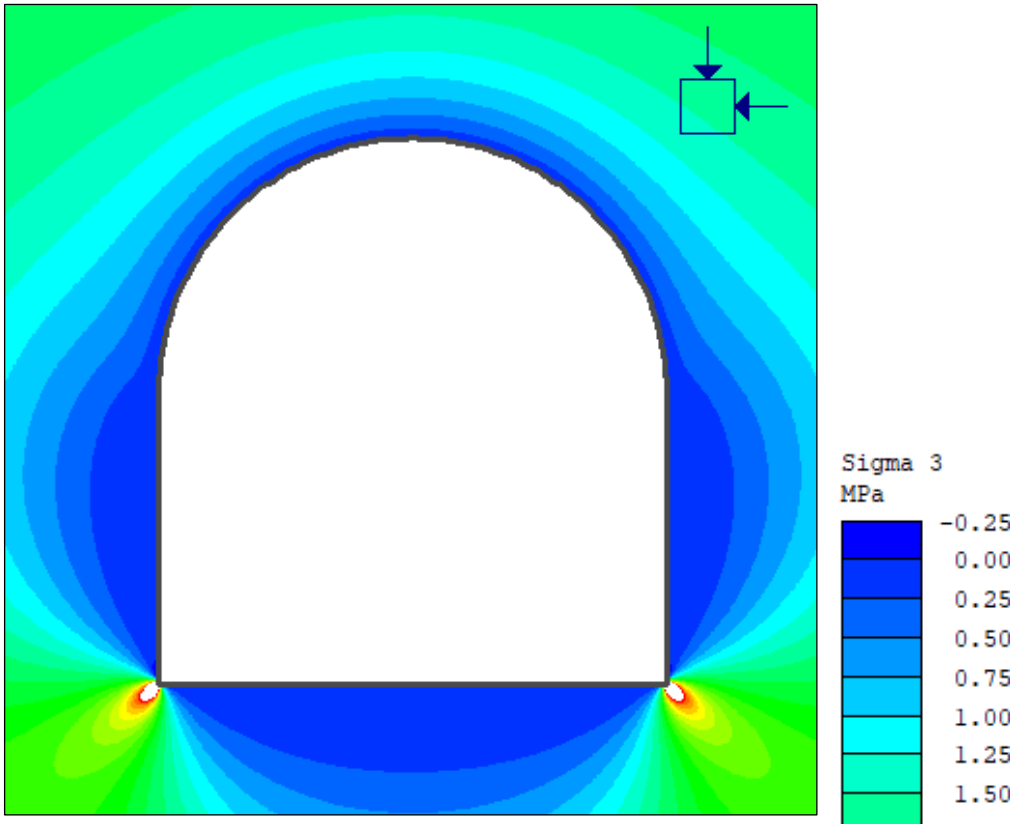

d) Stress field scenario 1. Min: -4.6 MPa, max: 19.1 MPa.

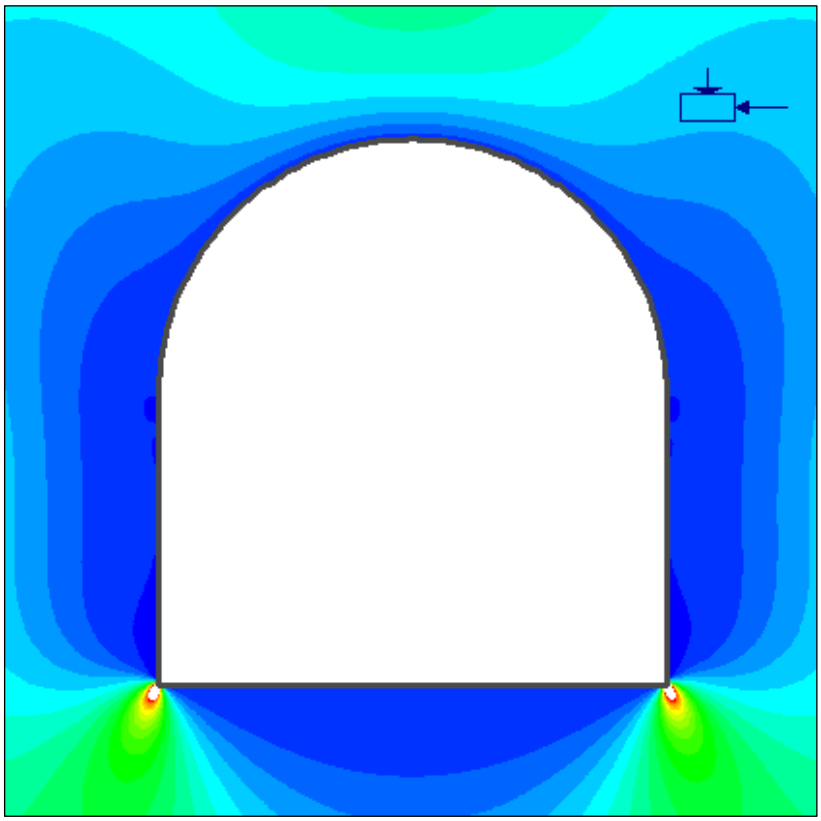

c) Stress field scenario 2. Min: -4.2 MPa, max: 16.9 MPa.

Figure 6.6: Minor induced principal total stress for the two stress field scenarios. The figure shows: a) scenario 1 and b) scenario 2. The relative magnitude of the virgin stresses is indicated by the stress block in the upper right corner of each figure.

6.3 Conclusions

Based on the FE simulations, the following conclusions are drawn:

- To reproduce the groundwater pressures measured by Holter et al. (2015), the hydraulic conductivity in the CDZ needs to be between one and two orders of magnitude higher than the effective hydraulic conductivity of the undisturbed rock mass.
- There is no need to include any difference between walls/crown and invert, with respect to hydraulic conductivity in the DE model, as the difference as such is not of primary importance.
- Elastic material behaviour is adequate for the intact blocks in the DE model, as no plastic behaviour is expected.
- Stress scenarios with total stress ratios of one and two should both be investigated by DE modelling as the latter leads to a more pronounced stress concentration in the crown, as well as larger low-stress areas in the walls.

7 Distinct Element Model Setup

This chapter describes the essential features of the three-dimensional DE model produced in *3DEC* (Itasca Consulting Group Inc., 2016a). The model geometry, material characteristics, stress field properties, mesh setup, boundary conditions, and calculation stages are described. First, however, an overview of the scenarios that will be considered in the simulations is given.

7.1 Overview of Scenarios

One of the great challenges during this study has been the long calculation time for flow calculations in *3DEC*. As only a standard *3DEC* license with a maximum of two parallel runs (one of which was, at most times, occupied by another user) was available for this study, the long calculation times severely limited the number of runs it was possible to perform within the given time frame. With this in mind it was decided to model two different scenarios for the EDZ. To get an idea about the effect of the virgin stresses, two scenarios for the stress field were included in the modelling. Hence, the parameters investigated are as follows:

- Virgin stress field scenarios (these are the same as in the FE simulations):
  1. Isotropic stress field with stresses 1.1 MPa above the gravitational vertical stress.
  2. Gravitational vertical stress and a total stress ratio of two.
- Scenarios for representation of the EDZ:
  1. No hydraulic conductivity change other than the one generated by the model itself in the form of joint normal displacements in response to stress redistribution and deformations. Construction damage is not included in this scenario.
  2. The hydraulic apertures in the region within 0.4 m from the excavation boundary are manually increased to represent effects not generated by the model. These effects are presumably mainly caused by blasting directly (i.e., they constitute damage within the CDZ).

When all permutations are included, there are at total four different scenarios. These are denoted 1.1, 1.2, 2.1, and 2.2 (Table 7.1). The first digit indicates the stress field, and the second digit indicates the representation of the EDZ (with numbers according to the list above). Note that, in the remainder of this thesis, the term *scenario* will be used in two different ways. When followed by a single digit, it will refer either to the virgin stress field *or* to the representation of the EDZ. When followed by a combination of two digits, it will refer to a specific permutation of both stress field and EDZ.

In addition to the four scenarios above, a scenario denoted the *reference scenario* is included (Table 7.1). The reference scenario consists of a single flow calculation where it is assumed that all hydraulic apertures stay unchanged from the virgin state. In effect, gradually more excavation damage is included in the simulations. The reference scenario does not include any excavation damage at all, scenarios 1.1 and 2.1 include damage that is not caused directly by the excavation works (i.e., the CDZ is not included), while scenario 1.2 and 2.2 include a CDZ.

Table 7.1: Overview of scenarios included in the DE simulations. The simulations are performed with two different virgin stress fields and two different ways of representing the EDZ, thus creating four different scenarios. In addition there is one scenario, the *reference scenario*, where a flow calculation is performed assuming that the excavation has no effect on the hydraulic apertures (i.e., there is no EDZ).

Scenario	Virgin stress field	Representation of the EDZ
Reference		Uniform hydraulic apertures, unchanged from the virgin state
1.1	Isotropic stress, 1.1 MPa larger than the gravitational vertical stress	Aperture changes generated by the model itself are included
1.2	Isotropic stress, 1.1 MPa larger than the gravitational vertical stress	Aperture increases in the CDZ are manually added in addition to changes generated by the model outside the CDZ
2.1	Gravitational vertical stress and a total stress ratio of two	Aperture changes generated by the model itself are included
2.2	Gravitational vertical stress and a total stress ratio of two	Aperture increases in the CDZ are manually added in addition to changes generated by the model outside the CDZ

As mentioned in the previous chapter, stress field scenario 2 is chosen because it has a higher deviatoric stress than stress field scenario 1, but the same mean stress. Among all stress fields with a total stress ratio of two in both horizontal directions that are considered realistic, this is the one with the lowest mean stress. It was chosen to keep the mean stress at a minimum, as it is of interest to find out whether the pressures measured by Holter et al. (2015) can be obtained with excavation damage only due to stress redistribution and deformations, that is, without damage directly caused directly by blasting (no CDZ). A higher mean stress would make the joints stiffer and, therefore, possibly result in smaller changes in joint hydraulic apertures. In the end, this could result in higher joint pressures at the excavation boundary. Of course, a stress field with higher mean stress, but the same total stress ratio, might have caused larger changes in the joint normal stresses between the final and initial states. This could have countered the effect of stiffer joints. Therefore, if more time had been available, an anisotropic stress field with higher mean stress would have been included in the simulations.

In scenario 2 for the representation of the EDZ, the hydraulic apertures within the CDZ vary with distance from the excavation boundary, but are nearly independent upon the position along it (Section 7.3.2.2). The scenario assumes that the hydraulic apertures after blasting are uniform along the excavation boundary in the walls and crown. In other words, the effect of factors other than the construction damage is not considered within the region representing the CDZ. Whether or not this is realistic can be discussed. It is difficult to say how construction damage and other factors will interact in reality. If more time had been available, other ways of implementing the CDZ could also have been investigated.

7.2 Geometry

7.2.1 Outer Boundaries

The base geometry of the DE model is an 80×80×70 m box (Fig. 7.1). The size of the model is chosen such that the distance from the excavation boundary to the model edge is more than 30 m in all directions in the tunnel cross-sectional plane. This length corresponds to three times the tunnel height, and is judged an acceptable compromise between

locating the model boundaries sufficiently far from the tunnel, and keeping the calculation times within an acceptable limit.

7.2.2 Joint Sets

Based on the field investigations (Section 5.1), three joint sets are represented in the model. These are (with dip/dip direction in real space):

- Set J1: 06°/211°
- Set J2: 80°/076°
- Set J3: 67°/349°

Similar to the model size, the joint spacing in the model was weighed against the calculation times. The spacing of joints in sets J1 and J2 is the double of the maximum spacing indicated in Section 5.1.3. For joints in set J3, the spacing is four times as large as in Section 5.1.3. Thus, the spacing is 2 m for sets J1 and J3, and 3 m for set J2. Compared to the tunnel span of 10 m, the joints are probably spaced closely enough to capture the essential mechanical behaviour of the blocks. With regards to the hydraulic behaviour, the excessive spacing is justified assuming that its effect is offset by the excessive persistence.

The representation of the joint sets is deterministic, with constant spacing and orientation, and infinite persistence. It was attempted, at an early stage, to create a model with stochastic features, maybe including a discrete fracture network (DFN). This attempt was abandoned in order to keep the number of model variables to a minimum. The joint geometry with deterministic joint sets creates a model that is easy to analyse.

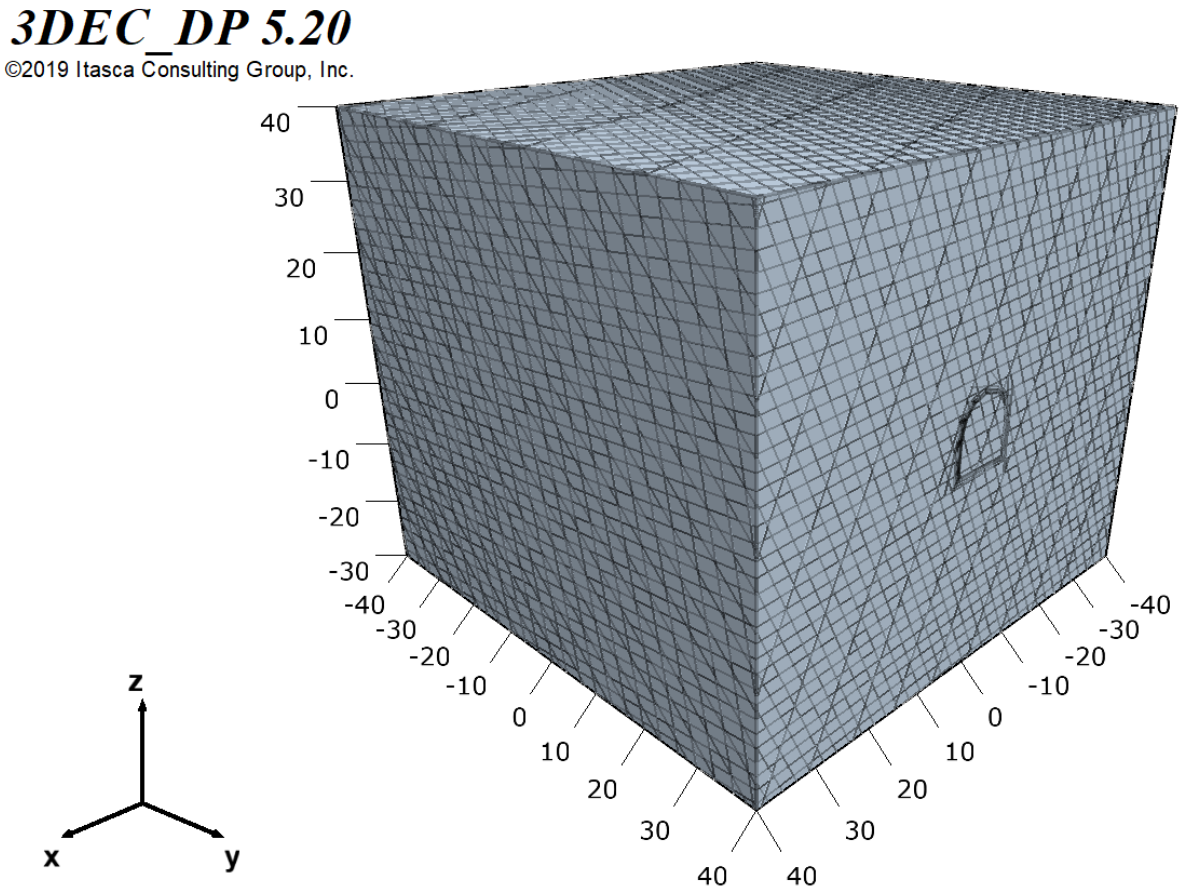

Figure 7.1: DE model geometry, showing the outer model boundaries and the three joint sets. The outline of the tunnel is also visible. Dimensions are shown in metres relative to the origin, which is positioned at the centre of the tunnel invert.

7.2.3 Tunnel and CDZ

The tunnel geometry is, as in the FE model, based on the guidelines for single-track railway tunnels in Bane NOR's technical design basis for intercity routes (Bane NOR, 2017). In the DE model, however, additional simplifications were made, to make discretization and meshing easier, and to reduce calculation times. The semi-circular crown is represented by six straight-edge segments of uniform length (Fig. 7.2). The tunnel axis, which trends 054°, is aligned with the model y-axis. The positive model y-direction corresponds to 054° (northeast) in reality. The positive model x-direction corresponds to 144° (southeast). The dip directions of the three joint sets in the model are rotated accordingly. The centre line of the tunnel floor is positioned at the origin in the model x-z-plane.

Around the tunnel there are material boundaries used to vary the mesh density and material properties. The boundaries are concentric with the excavation boundary, and are positioned at distances of 0.1, 0.2, 0.4, 0.6, and 1.0 m. Thus, it is possible to include stepwise changes in material properties with high resolution close to the excavation boundary.

At an early stage, an attempt was made to represent the CDZ by increased joint density; either as a discrete fracture network (DFN) or as deterministic joints. However, it was not possible to attain the necessary level of detail in the jointing, while still being able to mesh the model with a grid configured for fluid flow. It was therefore decided to represent the CDZ by altering the stiffness properties of the blocks and the hydraulic properties of the natural joints.

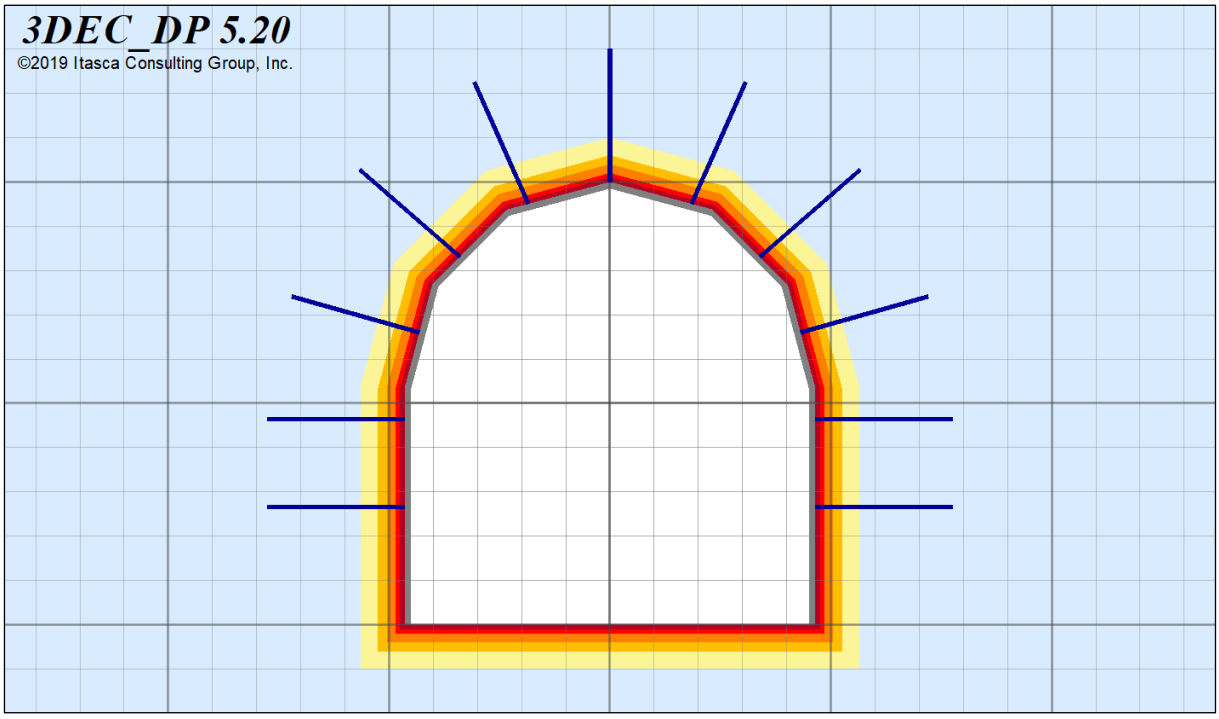

Figure 7.2: Tunnel geometry and rock support in the DE model. Material boundaries are positioned 0.1, 0.2, 0.4, 0.6, and 1.0 m from the excavation boundary, and coloured in shades of red to yellow. The lining (grey) is represented by beam elements, while the bolts (dark blue) are represented by cable elements. The interval of the grid is 1 m.

7.2.4 Rock Support

The rock support in the DE model is analogous to the support in the FE model. It includes lining and rock bolts.

The rock bolts are represented by cable elements. Cable elements include not only the strength of the steel rebar, but also shear resistance of the bond between grout and either the bolt or the rock mass. As in the FE model, the bolt length is 3 m and the spacing between bolts is 2 m in both the tunnel axial direction and the cross-sectional direction.

The sprayed concrete lining is represented by beam elements in the tunnel walls and crown. These are elements lying between two nodal points, and consist of straight segments with uniform cross-sectional properties (Itasca Consulting Group Inc., 2016b). The distance between beam nodes is 0.2 m in both the tunnel axial direction and the cross-sectional direction. Beam elements are chosen to avoid having to model the lining using deformable blocks. If deformable blocks were used, the zone size would have had to be very small in order to model the lining behaviour correctly. Therefore, the lining is represented by beams, with material properties representing an equivalent continuous lining. The waterproof character of the lining is represented by a zero discharge boundary condition.

7.3 Material Properties

7.3.1 Block Properties

The material properties of the undisturbed rock are based on the results of the laboratory investigations (Section 5.2). No plastic block deformations are expected, considering the high uniaxial compressive strength (123 MPa) compared to the virgin stresses and the induced stresses obtained from the FE simulations. Therefore, an isotropic linear elastic material model is chosen for the block material, although, based on observations in the field and results from the laboratory investigations, isotropic behaviour is probably not perfectly accurate. The material properties are shown in Table 7.2. The blocks of intact rock are assumed to be impermeable (i.e., there is no matrix fluid flow).

7.3.1.1 Block properties in the CDZ

The stiffness of the blocks in the CDZ is reduced, in order to represent the effect of blast damage. This is done for all scenarios, including those where the hydraulic apertures in the CDZ are not manually changed (i.e., scenarios 1.1 and 2.1). The exception is, of course, the reference scenario, which does not contain any mechanical calculations.

The stiffness of the disturbed rock is estimated using the disturbance factor and the generalised Hoek-Diederichs equation (Eq. (2.15)). Disturbed properties are assigned to the regions extending 0.0–0.1, 0.1–0.2, and 0.2–0.4 m from the excavation boundary. These three regions are assigned disturbance factors of 0.9, 0.7 and 0.4 respectively, corresponding to the disturbance factor in the middle of each region when it decreases linearly from one at the excavation boundary to zero at a distance of 0.5 m. Beyond 0.4 m undisturbed properties are used. The GSI is set to 70, as observed during the field investigations. With these parameters, the generalised Hoek-Diederichs equation gives the values shown in Table 7.3 and Fig. 7.3. The density and the Poisson ratio are not changed from the undisturbed values.

Table 7.2: Material properties for the blocks of intact rock in the DE model. The values are obtained from the laboratory investigations.

Property	Value
Density, kg m^{-3}	2730
Young's modulus, GPa	47
Poisson ratio	0.33

Table 7.3: Young's modulus for the damaged rock in the DE model. The values are calculated using the generalised Hoek-Diederichs equation. For comparison, values calculated by the method proposed by Barton (2002) are also shown.

Condition	Young's modulus
	GPa
Generalised Hoek-Diederichs equation	
$D = 0.9$	12
$D = 0.7$	16
$D = 0.4$	23
Method proposed by Barton (2002)	
$Q = 1.2$	11
$Q = 9$	22
$Q = 13.3$	25

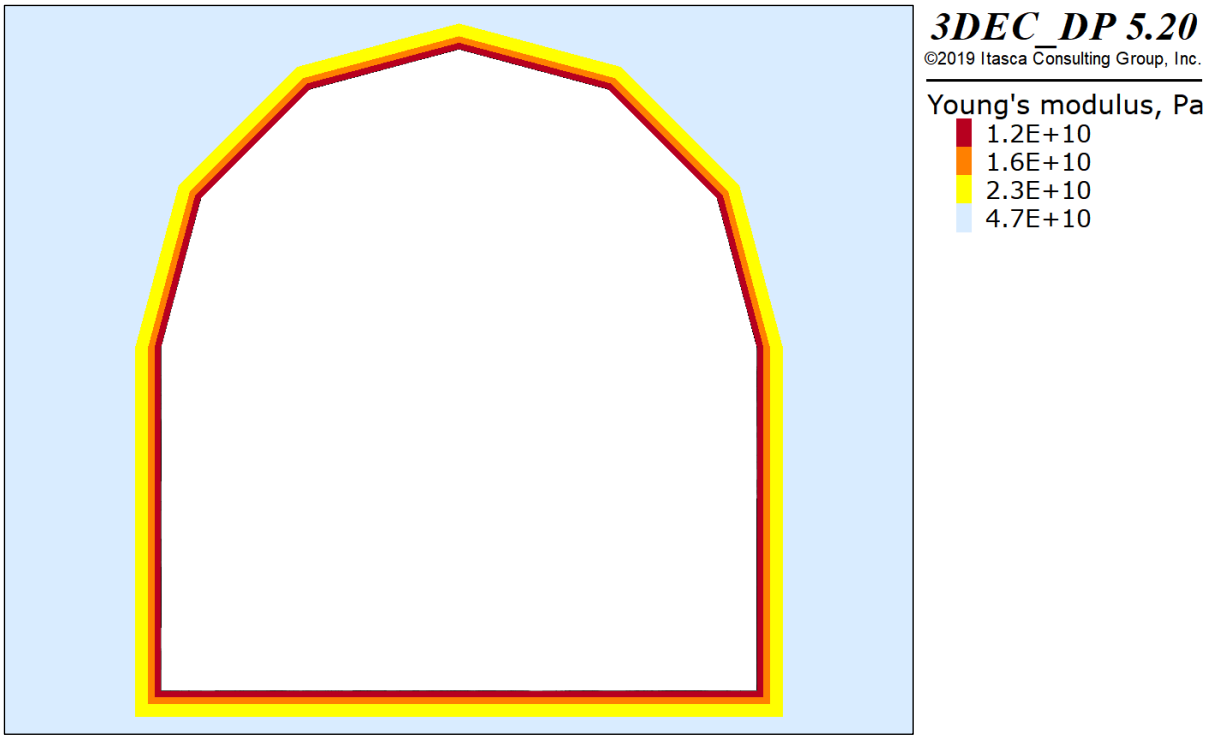

Figure 7.3: Young's modulus of the damaged rock after excavation of the tunnel. The Young's modulus is calculated with the generalised Hoek-Diederichs equation with increasing disturbance factor when moving closer to the excavation boundary.

For comparison, the Young's modulus of the disturbed rock is also calculated using a method proposed by Barton (2002, Eq. (9)). The Q-values determined in the field should be approximately representative for the CDZ (after all they are determined based on observations of blasted surfaces). Therefore, using the method proposed by Barton with the Q-values determined in the tunnel, should give similar results as the generalised Hoek-Diederichs equation (forgetting, for the moment, that the GSI used in this equation is also based on observation of blasted surfaces). Table 7.3 shows that there is indeed good agreement. The values obtained with the generalised Hoek-Diederichs equation all fall within the range spanned by the values calculated with the equation proposed by Barton.

The blocks in the CDZ are, as the rest of the blocks, modelled as isotropic linear elastic. This is appropriate as plastic deformations are expected to be negligible compared to elastic deformations. For example, when the parameters GSI = 70, m_i = 19 (typical Hoek-Brown constant for intact metasandstone), and D = 1 are chosen, a rock mass uniaxial strength of 10 MPa and a rock mass global strength of 25 MPa are obtained with the generalised Hoek-Brown criterion. Comparing this to the stresses obtained from the FE simulations, one realises that elastic behaviour will be dominant.

A comment is made on the nature of the stiffness parameters. While the blocks of undisturbed rock are assigned the stiffness properties found for intact rock in the laboratory, the blocks in the CDZ are assigned rock mass values. This is because, whereas the joints included in the model are assumed to adequately represent the significant discontinuities in the undisturbed rock mass, the fractures induced in the CDZ have not been included explicitly.

7.3.2 Joint Properties

The joint properties in the DE model are based on the findings in Section 5.3. For stress field scenario 1, the stiffness values are stated in Table 5.8. The normal stiffness is initially set to that for interlocked joints. After each calculation stage, the joints that have experienced slip or separation are assigned the appropriate value for mismatched joints.

In order to obtain useable strength parameters, the JRC and the JCS of the Barton-Bandis slip model must be converted to equivalent parameters (cohesion and angle of friction) for the Coulomb slip model, as this is the model implemented in *3DEC*. Values for the Coulomb slip criterion are obtained by linearising the Barton-Bandis slip criterion at a representative value of the joint normal stress (Hoek, 2006b). For stress field scenario 1, the linearisation is performed for a joint normal stress of $\sigma = 3$ MPa and a joint pressure of 0.7 MPa, giving an effective stress of 2.3 MPa. This is the effective joint normal stress at tunnel depth before the tunnel is excavated. After excavation, the joint normal stress will decrease on some joints and increase on others, depending on the position and orientation of the joint relative to the tunnel. Therefore, $\sigma' = 2.3$ MPa is considered a representative value. Linearising at this effective normal stress, the two strength criteria become as shown in Fig. 7.4 for joint set J1 and stress field scenario 1. The linearisation is seen to be a good approximation over a reasonably wide range of normal stresses.

For stress field scenario 2 both the stiffness and strength properties are adjusted to the appropriate stress level. This stress level is different for the three joint sets as the stress field is anisotropic. Therefore, the operating point for the linearisation and the normal stress used for calculation of the stiffness parameters will be different for the different joint sets. Otherwise, the procedure for obtaining the values is as before. Table 7.4 shows the joint mechanical properties obtained for both stress field scenarios.

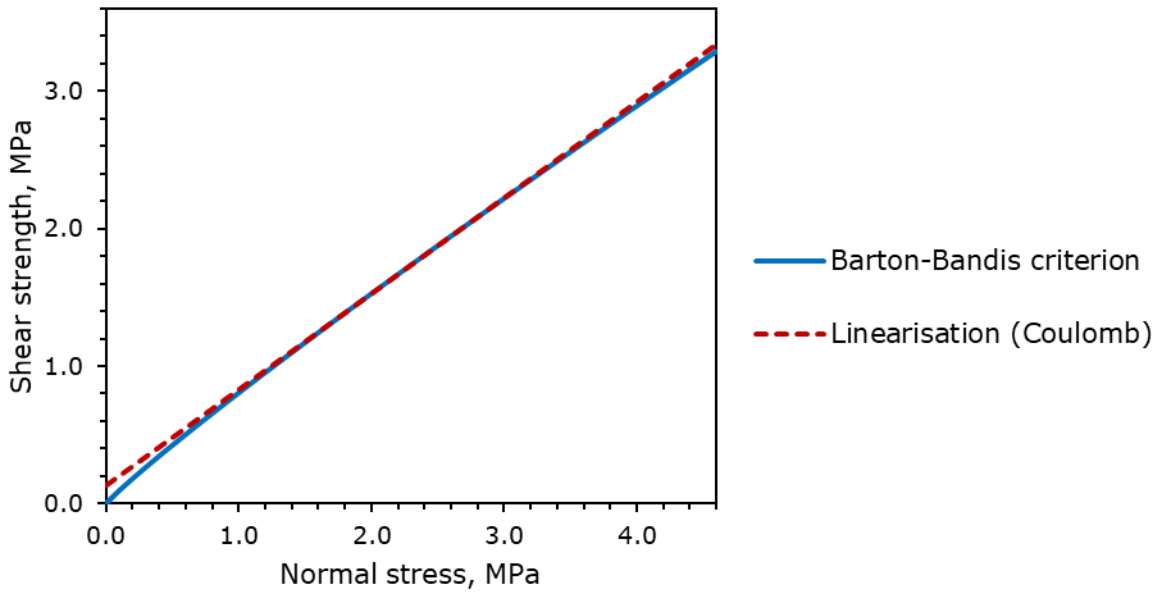

Figure 7.4: Linearisation of the Barton-Bandis slip criterion used to obtain the instantaneous angle of friction and instantaneous cohesion in the Coulomb slip criterion. The chart shows the linearisation for joint set J1 and stress field scenario 1.

Table 7.4: Joint properties in the DE model. The properties of each joint set are shown for both stress field (SF) scenarios, and are calculated based on the field and laboratory investigations as discussed in Sections 5.3 and 7.3.2.

Property	SF scenario 1			SF scenario 2		
	J1	J2	J3	J1	J2	J3
Stiffness						
Interlocked normal stiffness, GPa m^{-1}	93	25	30	54	32	36
Mismatched normal stiffness, GPa m^{-1}	32	10	12	22	13	14
Shear stiffness, GPa m^{-1}	0.32	0.24	0.25	0.18	0.31	0.30
Strength (Coulomb criterion)						
Joint cohesion, MPa	0.14	0.11	0.12	0.08	0.15	0.14
Angle of friction, degrees	35	27	28	36	27	28
Residual angle of friction, degrees	30	24	25	30	24	25

7.3.2.1 Joint hydraulic aperture

The hydraulic aperture of the joints in the undisturbed rock mass can be estimated from the equivalent hydraulic conductivity of the rock mass. This is done using the equation presented by Barton (2003), which gives the effective hydraulic conductivity of a rock mass with three perpendicular joint sets, each with spacing s and hydraulic aperture u_h:

$$K = \frac{\rho g}{\mu} \frac{u_h^3}{6s} \tag{7.1}$$

The effective hydraulic conductivity was earlier estimated to be approximately 1×10^{-8} m/s (Section 6.1.2.3). Rearranging Eq. (7.1) with respect to u_h and inserting ρ = 1000 kg/m^3, μ = 1.52×10^{-3} Pa×s, g = 9.81 m/s^2, K = 1×10^{-8} m/s, and s = 2.3 m (the geometric mean of the spacings for the three joint sets), the hydraulic aperture is calculated to be 28 µm.

7.3.2.2 Joint properties in the CDZ

For scenario 2 for representation of the EDZ (Section 7.1), that is, when construction damage is included in addition to the mechanical effects generated by the model, the hydraulic

apertures of the joints within the CDZ are manually increased. The results of the FE simulations are used as point of departure. In Section 6.1.3, FE modelling was used to find the effective hydraulic conductivity in the CDZ that gave the best fit with the measurements presented by Holter et al. (2015). The results (Table 6.3) are converted to an increase in hydraulic aperture using the cubic law (Section 2.3.2). According to this law, the fracture transmissivity is proportional to the cube of the hydraulic aperture. The effective hydraulic conductivity of the rock mass has the same dependency (Eq. (7.1)). The hydraulic aperture increase in the CDZ implemented in the DE model is, therefore, as shown in Table 7.5.

The hydraulic apertures are modified by simply increasing the minimum permitted hydraulic apertures to the values shown in Table 7.5. Larger but not smaller hydraulic apertures are allowed if such are generated by the model itself. In practice, this creates a scenario where the hydraulic apertures within the CDZ are uniform along the excavation boundary in the walls and crown, but larger for a few joints in the invert (Fig. 7.5).

Table 7.5: Hydraulic apertures in the CDZ in the DE model. The second column shows the effective hydraulic conductivities that were found by FE simulations to give a good fit with measurement data. The third column shows the relative increase in hydraulic conductivity, while in the fourth column this is converted to a relative increase in hydraulic aperture. The final column shows the resulting hydraulic apertures.

Region	Hydraulic conductivity	Relative to undisturbed	Relative aperture increase	Hydraulic aperture
m	m s^{-1}			m
0.0–0.1	8×10^{-7}	80	4	1.1×10^{-4}
0.1–0.2	3×10^{-7}	30	3	8.4×10^{-5}
0.2–0.4	1×10^{-7}	10	2	5.6×10^{-5}
Undisturbed	1×10^{-8}	1	1	2.8×10^{-5}

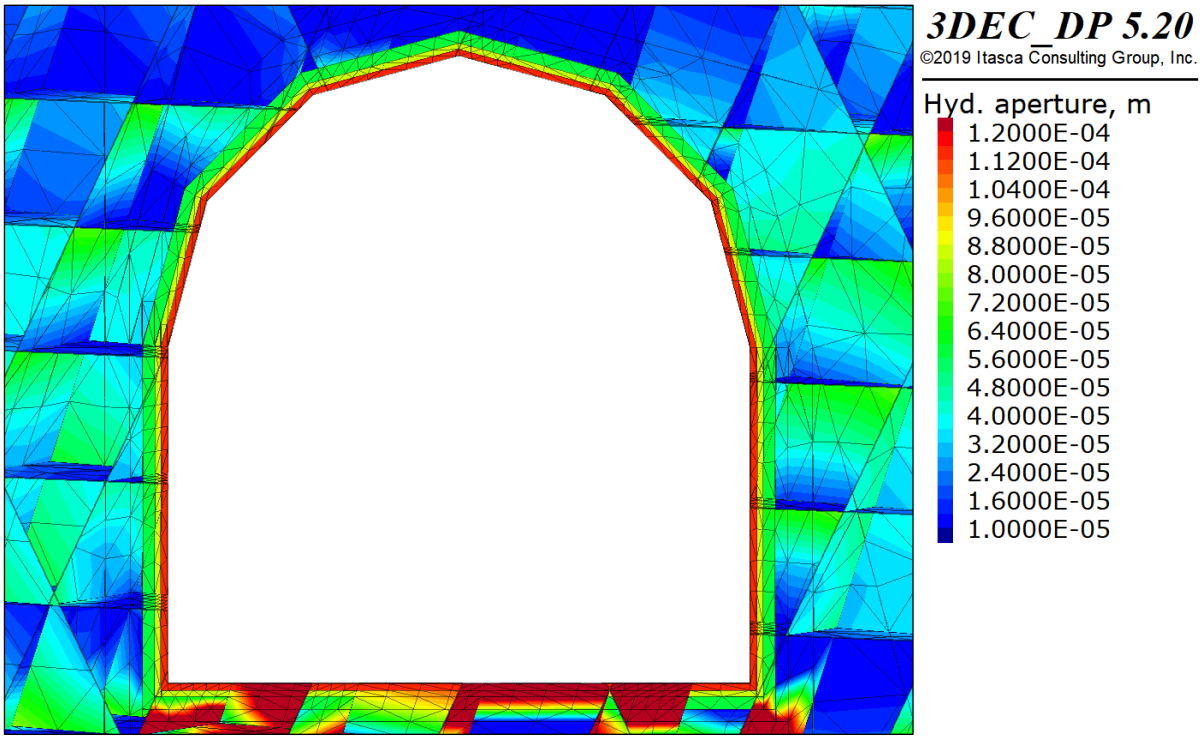

Figure 7.5: Hydraulic apertures in DE model for scenario 1.2 before the final stage. The model is seen in orthographic projection. The minimum hydraulic aperture has been increased within the CDZ, resulting in a situation where the hydraulic apertures are nearly uniform along the excavation boundary, and larger than in the undisturbed rock mass.

7.3.3 Rock Support Properties

The rock support properties are basically the same as those used in the FE model (Table 6.2). The properties of the beam elements representing the SCL are calculated such as to be equivalent to a continuous lining. The bending inertia about the axis perpendicular to both the tunnel axis and the beam axis is set to a high value high to prevent bending about this axis, as this is not realistic for a continuous lining.

7.4 Virgin Stress Field

The properties of the two stress fields included in the DE simulations were previously presented in Section 7.1, and will not be repeated here. The virgin joint pressure is assumed to be hydrostatic from a groundwater table at terrain level (i.e., 60 m above the tunnel crown).

7.5 Mesh Setup

A mesh consisting of tetrahedral zones is used. Tetrahedral zones are computationally efficient compared to mixed-discretization (*quad*) zones, and are preferred when extensive failure of the intact material is not expected (Itasca Consulting Group Inc., 2016c).

The mesh is densest at the excavation boundary and is made gradually coarser further away from the excavation. Thereby, the accuracy is higher near the tunnel. The maximum edge length increases from 0.5 m at the excavation boundary to 3 m in remote parts of the model. One of the considerations made during the choice of maximum edge lengths was to avoid zone aspect ratios (i.e., the ratios between the base length and height of the zone tetrahedra) larger than five.

7.6 Boundary Conditions

Mechanical and flow boundary conditions were specified such as to represent the conditions at relevant depth. The mechanical boundary conditions on the outer model boundaries are as follows (Fig. 7.6a):

- The vertical boundaries and the bottom boundary are normally fixed.
- A vertical stress is applied at the top boundary to obtain the desired stress field.

The flow boundary conditions are chosen such that a situation with no drawdown of the groundwater table is modelled (Fig. 7.6b):

- Constant joint pressure at the horizontal boundaries and at the vertical boundaries that are parallel with the tunnel axis.
- Zero discharge across the vertical boundaries that are perpendicular to the tunnel axis.

After tunnel excavation, a zero joint pressure boundary condition is applied to the tunnel invert, while a zero discharge boundary condition is applied to the walls and crown to obtain a partially drained situation.

7.7 Calculation Stages

The simulations are performed in five main stages:

- Stage 1: Initial stage. Initial mechanical equilibrium is established. The joint pressure field in this stage is calculated from the groundwater level.

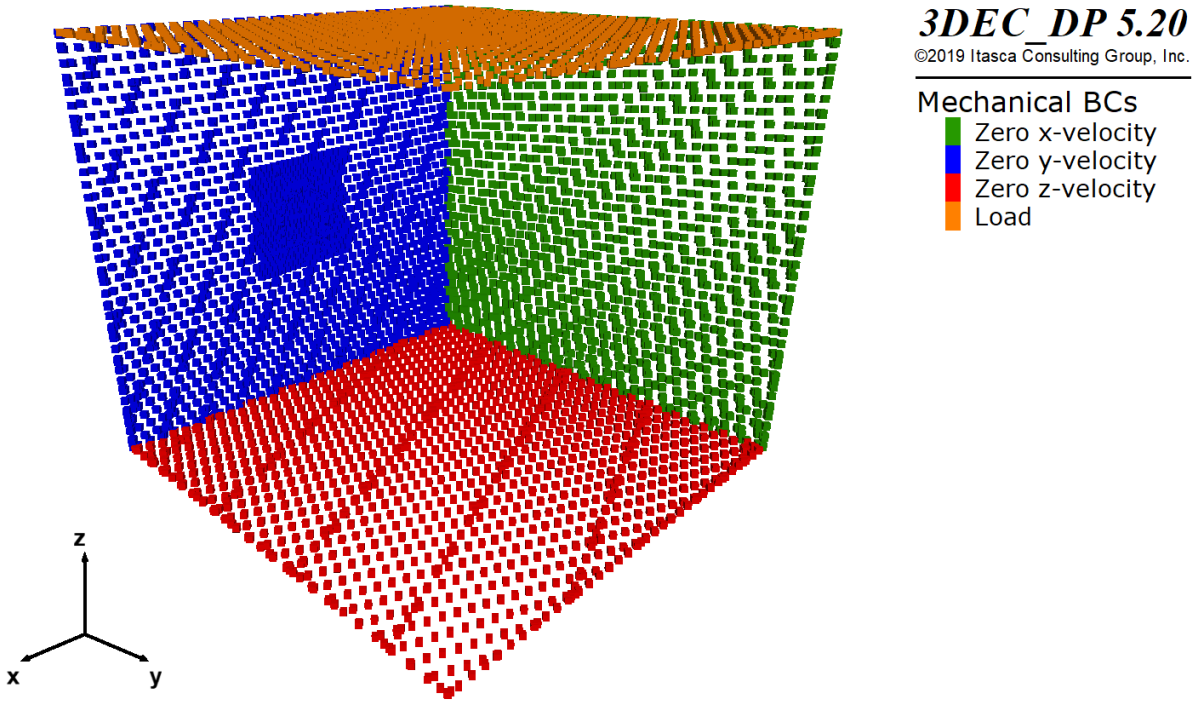

a) Mechanical boundary conditions.

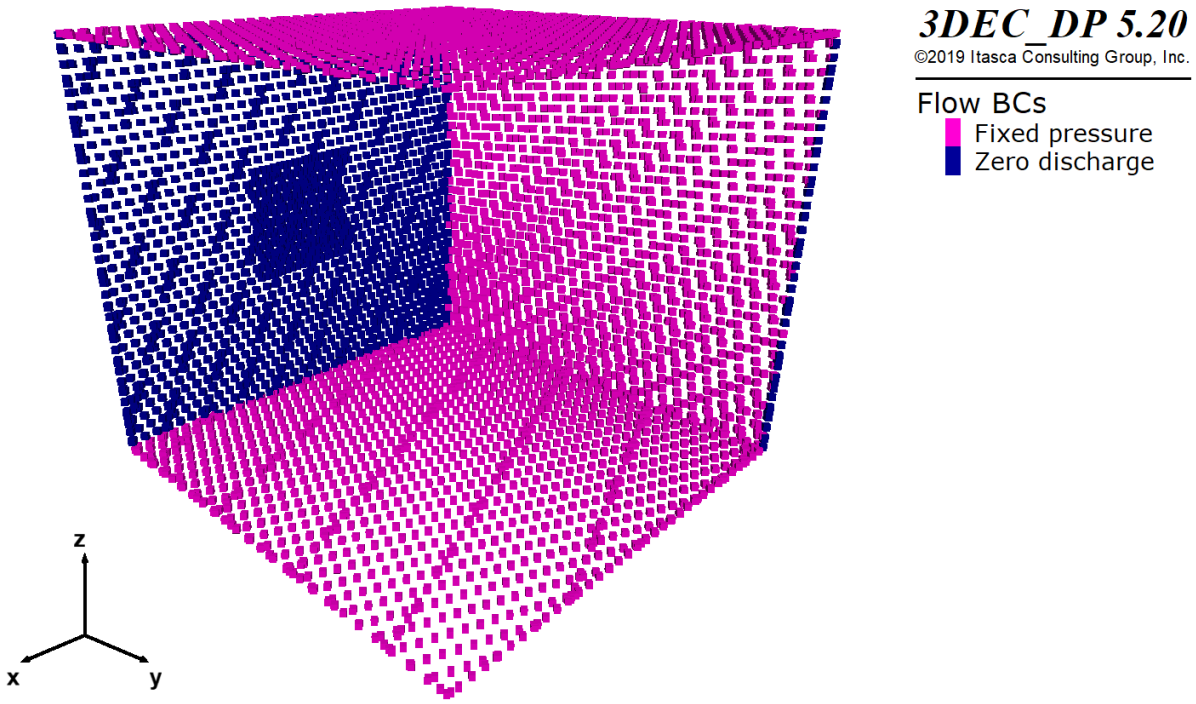

b) Fluid-flow boundary conditions.

Figure 7.6: Boundary conditions in the DE model. The figure shows: a) mechanical boundary conditions (BCs) and b) flow boundary conditions. For illustration purposes, the boundaries at x = 40 and y = 40 are not shown.

- Stage 2: Tunnel advancement stage. The blocks comprising the tunnel are removed, and replaced by an internal pressure acting on the excavation boundary to simulate the effect of tunnel advancement. The internal pressure is set to 75 % of the virgin stress (Section 6.1.7.1). The regions representing the CDZ are assigned new stiffness properties, according to their respective degrees of disturbance (Table 7.3). The joint pressure field is unchanged from stage 1.
- Stage 3: Intermediate stage. The internal pressure is reduced to 25 % of the virgin stress. This corresponds to a situation where the excavation face has moved, but still has a small restraining effect on the deformations behind it. This stage was necessary because the internal pressure could not be reduced directly to zero, as this created instabilities in the model. The beam and cable elements representing the rock support are installed at this stage. Stage 3 comprises both a steady state flow calculation and a mechanical calculation.
- Stage 4: Excavation finish. The internal pressure is removed, which means that the rock mass is no longer affected by the excavation face. This stage also comprises both a flow calculation and a mechanical calculation.
- Stage 5: Final stage. No modifications are made to the model. This stage simply comprises another flow calculation to arrive at the final long-term joint pressure field.

7.8 Solid-Fluid Coupling

There is full coupling between joint pressures and deformations, in the sense that they mutually affect each other. However, each calculation stage involves only one flow calculation and one mechanical calculation, performed separately. The flow calculation precedes the mechanical calculation. In other words, the joint pressure field is used as input for the mechanical analysis. During the mechanical calculation, the hydraulic apertures change, thus affecting the joint pressures calculated in the next stage. It was also attempted to use undrained and/or fully coupled logic in *3DEC*, but these attempts were not successful. The fully coupled logic involves rapid changes between flow calculations and mechanical calculations, such that pressures and deformations are effectively calculated together. However, the fully coupled logic in *3DEC* assumes a quasi-static model in the sense that the mechanical model is in equilibrium for the current distribution of joint pressures. This makes this logic unsuitable for intermediate stages of the problem at hand.

7.9 Measures to Reduce the Calculation Time

As already mentioned, the calculation time quickly became very long, particularly for the flow calculations. In order to complete all stages, the calculation time was in the order of weeks, despite that appropriate measures were taken to reduce it as much as possible.

One important measure is control of the maximum and minimum permissible hydraulic apertures. By capping the maximum and minimum hydraulic apertures that are permitted in the model, the contrasts in fracture transmissivity are reduced, thus increasing the critical time step. The minimum aperture was set to 10 μm. Any reduction beyond this is considered unlikely in reality, as the joint normal stiffness increases with the closure. Therefore, unlimited closure is not realistic. The maximum hydraulic aperture was set to five times the initial hydraulic aperture. A maximum five-fold increase makes sense based on the results of the FE simulations and capping the hydraulic aperture at this value will probably have little effect on the final state, because:

1) Only a few joints, all in the invert, are affected by the cap.
2) A five-fold increase in aperture corresponds to an increase of the fracture transmissivity by two orders of magnitude. Any further contrast in fracture transmissivity will probably have relatively little effect.

Additional measures taken to reduce the calculation time include control of the minimum permissible flow plane area, control of the minimum fluid knot volume, and control of the minimum flow zone edge length.

8 Distinct Element Simulation Results

The DE simulations produce a wide range of output. Recalling that the thesis set out to simulate joint pressures, this is what most of the presented results will centre around. Additional comments are made regarding the stress field and hydraulic apertures.

The results will be presented in three different views. For each scenario, the pressure at the excavation boundary, including variations in the tunnel axial direction, is illustrated by a perspective projection with a line of sight that coincides with the tunnel axis. In perspective projection, points in 3D space are projected to a projection plane using vanishing points, such that faraway objects appear smaller than close objects. This gives the impression of seeing the model in 3D. To illustrate the pressure field away from the excavation boundary, a figure under orthographic projection and a cross-section are presented. In orthographic projection, points in 3D space are projected to a projection plane by lines that are orthogonal to this plane. With a line of sight that coincides with the tunnel axis, this gives the impression of looking at a 2D section of the model. The orthographic projection shows a pressure field that appears to be continuous in space, produced by looking at a subdomain of the model that includes everything on one side of a vertical plane normal to the tunnel axis. Finally, the cross-section shows a contour plot of the pressure in joints that are cut by the same plane. The cross-section is included mostly for illustration purposes, to highlight the discontinuous nature of the model. The values in the tunnel crown, and in joints 10 m to the side of the tunnel will be pointed out, and later compared to the measurement results reviewed in Section 4.3.

8.1 Reference Scenario: No Excavation Damage

For the reference scenario (Table 7.1) with absolutely no change in hydraulic apertures due to the tunnel excavation, the joint pressure in the tunnel crown is generally in the range 440–470 kPa (Fig. 8.1). Compared to the hydrostatic pressure, this corresponds to a reduction of slightly more than 100 kPa at the centre of the crown. As could be expected based on the uniform hydraulic apertures, there are virtually no pressure variations in the direction of the tunnel axis. Due to the geometry of the joint network, the pressure is marginally higher in the right wall than in the left. Ten metres to the side of the tunnel at mid-height, the joint pressure is 475–500 kPa, that is, only slightly higher than at the excavation boundary (Figs. 8.2 and 8.3).

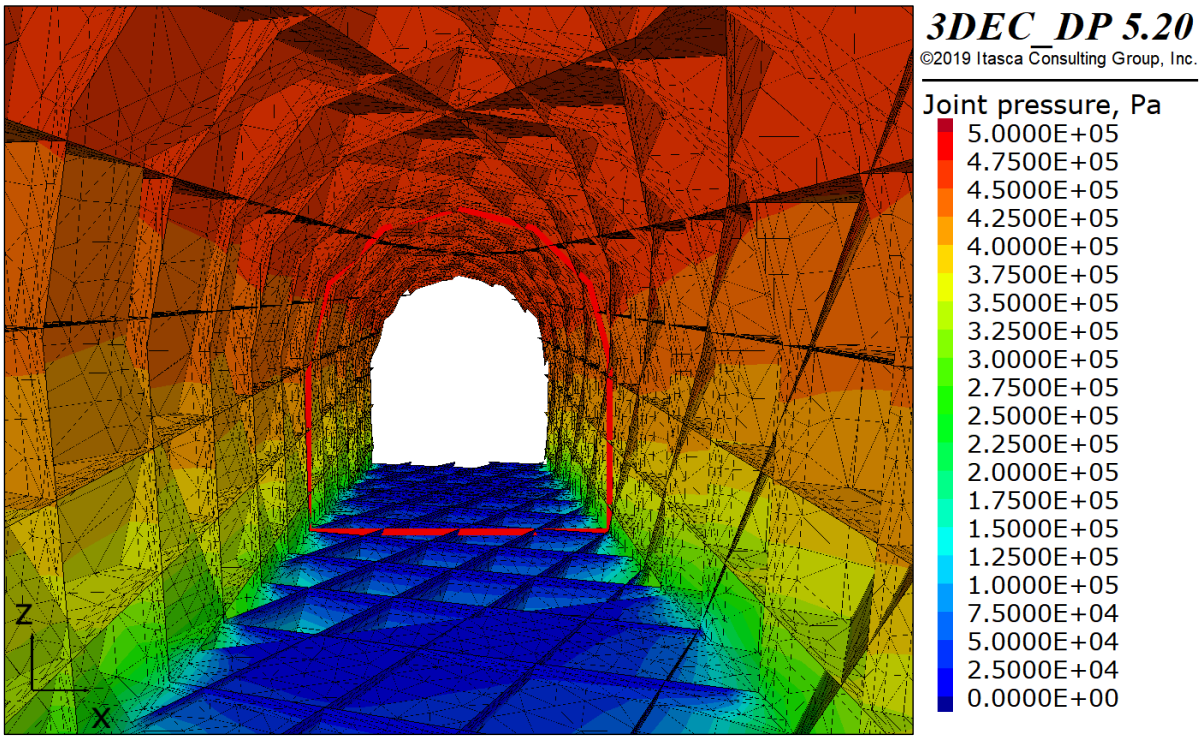

Figure 8.1: Perspective view of the joint pressure at the excavation boundary for the reference scenario without any excavation damage. The maximum pressure is approximately 470 kPa. There are only minor variations in the direction of the tunnel axis. The location of the plane where the model is cut in Figs. 8.2 and 8.3 is indicated by a red line along the tunnel circumference. Only the middle 40 m of the model are shown.

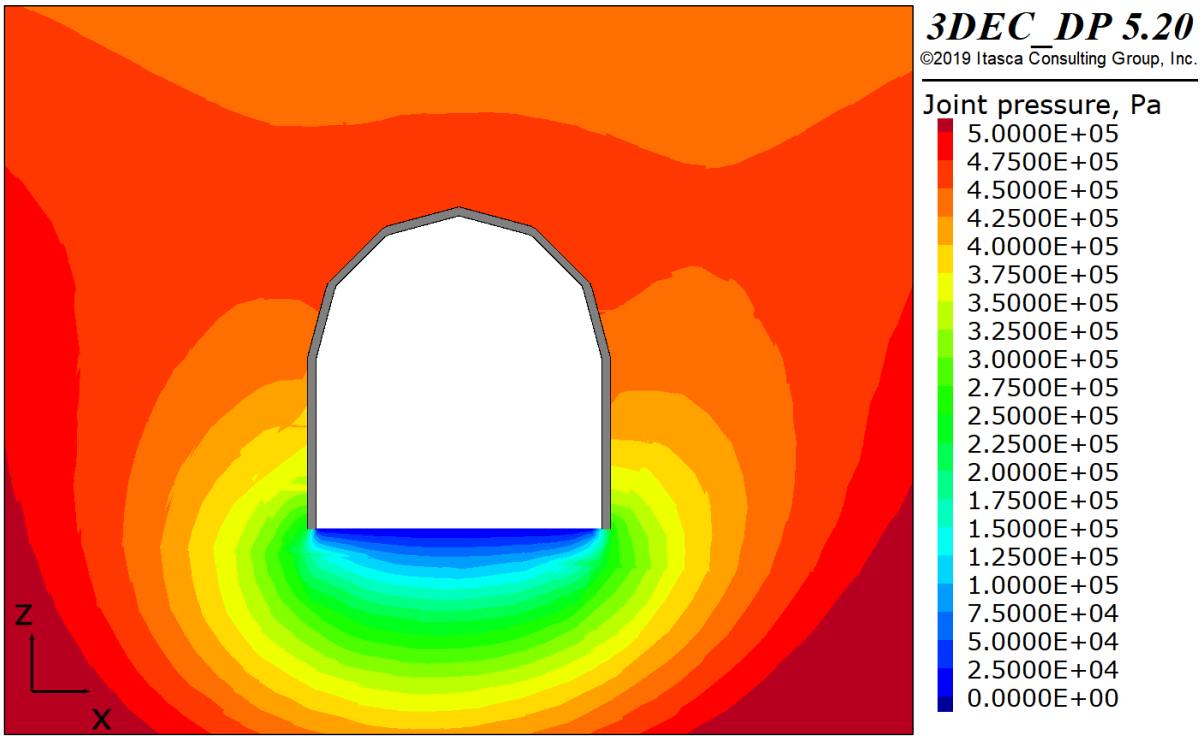

Figure 8.2: Orthographic view of the joint pressure field for the reference scenario without any excavation damage. Ten metres laterally into the rock mass, the joint pressure is in the range 475–500 kPa.

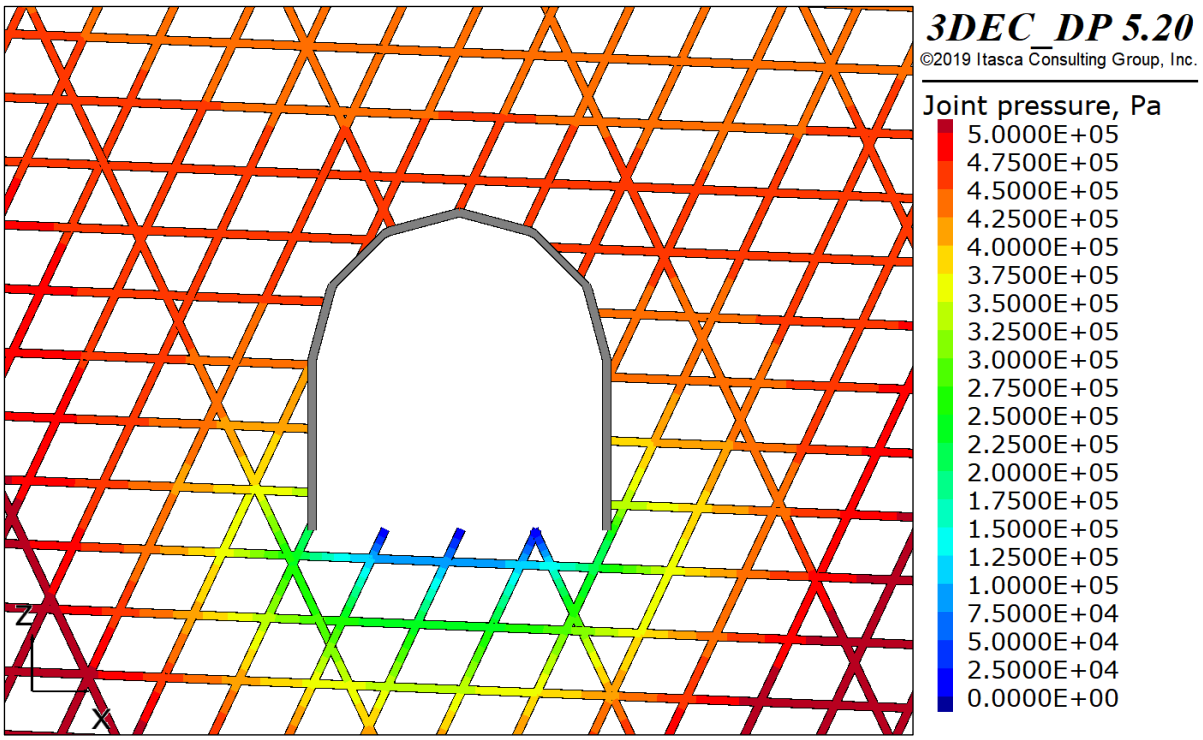

Figure 8.3: Cross-section showing the water pressure in distinct joints for the reference scenario without any excavation damage. The width of the lines is uniform and is not related to the hydraulic apertures of the joints.

8.2 Stress Field Scenario 1: Isotropic Virgin Stress Field

Figure 8.4 shows a contour plot of the major principal total stress for stress field scenario 1 in a representative cross-section. The same location will be used for all orthographic projections and cross-sections shown for scenarios with the isotropic stress field. Due to the effects created when the blocks deform and interact, Fig. 8.4 is not suitable for detailed analysis. The stress can vary widely within single blocks. Also, the low density of the finite difference mesh within each block does not improve the situation. Therefore, only general trends are of interest.

The stress field from the DE simulations for stress field scenario 1 contains several features that were previously observed in the FE modelling. There are stress concentrations in the corners and crown, and a low-stress area in the invert. An effect that was not present in the FE modelling is created due to the reduced stiffness in the region within 0.4 m from the excavation boundary. In this region, the stress is low, while it increases when entering the region with unchanged stiffness. This effect is best observed at the left side of the crown. The stress redistribution and deformations result in an increase in the hydraulic apertures in the tunnel walls, and a decrease in the crown and corners (Fig. 8.5).

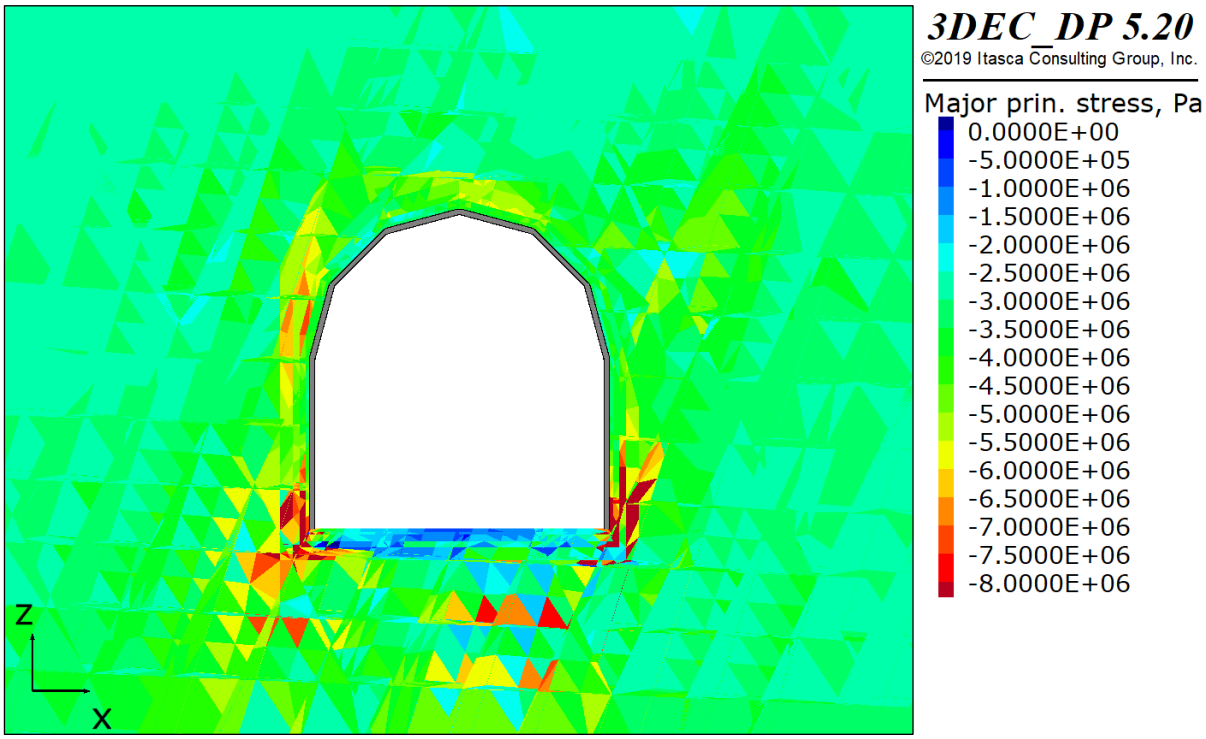

Figure 8.4: Cross-section showing a contour plot of the major principal total stress for stress field scenario 1. There are stress concentrations in the corners and crown, and stress relief in the invert. The region with reduced stiffness due to construction damage is de-stressed. Compression is negative.

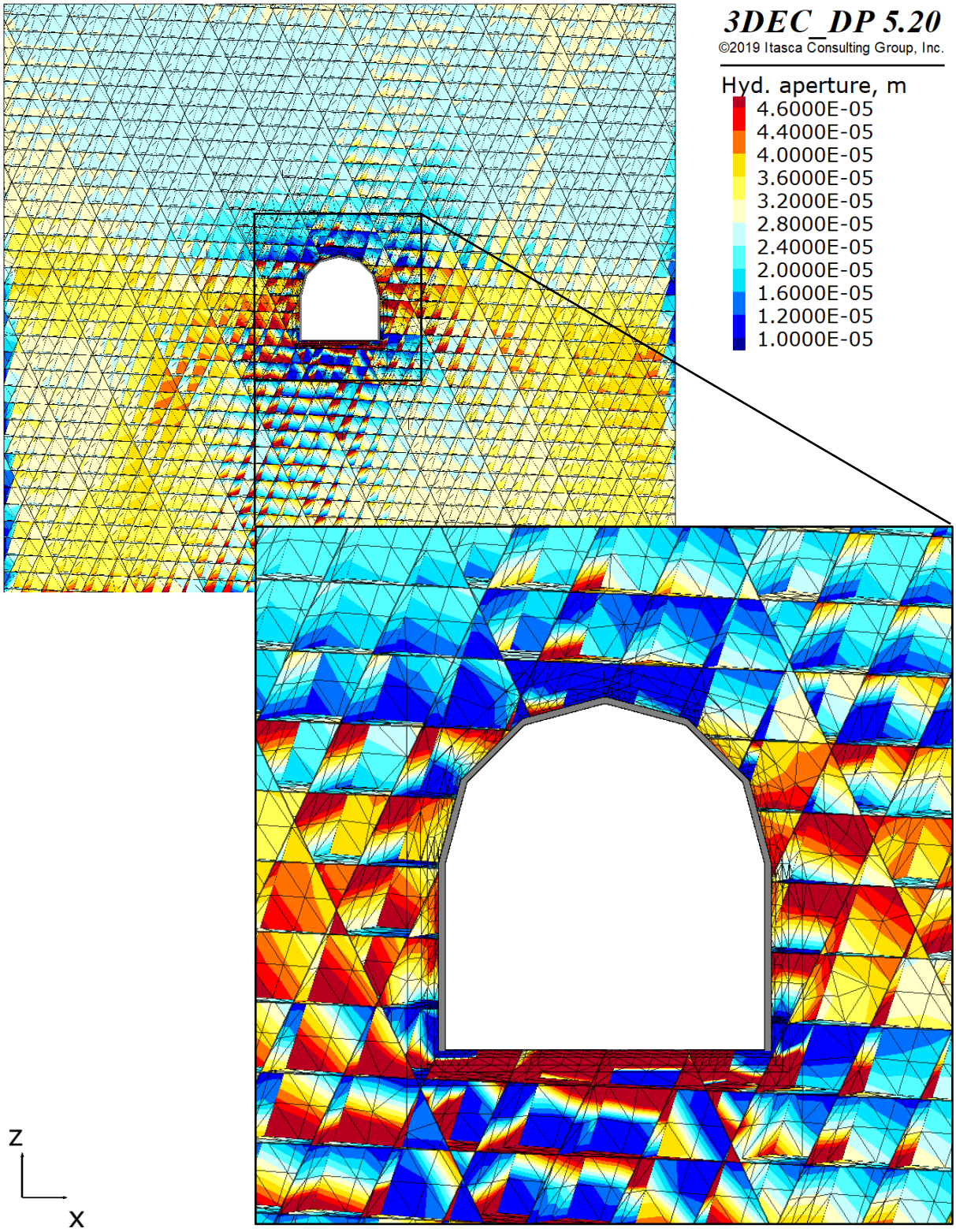

Figure 8.5: Joint hydraulic apertures produced by the DE simulation for scenario 1.1. Warm colours indicate an increase in aperture compared to the virgin state, while cold colours indicate a decrease. Generally there is an increase in the apertures in the walls and invert, and a decrease in the crown and corners. To make the contour ramp symmetrical about the original aperture, all values exceeding 46 µm are coloured cardinal red. The figure makes no distinction between apertures exceeding this value.

8.2.1 Scenario 1.1: No CDZ with Increased Hydraulic Apertures

When changes in the hydraulic apertures generated by the model itself (i.e., damage not caused directly by the excavation works) are included in the simulations, the joint pressures are lower. The pressures reflect the hydraulic apertures shown in Fig. 8.5. The stress concentration and consequent decrease in hydraulic apertures in the corners, result in a high joint pressure gradient in these areas. The joint closure is most pronounced in the right corner, and the flow path to go around the area of reduced apertures is longer than in the left corner. This leads to higher pressures in the right wall than in the left (Fig. 8.6). Generally, the pressure is 300–320 kPa in the left wall and 360–380 kPa in the right wall. In the crown, it increases to approximately 400 kPa a little to the right of the centre.

There are some variations in the direction of the tunnel axis, that is, between the pressures in joints at different y-locations but the same location in the x-z-plane. The presence of local variations is expected because, although there are no variations in any model property along the y-axis, block deformations create variations within distances of one to a few joint spacings. These variations are generally within some tens of kilopascals when the ends of the model are disregarded to avoid including areas where end effects are significant. They are, therefore, not very important compared to the variations within the cross-sectional plane.

The joint pressure reduction compared to the hydrostatic pressure is considerable far into the surrounding rock mass. For example, Figs. 8.7 and 8.8 show a considerable reduction more than 10 m into the rock mass. Ten metres to the side of the tunnel, the joint pressure is in the range 410–430 kPa, which is approximately 200 kPa lower than the hydrostatic pressure.

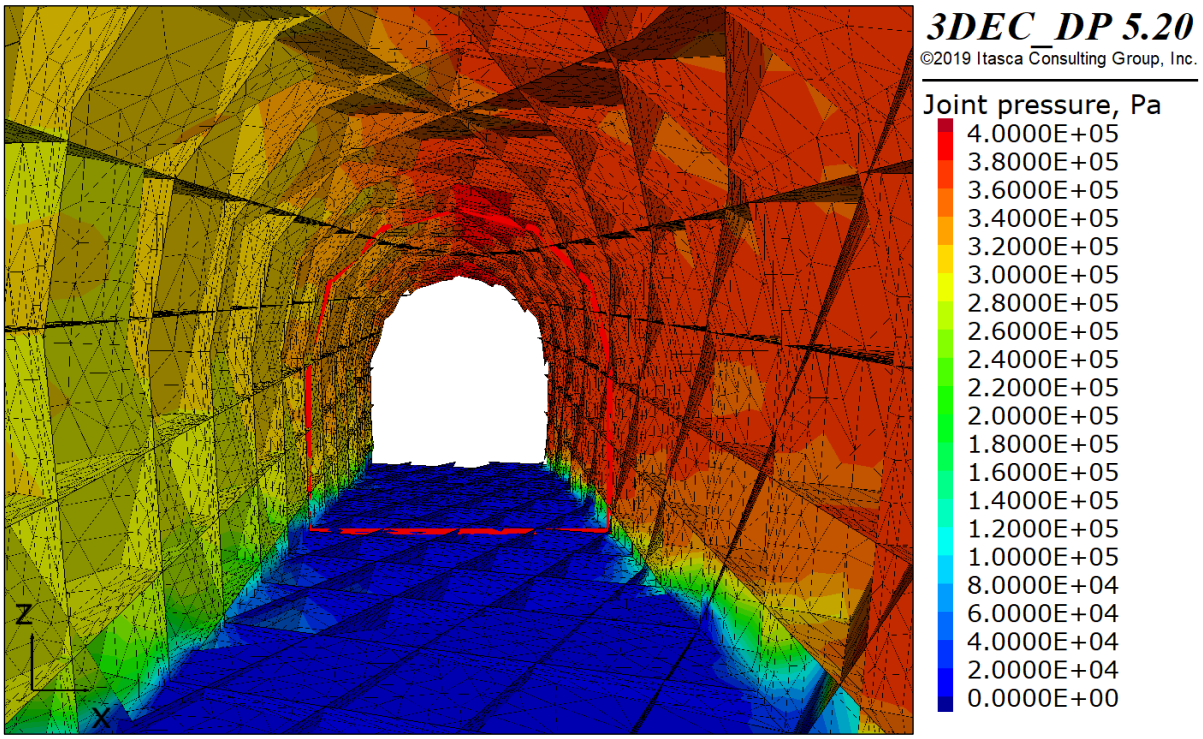

Figure 8.6: Perspective view of the joint pressure at the excavation boundary for scenario 1.1. The maximum pressure is approximately 400 kPa and occurs a little to the right of the centre of the crown. The pressure is higher in the right wall than in the left. Some variations in the direction of the tunnel axis are observed. The location of the plane where the model is cut in Figs. 8.7 and 8.8 is indicated by a red line along the tunnel circumference. Only the middle 40 m of the model are shown.

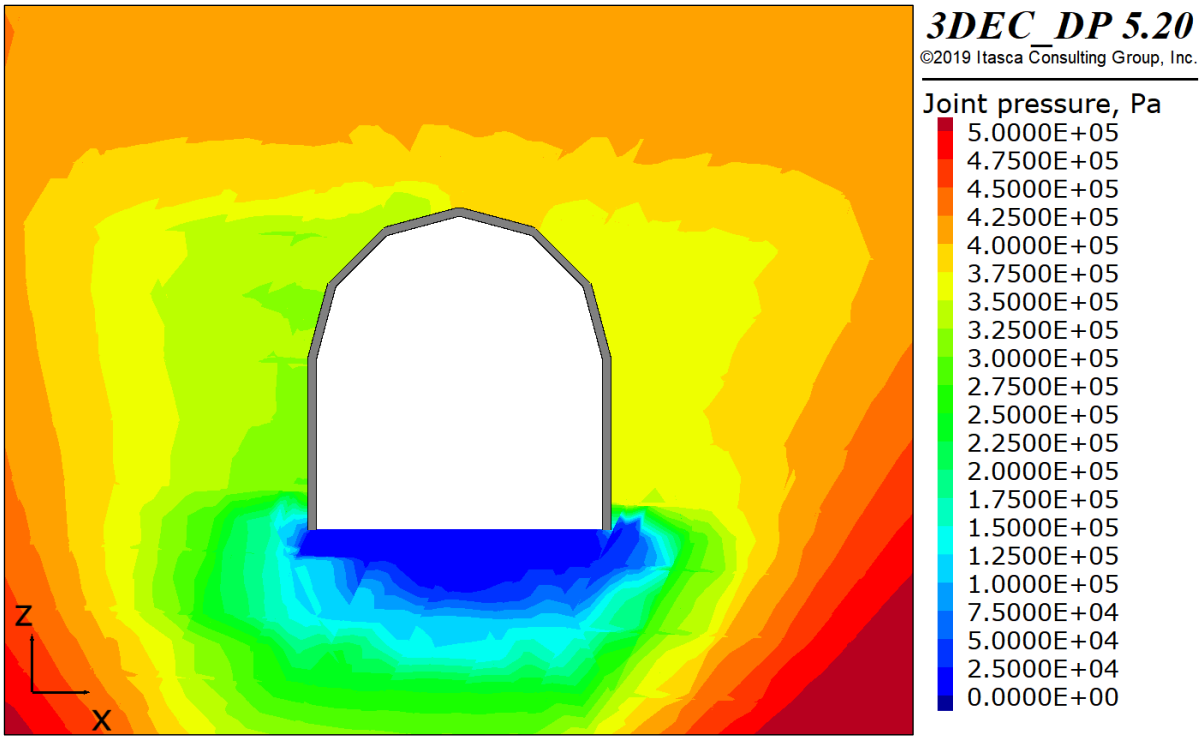

Figure 8.7: Orthographic view of the joint pressure field for scenario 1.1. Ten metres laterally into the rock mass, the joint pressure is 410–430 kPa.

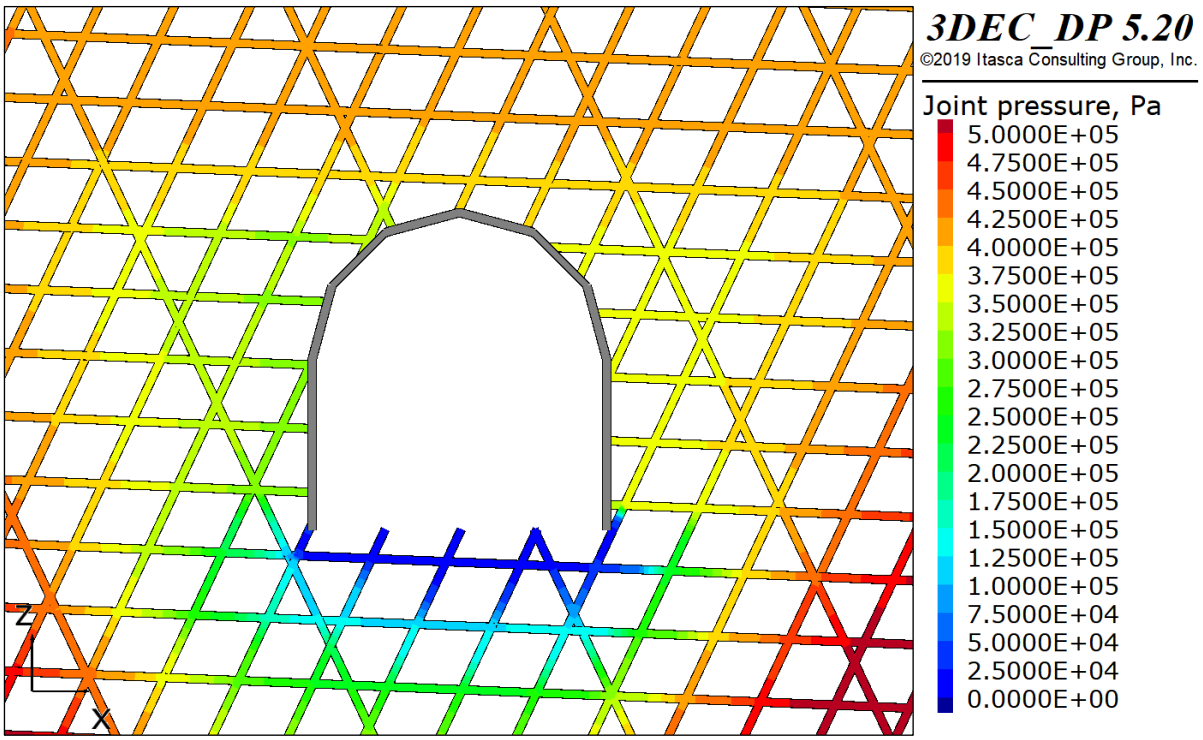

Figure 8.8: Cross-section showing the water pressure in distinct joints for scenario 1.1. The width of the lines is uniform and is not related to the hydraulic apertures of the joints.

8.2.2 Scenario 1.2: Increased Hydraulic Apertures in the CDZ

When a CDZ with increased hydraulic apertures is added, the joint pressure behind the SCL is reduced. In the crown, the joint pressure becomes 125–160 kPa (Fig. 8.9). The pressure is similar in the two walls, and there are only minor variations in the tunnel axial direction. The variations are generally within 10–20 kPa. Therefore, they are unimportant compared to the variations within the cross-section. This is as expected, as the hydraulic apertures within the CDZ are uniform in the y-direction due to the way the CDZ is implemented.

The pressure reduction relative to scenario 1.1 is most pronounced within the CDZ (Figs. 8.10 and 8.11). Outside this zone, the pressure increases rapidly with distance from the excavation boundary. The gradient is higher than for scenario 1.1. However, the pressure reduction relative to this scenario still extends far into the rock mass. For example, 10 m laterally into the rock mass, at tunnel mid-height, the joint pressure is still approximately 100 kPa lower than when the CDZ was not present (compare Figs. 8.7 and 8.10), and only approximately half the hydrostatic pressure. In other words, the pressure gradient approaches the one for scenario 1.1, when moving away from the excavation boundary.

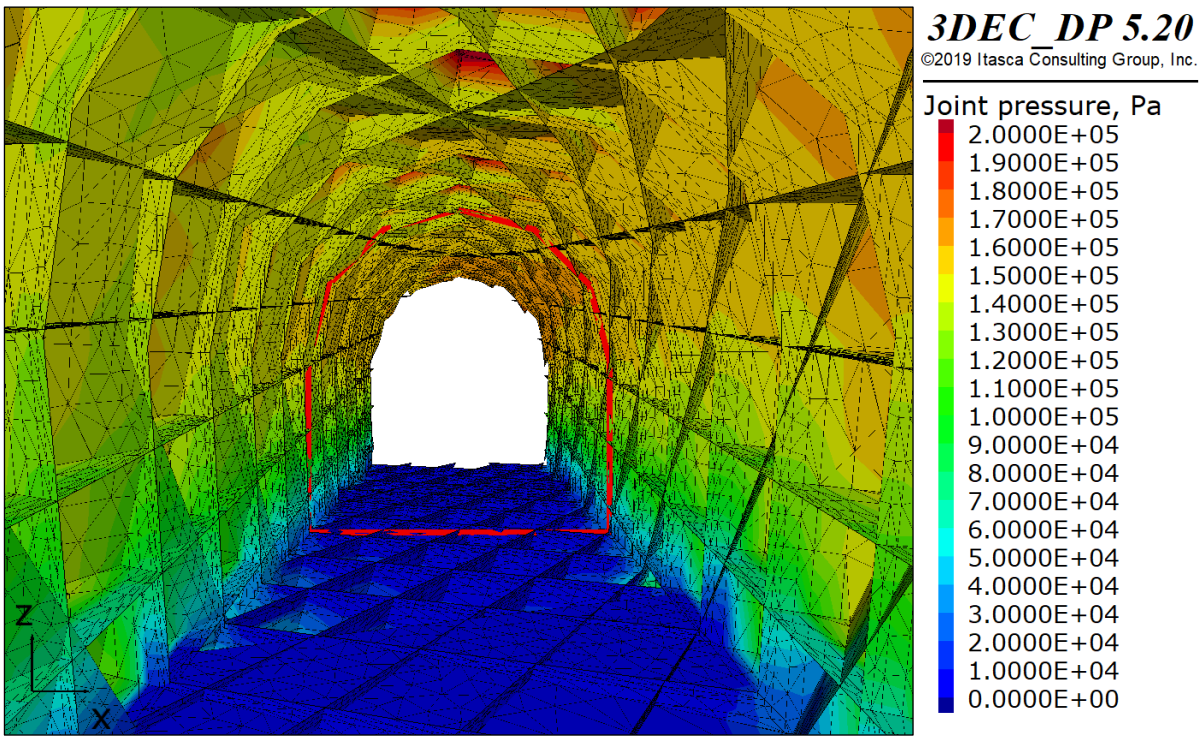

Figure 8.9: Perspective view of the joint pressure at the excavation boundary for scenario 1.2. The maximum pressure is approximately 160 kPa and occurs at the right side of the crown. The CDZ leads to a significant reduction in the joint pressure at the excavation boundary. Minor variations in the direction of the tunnel axis are observed. The location of the plane where the model is cut in Figs. 8.10 and 8.11 is indicated by a red line along the tunnel circumference. Only the middle 40 m of the model are shown.

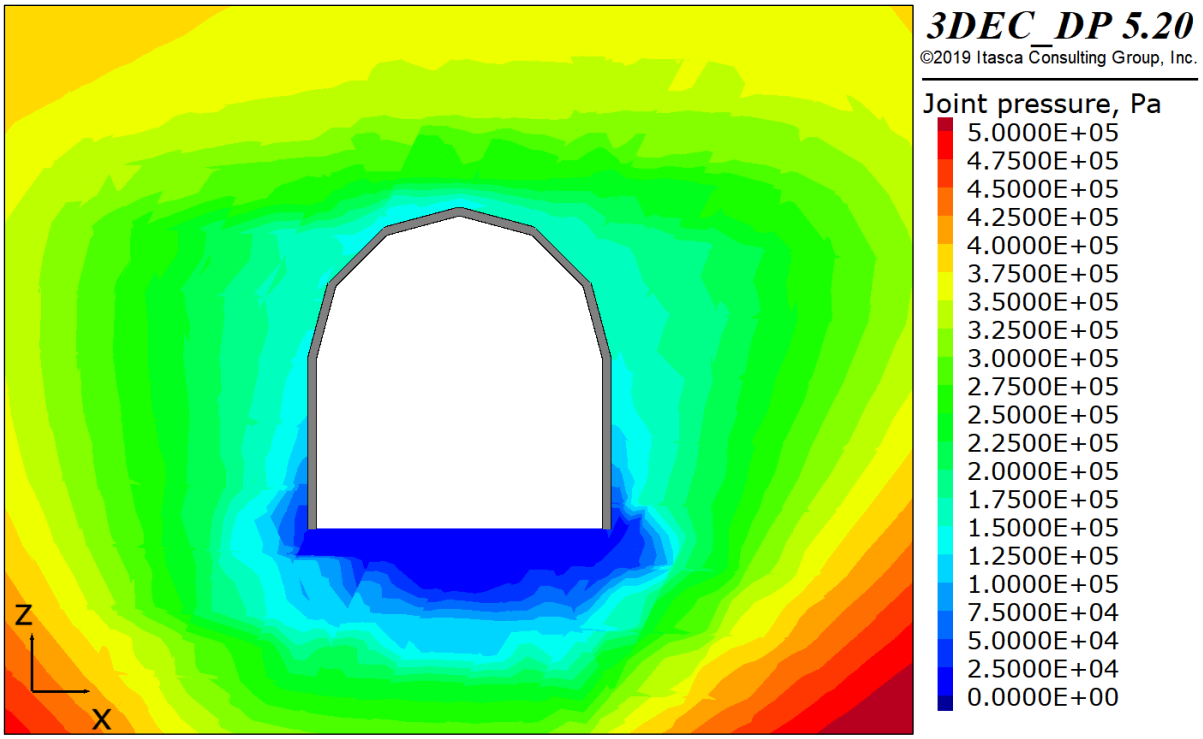

Figure 8.10: Orthographic view of the joint pressure field for scenario 1.2. Ten metres laterally into the rock mass, the joint pressure is approximately 350 kPa.

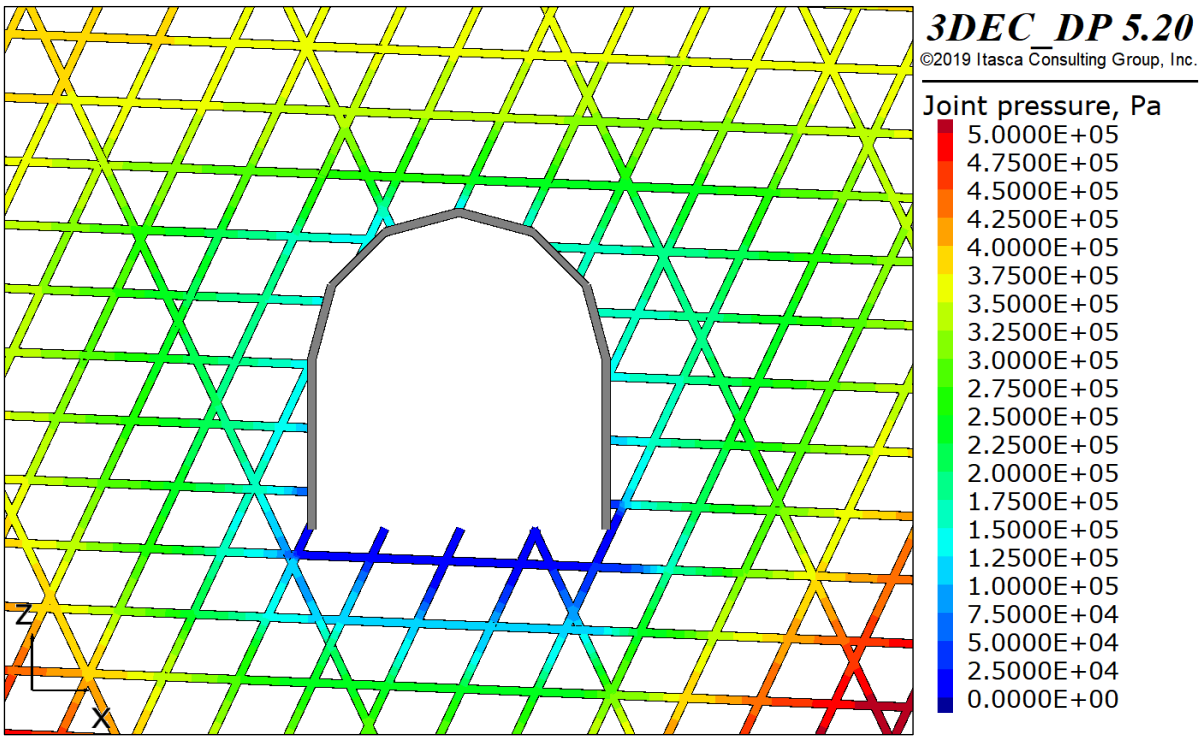

Figure 8.11: Cross-section showing the water pressure in distinct joints for scenario 1.2. The width of the lines is uniform and is not related to the hydraulic apertures of the joints.

8.3 Stress Field Scenario 2: Anisotropic Virgin Stress Field

For stress field scenario 2, the DE simulations did not converge towards a stable state. At some locations, blocks in the tunnel walls were unstable. As the tunnel in reality is stable, this can mean one of two things: either stress field scenario 2 is not representative for the real situation, or joint strength properties in the model are conservative. This adds an extra element of uncertainty to the results for stress field scenario 2 (Sections 9.3 and 9.6.4). To minimise the effect of the instabilities, all cross-sections are located at a point along the tunnel axis where the blocks in the tunnel walls are stable and the joint pressure is considered representative.

Figure 8.12 shows a contour plot of the major principal total stress after tunnel excavation. The stress distribution is generally as could be expected based on the FE modelling, and the DE modelling for stress field scenario 1. As before, there are stress concentrations in the corners. However, there is no distinguished stress relief in the invert, as was observed for the isotropic stress field. Also, the stress concentration in the crown is more localised. The stress above the centre of the crown is higher than before, while the stress at the left springline is lower. Bear in mind, however, that Figs. 8.4 and 8.12 do not show the same cross-section. The highest stresses tend to occur outside the region with reduced stiffness, analogous to what was observed for stress field scenario 1. Finally, there are low-stress areas next to the tunnel walls.

One of the most visible consequences of the anisotropic stress field with regard to hydraulic apertures, is an increase in the walls (Fig. 8.13). The aperture increase is most pronounced in the lowermost areas, and is probably due to convergence, that is, displacement of the rock mass in the direction towards the tunnel. The effect is seen to reach far into the rock mass, and is still present close to the edge of the model.

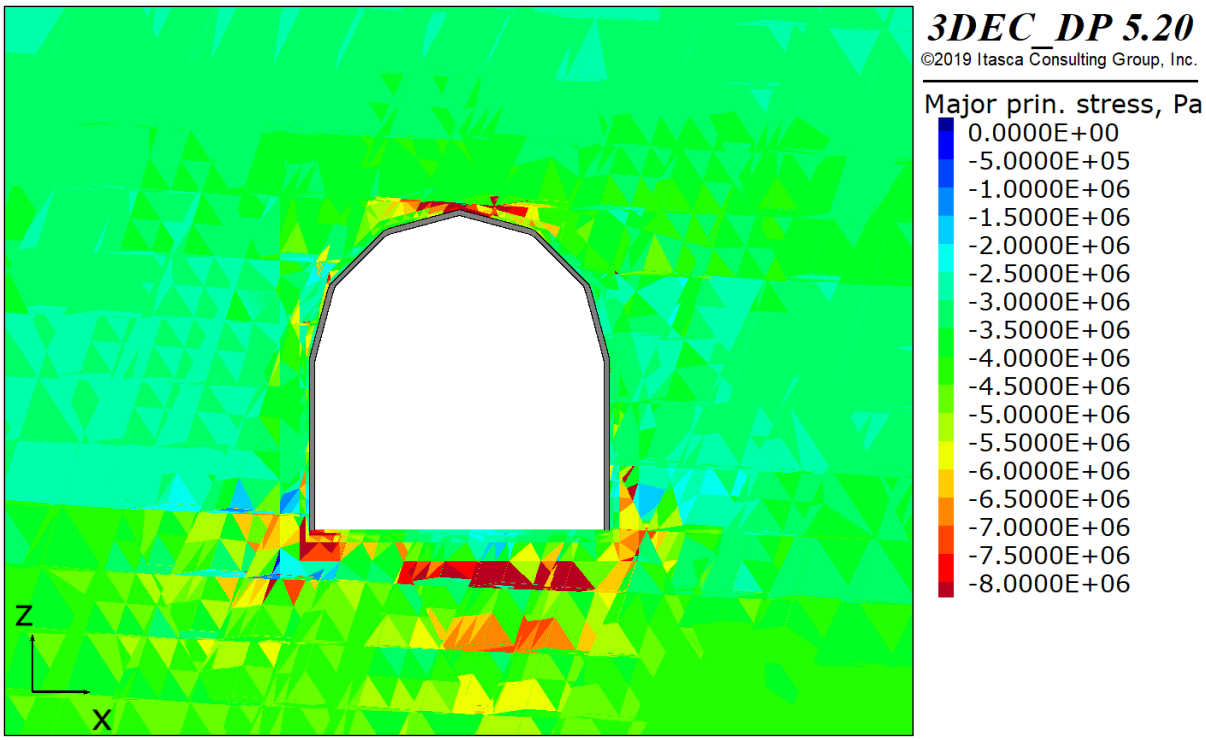

Figure 8.12: Cross-section showing a contour plot of the major principal total stress for stress field scenario 2. There are stress concentrations in the corners and the crown. In the walls there are low-stress areas. Compression is negative.

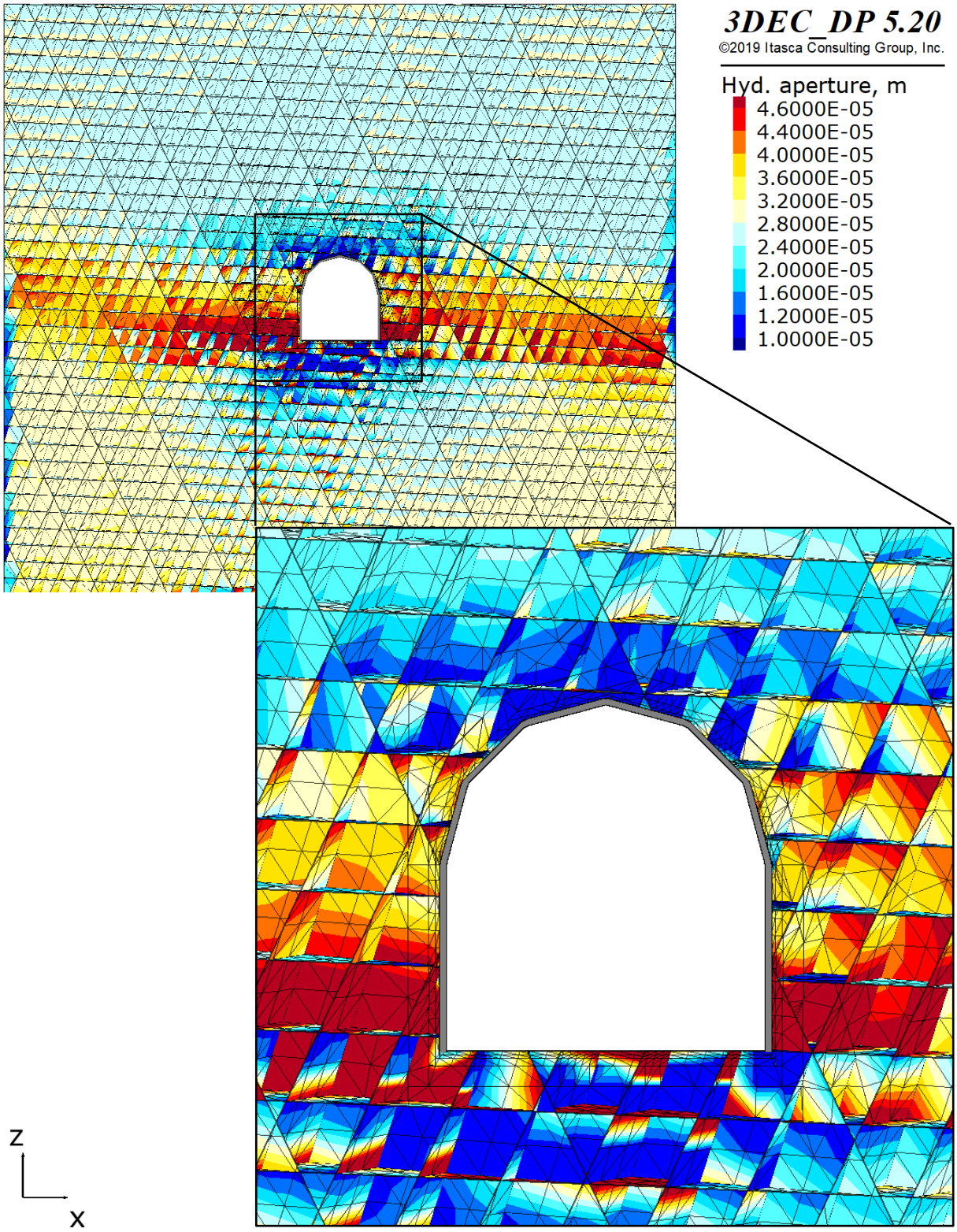

Figure 8.13: Joint hydraulic apertures produced by the DE simulation for scenario 2.1. Warm colours indicate an increase in aperture compared to the virgin state, while cold colours indicate a decrease. There is an increase in the apertures in the walls, particularly in the lower parts, and a decrease in the crown. To make the contour ramp symmetrical about the original aperture, all values exceeding 46 μm are coloured cardinal red. The figure makes no distinction between apertures exceeding this value.

8.3.1 Scenario 2.1: No CDZ with Increased Hydraulic Apertures

For scenario 2.1, which has no CDZ with increased hydraulic apertures, the joint pressure at the excavation boundary is approximately 320 kPa at its maximum (Fig. 8.14). This pressure occurs at the centre of the crown. The pressure at the point of transition between the semi-circular crown and the vertical walls is approximately 200–210 kPa. The pressure is generally slightly lower in the left wall than in the right wall, but the difference is less than for scenario 1.1. Note that the variations in the tunnel axial direction are large in the lower walls. This can probably be attributed partly to the instabilities in this region. At 10 m lateral distance from the tunnel, the joint pressure is 325–350 kPa (Figs. 8.15 and 8.16).

8.3.2 Scenario 2.2: Increased Hydraulic Apertures in the CDZ

For scenario 2.2, where the hydraulic apertures in the CDZ are increased, the results are similar to those for scenario 1.2, which also included a CDZ. However, just as scenario 2.1 resulted in lower pressures than scenario 1.1, scenario 2.2 results in lower pressures than scenario 1.1. The joint pressure in the crown is approximately 110–120 kPa, while the pressure 10 m to the side of the tunnel is approximately 300 kPa (Figs. 8.17, 8.18, and 8.19). Still, the pressure is slightly higher in the left wall than in the right.

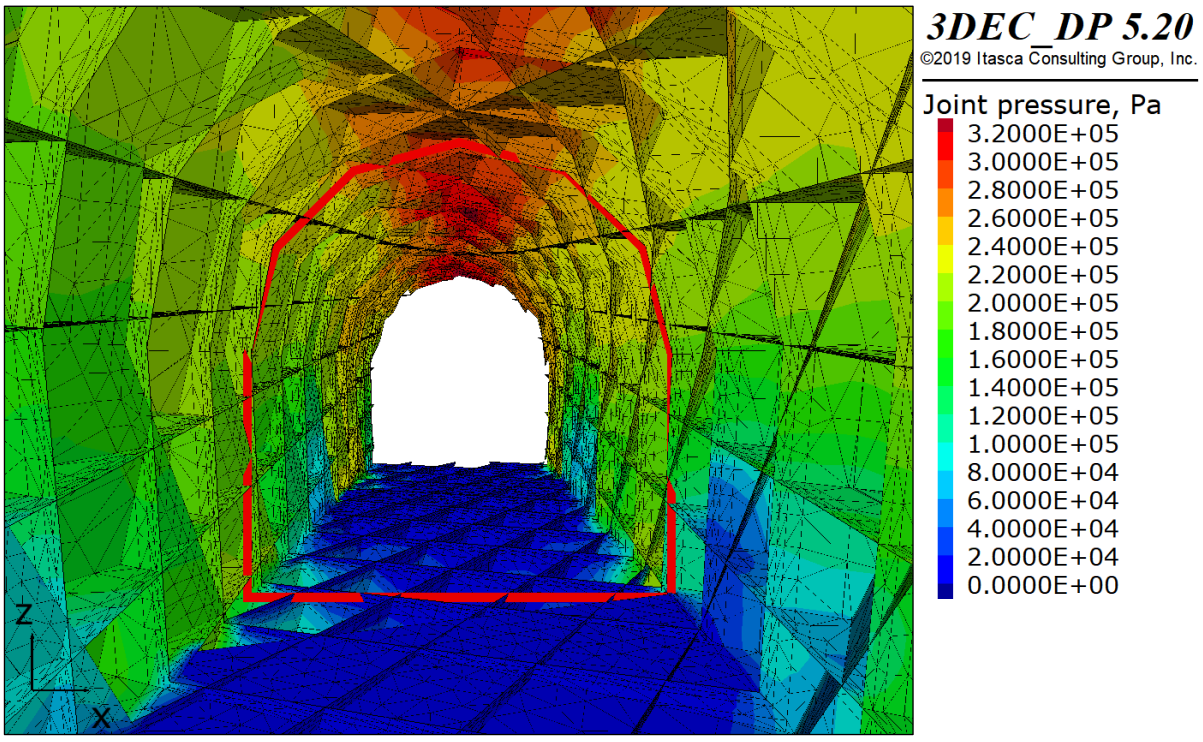

Figure 8.14: Perspective view of the joint pressure at the excavation boundary for scenario 2.1. The maximum pressure is approximately 320 kPa and occurs at the centre of the crown. Small variations in the direction of the tunnel axis are observed. The location of the plane where the model is cut in Figs. 8.15 and 8.16 is indicated by a red line along the tunnel circumference. Only the middle 40 m of the model are shown.

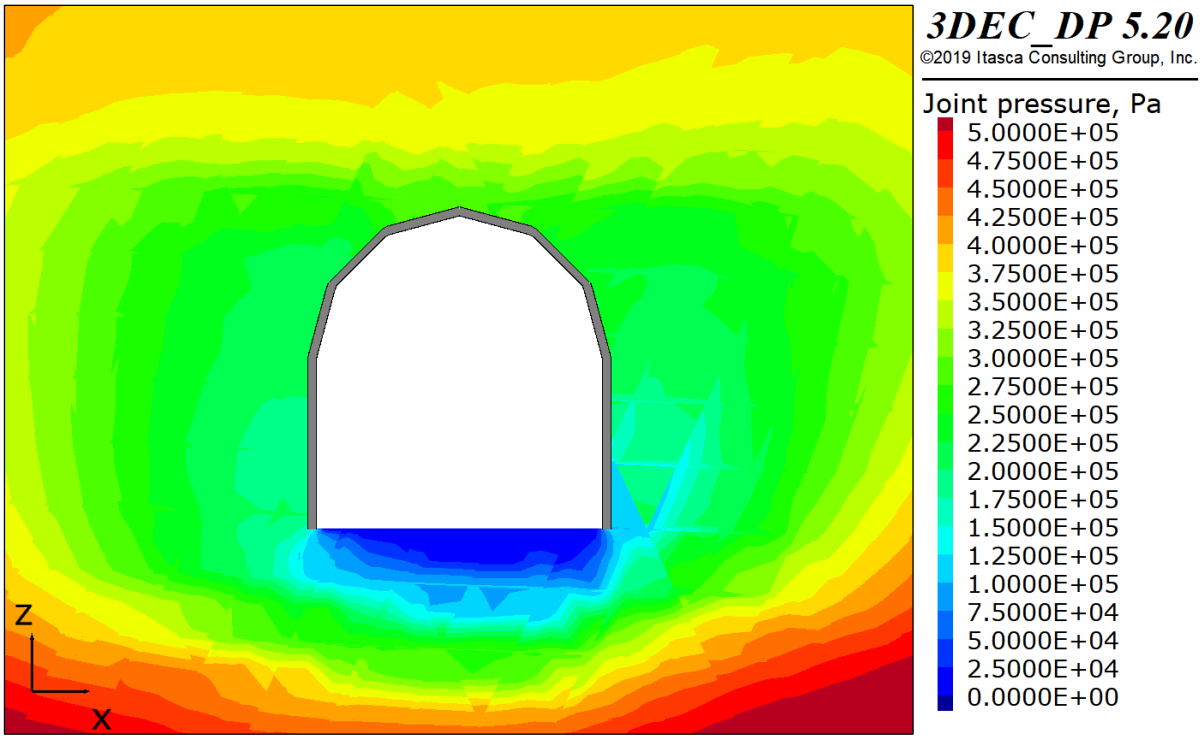

Figure 8.15: Orthographic view of the joint pressure field for scenario 2.1. Ten metres laterally into the rock mass, the joint pressure is 325–350 kPa.

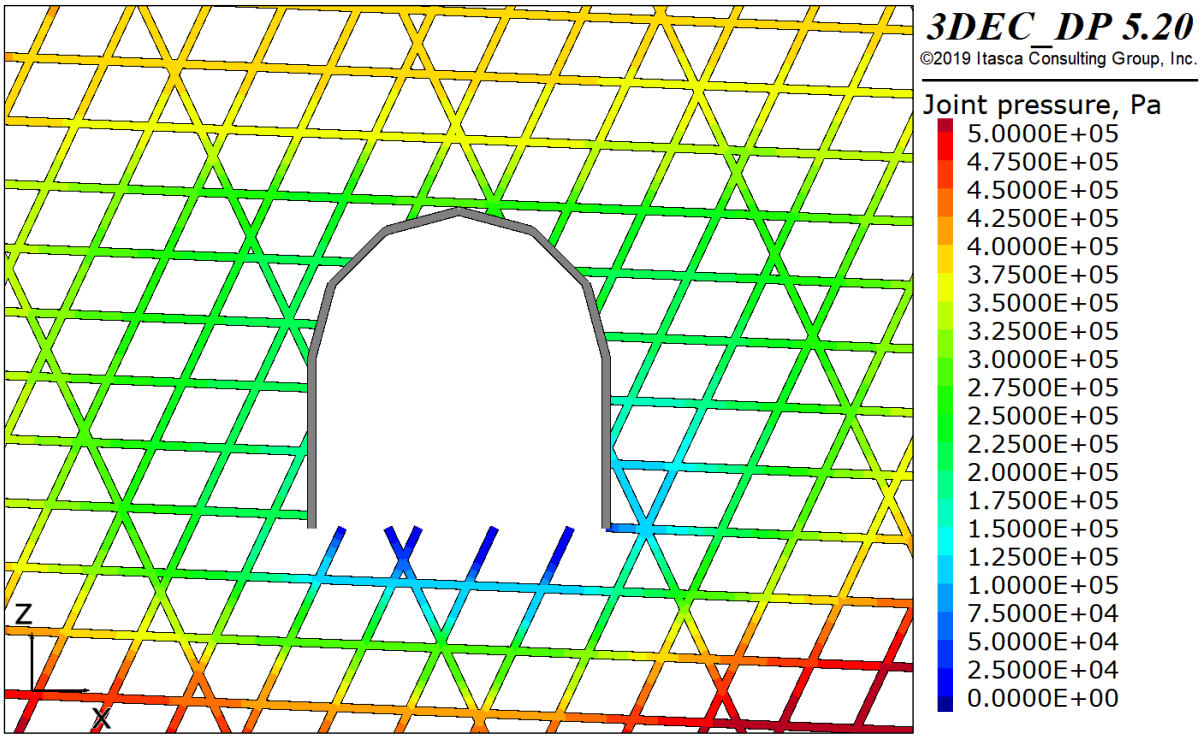

Figure 8.16: Cross-section showing the water pressure in distinct joints for scenario 1.2. The width of the lines is uniform and is not related to the hydraulic apertures of the joints.

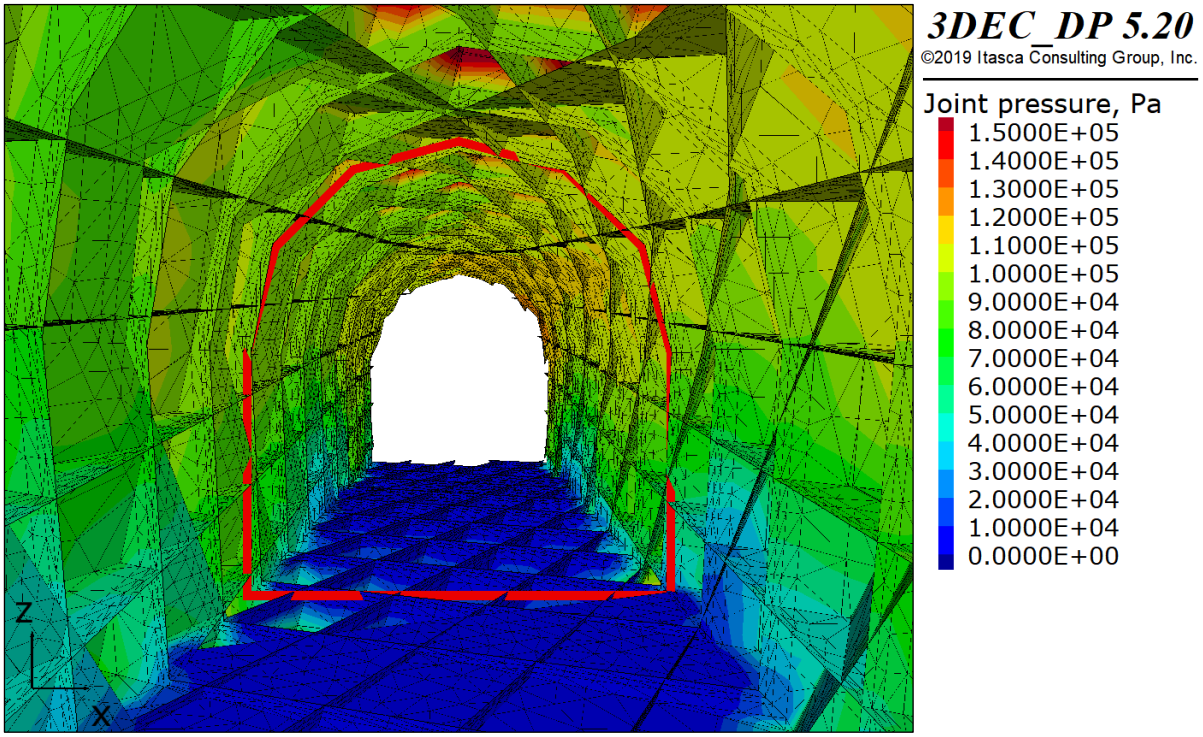

Figure 8.17: Perspective view of the joint pressure at the excavation boundary for scenario 2.2. The maximum pressure is approximately 110–120 kPa. Minor variations in the direction of the tunnel axis are observed. The location of the plane where the model is cut in Figs. 8.18 and 8.19 is indicated by a red line along the tunnel circumference. Only the middle 40 m of the model are shown.

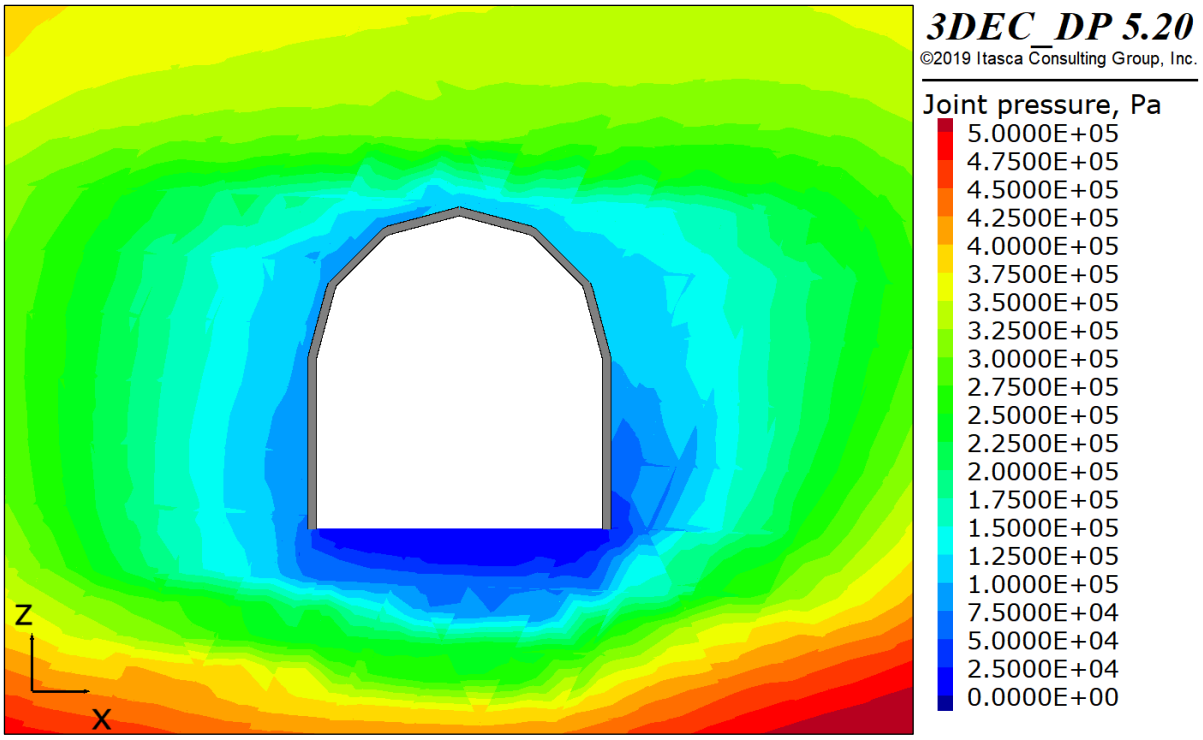

Figure 8.18: Orthographic view of the joint pressure field for scenario 2.2. Ten metres laterally into the rock mass, the joint pressure is approximately 300 kPa.

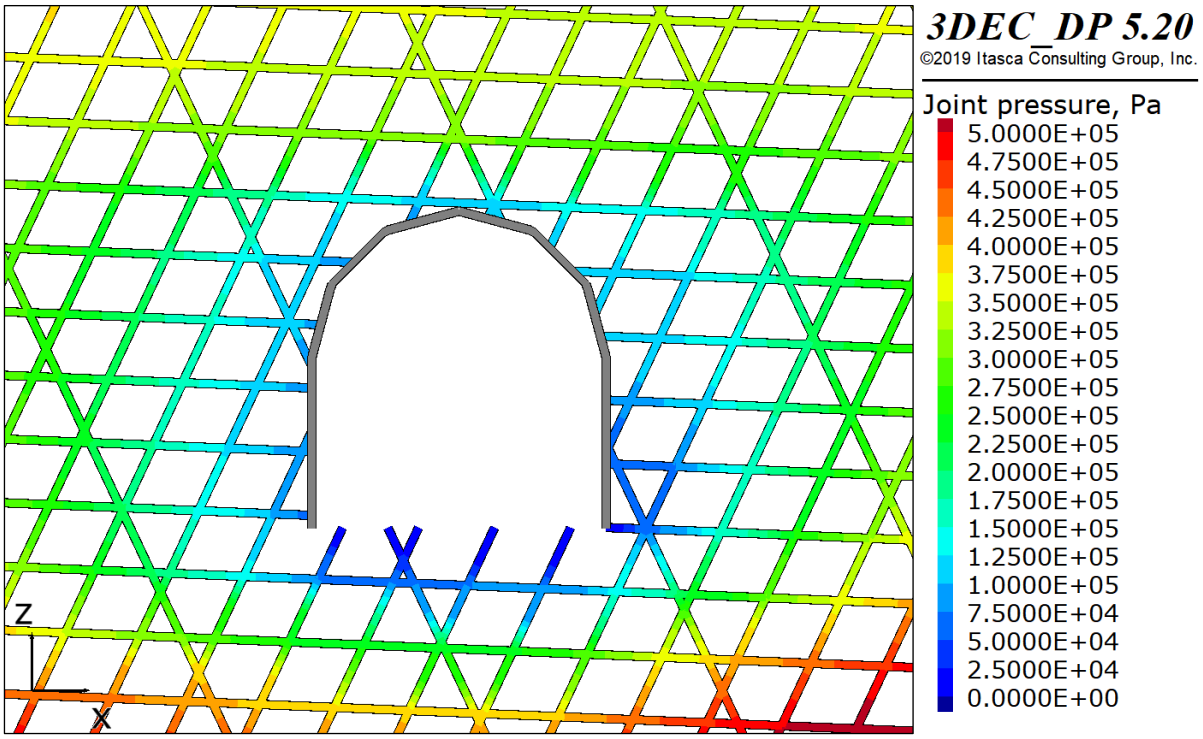

Figure 8.19: Cross-section showing the water pressure in distinct joints for scenario 1.2. The width of the lines is uniform and is not related to the hydraulic apertures of the joints.

9 Discussion

9.1 Comparison between Simulated and Measured Pressures

When no construction damage is included, both the FE model and the DE model predict too high groundwater pressures behind the SCL. If no change in hydraulic apertures is allowed, the DE simulations predict a pressure close to 0.5 MPa at the centre of the tunnel crown, only slightly lower than the hydrostatic pressure of 0.6 MPa. Even when the joint hydraulic apertures in the DE model are allowed to change in response to rock mass deformations and stress redistribution, the simulated pressure still exceeds 0.3 MPa. The FE model predicts a pressure close to 0.4 MPa when no CDZ is included. This is more than half the hydrostatic groundwater pressure, and is not in agreement with previous investigations (Section 4.3). To obtain agreement with the measurements performed immediately behind the SCL in the Gevingåsen tunnel, an increase in the hydraulic conductivity of between one and two orders of magnitude in the region within 0.4 m from the excavation boundary is necessary. This is equivalent to an increase in the joint hydraulic apertures with a factor 2–4, and produces groundwater pressures similar to those measured by Holter et al. (2015). Based on the literature, such an increase in the hydraulic conductivity within the CDZ seems reasonable. For example, it is similar to what is obtained using the harmonic mean of the injection test measurements performed by Ericsson et al. (2015) at the Äspö HRL. Also, it is in agreement with the results found by Chandler et al. (1996).

The relative differences between the pressures measured by the three piezometers used by Holter et al. (2015) are not captured by the model. The model predicts a smaller relative difference between the point at the centre of the crown and the points 2 m below. This might be due to smaller hydraulic apertures in the crown, and larger apertures in the walls in reality than in the model. In the DE simulations, the hydraulic apertures within each region representing the CDZ were nearly uniform in space. As mentioned earlier, this might not be realistic. However, the differences measured by Holter et al. might simply be due to random local variations in the rock mass. Looking at the measurements from the Karmsund test site (Holter, 2014), this is substantiated. These measurements show the opposite of what is intuitively expected; the lowest pressure is measured in the borehole furthest away from the invert. Therefore, it is not possible to say, neither based on the measurements nor on the simulations, what is the typical pressure distribution along the excavation boundary.

There is reason to believe that the modelling does not produce the correct pressures some distance away from the excavation boundary. At the Karmund test site, Holter (2014) measured groundwater pressures close to hydrostatic pressure at the end of the 9 m long boreholes (Section 4.3.2). Those measurements suggest a rather abrupt pressure reduction with high gradient close to the excavation boundary. When the CDZ was included in the DE model in this study, the groundwater pressure at a similar distance from the excavation boundary was only roughly half the hydrostatic pressure. This can probably be explained by the infinite joint persistence and perfect interconnectivity between joints in the numerical model. Imagine, for example, a point in the rock mass a couple of metres above and to the side of the tunnel. Due to the infinite persistence and perfect interconnectivity, water in this point is free to flow into the CDZ by a short and nearly straight path. Once

the groundwater enters the CDZ, where the hydraulic conductivity is higher, it flows towards the drained invert with less resistance. Thus the CDZ provides an effective flow path to the invert not only from points close to the excavation boundary, but also from points further away. The same happens in the FE model, of course. The lack of agreement with the measurements from the Karmsund tunnel might be due to the excessive joint persistence in the DE model, or may suggest imperfect joint interconnectivity in reality. Remember, however, that the above observations assume that the conditions at the Karmsund test site are similar to those in the Gevingåsen tunnel. The actual pressure field away from the excavation boundary in the Gevingåsen tunnel has not been measured.

9.2 Comparison between the FE and DE Simulations

At first, the agreement between the FE modelling and the DE modelling might seem reasonably good. Without going into details (the figures in Chapters 6 and 8 can easily be compared as desired), suffice it to say that both models produce groundwater pressures of 0.3–0.4 MPa at the centre of the tunnel crown when no construction damage is included. However, this is provided that changes in the hydraulic apertures generated by the DE model itself are permitted. The agreement is not so good for the reference scenario of the DE simulations, which results in a maximum groundwater pressure at the excavation boundary that is 0.1 MPa higher than in the FE model.

In the DE model, the transmissivities of the joints change as blocks translate, rotate, and deform. Such changes in the hydraulic properties are not included in the FE model. In other words, the DE model includes effects related to excavation damage even when the CDZ is not represented. In fact, these effects give a significant contribution to the pressure reduction relative to the hydrostatic pressure, and their inclusion in the DE model gives valuable insight that an FE model cannot provide.

9.3 Comparison between the Two Virgin Stress Fields

Scenario 2.1 with an anisotropic stress field, produced a maximum joint pressure at the excavation boundary that was approximately 70–80 kPa lower than in scenario 1.1, with an isotropic stress field. The pressure was generally lower along the entire excavation boundary, and more similar in the two tunnel walls. This can probably be attributed to the low-stress areas with hydraulic aperture increase in the walls.

The aperture increase seemed to occur below the lowermost row of bolts. The joint pressures remaining in the rock mass would possibly have been higher if an additional row of bolts had been installed close to the bottom of the walls. This means that the type, quantity, and geometry of the rock support might have a significant influence on the groundwater pressure field. Similarly, the time of installation of the support is expected to have an influence. For example, lower groundwater pressures are expected if the support is installed a certain distance behind the face, as the joint displacements at the time of installation will be larger. In other words, the support will then have a less important role in restraining joint displacements.

When the CDZ was included in the simulations, the pressures were still lower for stress field scenario 2, both at the excavation boundary and 10 m into the rock mass. This means that other factors still have an influence even when the construction damage is dominant in determining the hydraulic apertures close to the excavation boundary. In other words, damage that is independent of the excavation method still has an effect, although less important when there is considerable construction damage.

It should be remembered that the DE model was not completely stable for the anisotropic stress field scenario. The results for this stress field scenario are, therefore, more uncertain than those for the isotropic stress field scenario. The joint pressures obtained may be too low as unstable convergence will produce excessively large joint hydraulic apertures. This might also affect tunnel sections that are stable. Consequently, the difference seen between the two stress field scenarios may be unrealistically large.

9.4 Solid-Fluid Coupling

One important consideration during the DE modelling was the choice of coupling between joint pressures and deformations. In the end, a type of full coupling with certain limitations was used. Each stage of mechanical calculations was preceded by a flow calculation to determine the joint pressures used for the effective stress-based mechanical analysis. During the mechanical calculation, the hydraulic apertures changed, thus affecting the joint pressure field calculated in the next stage. One weakness with this approach is that the joint pressure field has an unrealistically important role in driving mechanical deformations because the response between deformations and joint pressures is slow. The joint pressure field does not change during the mechanical calculation, that is, it does not change in response to changes in the joint hydraulic aperture during the same stage. Only prior to the next stage of mechanical calculations is the joint pressure field updated. Therefore, the joint pressure contribution to the forces driving the deformations remains constant throughout the mechanical calculation in each stage. Consequently, the joint normal displacement and, hence, the increase in hydraulic apertures are overestimated. This will, ultimately, result in an underestimation of the joint pressures. To remedy this problem it was attempted to use other types of coupling, including fully coupled logic, which, had it worked, would have solved the problem. However, these attempts were not successful. One reason for this was that the fully coupled logic in *3DEC* assumes a quasi-static model, in the sense that the mechanical model is in equilibrium for the current distribution of joint pressures.

9.5 Representation of the CDZ

In this study, the effect of damage created directly by excavation works (i.e., the CDZ) has been represented by manually increasing the hydraulic aperture of natural joints. More specifically this was done by increasing the minimum aperture. This probably does not result in a perfectly realistic representation of the combined effects of construction damage and mechanical effects. However, it provided a way of studying the fundamental effect of construction damage. Other ways of implementing the CDZ could also have been included in the study, but this was not possible within the given time frame.

It is also acknowledged that the approach chosen in this study fails to represent new fractures created due to excavation damage. The attempt of representing such joints explicitly was found not to be feasible with the software and time available. It would have been possible to represent the blast-induced fractures by a matrix conductivity in the region close to the excavation boundary. This approach would have to assume that the blast-induced fractures create a continuous network, which might not be the case. Possibly, the blast-induced fractures are not of primary importance to the steady state groundwater pressure field. For example, Olsson et al. (2009) find no evidence of a continuous network of blast-induced fractures at the Äspö HRL. They also observe that the blast-induced fractures are influenced strongly by natural fractures, and that the longer natural fractures control the groundwater flow.

9.6 Inadequacies of the DE Model

9.6.1 Numerical Formulation of Joint Fluid Flow

There are several assumptions made in *3DEC* that might, or certainly do differ from actual conditions. One that is considered particularly important to the topic investigated in this thesis, is the parallel plate model for joint fluid flow. The parallel plate model assumes that joint fluid flow takes place in infinite slits between smooth parallel walls. In reality this is never the case. Actual joints are rough (to a lesser or greater extent) and may also be partially filled. Correct choice of the hydraulic aperture might counter some of the differences between the mathematical model and real joints, but not all. For example, the inflow to a tunnel may often be observed to occur as point leakages. This would mean that the flow mostly occurs in one-dimensional channels rather than in two-dimensional slits. If this is the case, it can hardly be expected that the relation between mechanical deformations and changes in the hydraulic aperture *3DEC* is accurate. Equation (2.11), stating that the change in hydraulic aperture is equal to the joint normal displacement, is accurate only for smooth and interlocked joints. For mismatched or rough joints, the change in hydraulic aperture will be less than the joint normal displacement (Witherspoon et al., 1980, Alvarez et al., 1995, Zimmerman and Bodvarsson, 1996). This would mean that the opening of joints that experience normal stress relief would be smaller, possibly leading to higher groundwater pressures behind the lining. The presence of flow channels, on the other hand, could lead to lower groundwater pressures by providing low-resistance flow paths to the invert. The joints in the Gevingåsen tunnel are generally quite smooth with little or no infilling. Therefore, the problems outlined above is probably not very severe in this case. However, it is certainly relevant.

9.6.2 Model Geometry

9.6.2.1 Model size

There are also possible sources of error related to the geometry of the *3DEC* model. The limited extent of the model is one example. Although probably not the largest source of error, Fig. 8.13 illustrates that the influence of the tunnel reaches all the way to the model edge. Ideally, the model should therefore have been larger. However, this would have negatively affected the calculation time, which was already on the verge of unacceptable. Larger model extent would lead to lower pressure on the excavation boundary.

9.6.2.2 Joint network

Another source of error related to the geometry is the simplifications made to the joint network. In this study, the joint network was simplified to one that consists of three sets of infinitely persistent joints with constant joint orientation within each set. Both the persistence and spacing of the joints are larger in the model than in reality. Initially, it was attempted to introduce stochastic features into the fracture geometry, for example, in the form of randomly distributed joint spacings, orientations, and persistences. However, problems arise if the jointing generates sliver-shaped blocks. Sliver-shaped blocks create problems during meshing, particularly when the grid is configured for fluid flow. In the end, it was decided to simplify the joint geometry to the one that has been previously presented, not only to avoid these problems, but also to create a simpler geometry that made the model easier to analyse. Of course, this comes at the expense of some effects that would have been present with a more complex representation of the joint network. For example, finite joint persistence in the model could have lengthened the flow paths to the invert, thus leading to a higher groundwater pressure behind the lining. Smaller joint spacing

would have had the opposite effect. Also, the possibility of highly local variations is not captured with the simple joint network. However, this would have been difficult to capture in any numerical model, no matter how complex.

9.6.3 Geochemical Processes

There are also phenomena that are not included in the model at all, for example, geochemical processes. With time, minerals may precipitate, and clay particles may sediment in the fractures close to the excavation boundary. This might lead to a reduction of the transmissivity with time, and thus an increase in the joint pressure behind the lining. The opposite can also theoretically happen: the transmissivity may gradually increase due to dissolution of joint filling or intact rock. This would lead to a decrease in the joint pressure with time. However, considering the condition of the joints (mostly without filling) and the type of rock in the area, this is considered unlikely.

9.6.4 Other Uncertainties

Finally, there is a range of other uncertainties. The effects of weakness zones and spatial variations in rock mass properties are not considered, the block and joint constitutive models do not perfectly describe the behaviour of the real rock mass, and the virgin stress field and other estimated input parameters might not be perfectly accurate. For example, it has been shown that the estimated joint shear strength properties might be conservative. Within the time frame of the study, it was not possible to redo the calculations with more favourable strength properties. Therefore, it is not known exactly how this would affect the results. However, using the equations related to the Barton-Bandis slip model that describe the joint normal stiffness (Eqs. (2.23)–(2.27)), one finds that an increase in the JRC or the JCS leads to a decrease in the joint normal stiffness. Lower joint normal stiffness would lead to an increased opening of joints that experience stress relief, and, therefore, possibly lower groundwater pressure behind the lining. To summarise, there are many sources of error whose overall effect on the simulation results is not possible to tell.

9.7 Further Work

Further work is needed to gain more knowledge regarding the groundwater pressure behind partially drained tunnel lining structures. The results of this thesis are related to specific site conditions, and are subject to several factors of uncertainty. There are also a number of questions that have not been investigated. The following points are suggested for future research:

- Inclusion of a DFN in the DE model. A DFN might, for example, be constructed for the conditions in the Gevingåsen tunnel. The results may then be compared with those presented in this thesis. Inclusion of a DFN in *3DEC* could, based on the experiences from working with this thesis, be difficult to achieve. However, it should be possible if appropriate simplifications are made.
- Investigation of the effect of other parameters upon the groundwater pressure, for example, joint spacing, joint persistence, other virgin stress field conditions, joint sets with different fracture transmissivities, and so on.
- Execution of injection tests to measure the hydraulic conductivity of the CDZ in the Gevingåsen tunnel and in other Norwegian tunnels. SINTEF is currently building the necessary equipment. With such measurements it should be possible to perform forward modelling, rather than simply back-calculations, which has been the focus of this thesis. One important question, however, is how to treat the measurement data in a

meaningful way to obtain model input parameters. Comparison with results from this thesis can prove useful in that regard.

10 Conclusions

This thesis has presented a back-calculation of the hydraulic properties of the construction damage zone (CDZ) in the Gevingåsen railway tunnel in Trøndelag, Norway, based on existing groundwater pressure measurements presented by Holter et al. (2015) from behind the partially drained sprayed concrete lining (SCL) in the tunnel. The study included field and laboratory investigations to determine properties of the intact rock, discontinuities, and rock mass, two-dimensional finite element modelling in the software *RS2*, and three-dimensional distinct element modelling in the software *3DEC.* The main findings of the study are:

- Based on observed water conditions in the tunnel, the effective hydraulic conductivity of the undisturbed rock mass is estimated to be approximately 1×10^{-8} m/s. This corresponds to a joint hydraulic aperture of approximately 3×10^{-5} m.
- Without any change in the rock mass hydraulic properties due to the tunnel excavation, the maximum rock joint water pressure immediately behind the partially drained SCL is simulated to be close to 0.5 MPa, occurring at the centre of the crown. This constitutes a small reduction relative to the hydrostatic pressure of 0.6 MPa.
- Even without a CDZ, the pressure will, in reality, probably be lower due to rock mass deformations and stress redistribution that increase the hydraulic aperture of some natural joints. The maximum joint pressure immediately behind the partially drained SCL is simulated to be in the order of 0.3–0.4 MPa, when joint normal displacements are allowed to affect the joint hydraulic apertures in the *3DEC* model. This is, however, still more than half the hydrostatic pressure, and considerably higher than what has been measured.
- A hydraulic conductivity increase between one and two orders of magnitude in a CDZ is necessary to explain the measured groundwater pressures. This corresponds to a hydraulic aperture increase with a factor 2–4. When such a hydraulic aperture increase is included in the region within 0.4 m from the excavation boundary, the simulations result in joint pressures no higher than approximately 0.16 MPa. For comparison, the pressure measured by Holter et al. (2015) at the centre of the crown is 0.135 MPa. A hydraulic conductivity increase of between one and two orders of magnitude in the CDZ is considered reasonable based on the literature.
- The simulations show that the groundwater pressure may be considerably lower than the hydrostatic pressure not only at the excavation boundary, but also reasonably far into the surrounding rock mass if its hydraulic characteristics are favourable in this regard. However, the far-reaching pressure reduction does not agree with the measurements performed in boreholes in the Karmsund tunnel (Holter, 2014). If the actual situation in the Gevingåsen tunnel is similar to those in the Karmsund tunnel, the deviating simulation results might be due to unrealistically large joint persistence and perfect joint interconnectivity in the *3DEC* model.
- An anisotropic stress field with gravitational vertical stress and a total stress ratio of two produced lower pressures behind the SCL than an isotropic stress field with the same mean stress. This was the case both with and without a CDZ. The difference is probably due to larger low-stress areas with hydraulic aperture increase in the walls, when the virgin stress field is anisotropic. This illustrates that the virgin stress field may have a significant effect on the pressures.

- The pressure field is probably affected by the type, quantity and installation time of the rock support, as the rock support restrains the joint normal displacements. For the studied scenario with anisotropic stress field, the hydraulic aperture increase in the *3DEC* model was most pronounced below the lowermost row of bolts.

There are many uncertainties, assumptions and limitations related to the presented simulations. For example, it was found that the estimated joint strength properties might have been conservative. Also, only a couple of scenarios, with no variations in the majority of input parameters, have been investigated. Therefore, the conclusions are not necessarily relevant to other situations. More work related to the groundwater pressure behind partially drained tunnel linings is necessary to draw broadly valid conclusions. Several questions still remain to be answered.

References

Alvarez, T. A., Cording, E. J. and Mikhail, R. A. (1995) Hydromechanical behavior of rock joints: A re-interpretation of published experiments. Paper presented at *The 35th U.S. Symposium on Rock Mechanics (USRMS)*, Reno, Nevada, USA, 5–7 June 1995.

Aydin, A. (2009) ISRM suggested method for determination of the Schmidt hammer rebound hardness: Revised version, *International Journal of Rock Mechanics and Mining Sciences*, 46(3), pp. 627–634. doi: 10.1016/j.ijrmms.2008.01.020

Aydin, A. (2014) Upgraded ISRM suggested method for determining sound velocity by ultrasonic pulse transmission technique, *Rock Mechanics and Rock Engineering*, 47(1), pp. 255–259. doi: 10.1007/s00603-013-0454-z

Bandis, S. C., Lumsden, A. C. and Barton, N. R. (1983) Fundamentals of rock joint deformation, *International Journal of Rock Mechanics and Mining Sciences & Geomechanics Abstracts*, 20(6), pp. 249–268. doi: 10.1016/0148-9062(83)90595-8

Bane NOR (2017) *Teknisk designbasis for InterCity-strekningene*. (ICP-00-A-00030). Bane NOR. Available at: https://www.banenor.no/globalassets/documents/inter-city/teknisk-designbasis.pdf (accessed: 22 January 2019).

Bane NOR (2018a) *Anbefalt konstruksjonsprinsipp for jernbanetunneler.* Available at: https://prosjekteringsveileder.jbv.no/wiki/veiledere/jernbanetunneler_anbefalt_konstruksjonsprinsipp (accessed: 25 January 2019).

Bane NOR (2018b) *Tunneler/Prosjektering og bygging/Vannsikring.* Available at: https://trv.banenor.no/wiki/Tunneler/Prosjektering_og_bygging/Vannsikring (accessed: 26 January 2019).

Barton, N. (1973) Review of a new shear-strength criterion for rock joints, *Engineering Geology*, 7(4), pp. 287–332. doi: 10.1016/0013-7952(73)90013-6

Barton, N. (1976) The shear strength of rock and rock joints, *International Journal of Rock Mechanics and Mining Sciences & Geomechanics Abstracts*, 13(9), pp. 255–279. doi: 10.1016/0148-9062(76)90003-6

Barton, N. (1978) Suggested methods for the quantitative description of discontinuities in rock masses: International Society for Rock Mechanics, *International Journal of Rock Mechanics and Mining Science*, 15(6), pp. 319–368. Available at: https://www.isrm.net/fotos/gca/1158224359isrm_sm_quantitative_description_of_discontinuities_-_1978.pdf (accessed: 4 February 2019).

Barton, N. (1982) *Modelling rock joint behaviour from in situ block tests: implications for nuclear waste repository design*. (ONWI-308). Salt Lake City, Utah: Office of Nuclear Waste Isolation (ONWI). Available at: https://www.researchgate.net/publication/236433630_Modelling_rock_joint_behavior_from_in_situ_block_tests_Implications_for_nuclear_waste_repository_design (accessed: 7 February 2019).

Barton, N. (1988) *Predicting the behaviour of underground openings in rocks*. (NGI Publication 172). Oslo: The Norwegian Geotechnical Institute (NGI).

Barton, N. (2002) Some new Q-value correlations to assist in site characterisation and tunnel design, *International Journal of Rock Mechanics and Mining Sciences*, 39(2), pp. 185–216. doi: 10.1016/S1365-1609(02)00011-4

Barton, N. (2003) *Teoretisk og empirisk forståelse av forinjeksjon og mulighet for redusert sikringsmengde i utvalgte tunnelstrekninger*. (Intern rapport nr. 2323). Oslo: Statens vegvesen, Vegdirektoratet, Teknologiavdelingen. Available at: https://www.vegvesen.no/fag/fokusomrader/forskning+og+utvikling/Avsluttede+FoU-program/miljovennlige-tunneler/rapporter (accessed: 26 November 2018).

Barton, N. and Bandis, S. (1982) Effects of block size on the shear behavior of jointed rock. Paper presented at *The 23rd U.S Symposium on Rock Mechanics (USRMS)*, Berkeley, California, USA, 25–27 August 1982.

Barton, N. and Bandis, S. (1990) Review of predictive capabilities of JRC-JCS model in engineering practice, in Barton, N. and Stephansson, O. (eds.) *Rock joints : proceedings of the International Symposium on Rock Joints*, Loen, Norway, 4–6 June 1990. Rotterdam: Balkema, pp. 603–610.

Barton, N. and Choubey, V. (1977) The shear strength of rock joints in theory and practice, *Journal of the International Society of Rock Mechanics / Felsmechanik / Mécanique des roches*, 10(1), pp. 1–54. doi: 10.1007/BF01261801

Barton, N., Lien, R. and Lunde, J. (1974) Engineering classification of rock masses for the design of tunnel support, *Rock Mechanics Felsmechanik Mécanique des Roches*, 6(4), pp. 189–236. doi: 10.1007/BF01239496

Basu, A. and Aydin, A. (2004) A method for normalization of Schmidt hammer rebound values, *International Journal of Rock Mechanics and Mining Sciences*, 41(7), pp. 1211–1214. doi: 10.1016/j.ijrmms.2004.05.001

Bieniawski, Z. T. and Bernede, M. J. (1979) Suggested methods for determining the uniaxial compressive strength and deformability of rock materials, *International Journal of Rock Mechanics and Mining Science*, 16(2), pp. 137–140. Available at: https://www.isrm.net/fotos/gca/1129631264isrm_sm_uniaxial_compressive_strength_and_deformability-_1979.pdf (accessed: 5 February 2019).

Bossart, P., Meier, P. M., Moeri, A., Trick, T. and Mayor, J.-C. (2002) Geological and hydraulic characterisation of the excavation disturbed zone in the Opalinus Clay of the Mont Terri Rock Laboratory, *Engineering Geology*, 66(1), pp. 19–38. doi: 10.1016/S0013-7952(01)00140-5

Bryne, L. E., Ansell, A. and Holmgren, J. (2014) Laboratory testing of early age bond strength of shotcrete on hard rock, *Tunnelling and Underground Space Technology*, 41, pp. 113–119. doi: 10.1016/j.tust.2013.12.002

Bäckblom, G. (2008) *Excavation damage and disturbance in crystalline rock - results from experiments and anlyses*. (SKB TR-08-08). Stockholm: Svensk kärnbränslehantering AB (SKB). Available at: https://www.skb.se/publikation/1931340/ (accessed: 30 January 2019).

Carranza-Torres, C. and Fairhurst, C. (2000) Application of the convergence-confinement method of tunnel design to rock masses that satisfy the Hoek-Brown failure criterion, *Tunnelling and Underground Space Technology*, 15(2), pp. 187–213. doi: 10.1016/S0886-7798(00)00046-8

Chandler, N. A., Kozak, E. T. and Martin, C. D. (1996) Connected pathways in the EDZ and the potential for flow along tunnels, in Martino, J. B. and Martin, C. D. (eds.) *Designing the excavation disturbed zone for a nuclear repository in hard rock: proceedings of a Canadian Nuclear Society workshop*, Winnipeg, Canada, 20 September 1996. Toronto: Canadian Nuclear Society, pp. 25–34.

Chen, S. H., Feng, X. M. and Isam, S. (2008) Numerical estimation of REV and permeability tensor for fractured rock masses by composite element method, *International Journal for Numerical and Analytical Methods in Geomechanics*, 32(12), pp. 1459–1477. doi: 10.1002/nag.679

Chern, J. C., Shiao, F. Y. and Yu, C. W. (1998) An empirical safety criterion for tunnel construction, in Ou, C.-d. (ed.) *Sedimentary Rock Engineering : Proceedings of Regional Symposium on Sedimentary Rock Engineering*, Taipei, Taiwan, 22–20 November 1998. Taipei: Public Construction Commission, pp. 222–227.

Corbetta, F., Bernaud, D. and Minh, D. N. J. R. F. d. G. (1991) Contribution à la méthode convergence-confinement par le principe de la similitude, *Rev. Fr. Géotech.*, (54), pp. 5–11. doi: 10.1051/geotech/1991054005

Cundall, P. A. and Strack, O. D. L. (1979) A discrete numerical model for granular assemblies, *Géotechnique*, 29(1), pp. 47–65. doi: 10.1680/geot.1979.29.1.47

Darcy, H. (1856) *Les fontaines publiques de la ville de Dijon: exposition et application*. Paris: Victor Dalmont.

Deere, D. U. and Miller, R. P. (1966) *Engineering classification and index properties for intact rock*. (Technical Report No. AFWL-TR-65-116). Urbana, Illinois: University of Illinois,. Available at: https://apps.dtic.mil/dtic/tr/fulltext/u2/646610.pdf (accessed: 4 February 2019).

DYWIDAG Norge AS (2016) *GEWI® Varmgalvanisert: Typetegning/Datablad*. DYWIDAG Norge AS. Available at: http://www.dywidag-norge.no/wp-content/uploads/2017/04/GEWI-fjellsikring.pdf (accessed: 15 February 2019).

El Tani, M. (2003) Circular tunnel in a semi-infinite aquifer, *Tunnelling and underground space technology*, 18(1), pp. 49–55. doi: 10.1016/S0886-7798(02)00102-5

EPRI (1992) *Uplift pressures, shear strengths, and tensile strengths for stability analysis of concrete gravity dams. Volume 1: final report*. (TR 100345). Electric Power Reasearch Institute (EPRI).

Ericsson, L. O., Thörn, J., Christiansson, R., Lehtimäki, T., Ittner, H., Hansson, K., Butron, C., Sigurdsson, O. and Kinnbom, P. (2015) *A demonstration project on controlling the excavation-damaged zone - experience from the Äspö Hard Rock Laboratory*. (SKB R-14-30). Stockholm: Svensk kärnbränslehantering AB (SKB). Available at: https://www.skb.se/publikation/2480345/ (accessed: 3 January 2019).

Esmaieli, K., Hadjigeorgiou, J. and Grenon, M. (2010) Estimating geometrical and mechanical REV based on synthetic rock mass models at Brunswick Mine, *International*

Journal of Rock Mechanics and Mining Sciences, 47(6), pp. 915–926. doi: 10.1016/j.ijrmms.2010.05.010

Fabian, D., Peter, C., Daniel, B. and Torsten, G. (2007) Evaluation of damage-induced permeability using a three-dimensional Adaptive Continuum/Discontinuum Code (AC/DC), *Physics and Chemistry of the Earth, Parts A/B/C*, 32(8), pp. 681–690. doi: 10.1016/j.pce.2006.01.006

Franklin, J. A. (1985) Suggested method for determining point load strength, *International Journal of Rock Mechanics and Mining Sciences & Geomechanics Abstracts*, 22(2), pp. 51–60. doi: 10.1016/0148-9062(85)92327-7

Franklin, J. A., Vogler, U. W., Szlavin, J., Edmond, J. M. and Bieniawski, Z. T. (2007) Suggested methods for determining water content, porosity, density, absorption and related properties and swelling and slake-durability index properties in Ulusay, R. and Hudson, J. A. (eds.) *The Complete ISRM Suggested Methods for Rock Characterization, Testing and Monitoring: 1974–2006.* Ankara: Commission on Testing Methods, International Society of Rock Mechanics, pp. 143–159.

Fransson, Å. (2002) Nonparametric method for transmissivity distributions along boreholes, *Groundwater*, 40(2), pp. 201–204. doi: 10.1111/j.1745-6584.2002.tb02505.x

Furbish, D. J. (1996) *Fluid physics in geology: an introduction to fluid motions on Earth's surface and within its crust*. New York: Oxford University Press.

Grimstad, E., Kankes, K., Bhasin, R. and Wold Magnussen, A. (2002) Rock mass quality Q used in designing reinforced ribs of sprayed concrete and energy absorption. Paper presented at *Fourth International Symposium on Sprayed Concrete – Modern Use of Wet Mixed Sprayed Concrete for Underground Support*, Davos, Switzerland, 22–26 September 2002.

Gustafson, G. (2009) *Hydrogeologi för bergbyggare*. Stockholm: BeFo.

Gustafson, G. and Fransson, Å. (2005) The use of the Pareto distribution for fracture transmissivity assessment, *Hydrogeology Journal*, 14(1), pp. 15–20. doi: 10.1007/s10040-005-0440-y

Harrison, J. P. and Hudson, J. A. (2000) *Engineering rock mechanics part 2: illustrative worked examples*. Elsevier. doi: 10.1016/B978-0-08-043010-2.X5000-X.

Hoek, E. (1994) Strength of rock and rock masses, *ISRM News J*, 2(2), pp. 4–16. Available at: https://www.isrm.net/fotos/gca/1332169399isrm_newsjournal_-_1994,_volume_2,_number_2_web.pdf (accessed: 8 January 2019).

Hoek, E. (2006a) In situ and induced stresses, in Hoek, E. (ed.) *Practical rock engineering.* Toronto: Rocscience.

Hoek, E. (2006b) Shear strength of rock discontinuities, in Hoek, E. (ed.) *Practical rock engineering.* Toronto: Rocscience.

Hoek, E. and Diederichs, M. S. (2006) Empirical estimation of rock mass modulus, *International Journal of Rock Mechanics and Mining Sciences*, 43(2), pp. 203–215. doi: 10.1016/j.ijrmms.2005.06.005

Hoek, E. and Marinos, P. (2000) Predicting tunnel squeezing problems in weak heterogeneous rock masses, *Tunnels and Tunnelling International*, 132(11), pp. 45–51.

Available at: https://www.rocscience.com/assets/resources/learning/hoek/Predicting-Tunnel-Squeezing-Problems-in-Weak-Heterogeneous-Rock-Masses-2000.pdf (accessed: 8 January 2019).

Hoek, E., Marinos, P. G. and Marinos, V. P. (2005) Characterisation and engineering properties of tectonically undisturbed but lithologically varied sedimentary rock masses, *International Journal of Rock Mechanics and Mining Sciences*, 42(2), pp. 277–285. doi: 10.1016/j.ijrmms.2004.09.015

Hoek, E., T. Carranza-Torres, C., Corkum, B., Hoek, E. and Carranza-Torres, C. (2002) Hoek-Brown failure criterion - 2002 Edition, in Reginald, H., Bawden, W. F., Curran, J. C. and Telesnicki, M. (eds.) *NARMS-TAC 2002 : Mining and Tunnelling Innovation and Opportunity*, Toronto, Ontario, Canada, 7–10 July 2002. Toronto, Ontario: University of Toronto Press, pp. 267–273.

Holter, K. G. (2014) Loads on sprayed waterproof tunnel linings in jointed hard rock: a study based on norwegian cases, *Rock Mechanics and Rock Engineering*, 47(3), pp. 1003–1020. doi: 10.1007/s00603-013-0498-0

Holter, K. G. (2015) *Properties of waterproof sprayed concrete tunnel linings. A study of EVA-based sprayed membranes for waterproofing of rail and road tunnels in hard rock and cold climate.* Ph.D. thesis, Norwegian University of Science and Technology.

Holter, K. G. (2016) How do sprayed concrete linings with sprayed waterproof membranes function? Findings from a reasearch project for traffic tunnels in hard rock in Norway. Paper presented at *13th International Conference Underground Construction*, Prague, Czech Republic, 23–25 May 2016.

Holter, K. G., Christiansson, R. and Basnet, C. B. (2015) Effects on ground water pressure in the immediate rock mass around partially drained SCL with bonded waterproof membrane, *Unpublished manuscript*.

Hou, Z. (2003) Mechanical and hydraulic behavior of rock salt in the excavation disturbed zone around underground facilities, *International Journal of Rock Mechanics and Mining Sciences*, 40(5), pp. 725–738. doi: 10.1016/S1365-1609(03)00064-9

Huaming, A., Hongyuan, L., Xuguang, W., Jianjun, S. and Haoyu, H. (2017) Hybrid finite-discrete element modelling of blast-induced excavation damaged zone in the top-heading of deep tunnels, *Civil Engineering Journal*, 2017(1), pp. 22–33. doi: 10.14311/CEJ.2017.01.0003

Hudson, J. A., Bäckström, A., Rutqvist, J., Jing, L., Backers, T., Chijimatsu, M., Christiansson, R., Feng, X.-T., Kobayashi, A., Koyama, T., Lee, H.-S., Neretnieks, I., Pan, P.-Z., Rinne, M. and Shen, B.-T. (2009) Characterising and modelling the excavation damaged zone in crystalline rock in the context of radioactive waste disposal, *Environmental Geology*, 57(6), pp. 1275–1297. doi: 10.1007/s00254-008-1554-z

Huitt, J. (1956) Fluid flow in simulated fractures, *AIChE Journal*, 2(2), pp. 259–264. doi: 10.1002/aic.690020224

Itasca Consulting Group Inc. (2016a) *3DEC - Three-Dimensional Distinct Element Code*, *Ver. 5.2*. Minneapolis: Itasca.

Itasca Consulting Group Inc. (2016b) *3DEC Version 5.2: theory and background*. Minneapolis: Itasca.

Itasca Consulting Group Inc. (2016c) *3DEC Version 5.2: user's guide*. Minneapolis: Itasca.

Kulatilake, P. H. S. W. and Panda, B. B. (2000) Effect of block size and joint geometry on jointed rock hydraulics and REV, *Journal of Engineering Mechanics*, 126(8), pp. 850–858. doi: 10.1061/(ASCE)0733-9399(2000)126:8(850)

Lisjak, A., Garitte, B., Grasselli, G., Müller, H. R. and Vietor, T. (2015) The excavation of a circular tunnel in a bedded argillaceous rock (Opalinus Clay): Short-term rock mass response and FDEM numerical analysis, *Tunnelling and Underground Space Technology*, 45, pp. 227–248. doi: 10.1016/j.tust.2014.09.014

Lisjak, A., Tatone, B. S. A., Mahabadi, O. K., Grasselli, G., Marschall, P., Lanyon, G. W., Vaissière, R. d. l., Shao, H., Leung, H. and Nussbaum, C. (2016) Hybrid finite-discrete element simulation of the EDZ formation and mechanical sealing process around a microtunnel in Opalinus Clay, *Rock Mechanics and Rock Engineering*, 49(5), pp. 1849–1873. doi: 10.1007/s00603-015-0847-2

Louis, C. (1969) *A study of groundwater flow in jointed rock and its influence on the stability of rock masses*. London: Imperial College of Science and Technology.

Marinos, P. and Hoek, E. (2001) Estimating the geotechnical properties of heterogeneous rock masses such as flysch, *Bulletin of Engineering Geology and the Environment*, 60(2), pp. 85–92. doi: 10.1007/s100640000090

Marinos, V., Marinos, P. and Hoek, E. (2005) The geological strength index: applications and limitations, *Bulletin of Engineering Geology and the Environment*, 64(1), pp. 55–65. doi: 10.1007/s10064-004-0270-5

Martino, J. B. and Chandler, N. A. (2004) Excavation-induced damage studies at the Underground Research Laboratory, *International Journal of Rock Mechanics and Mining Sciences*, 41(8), pp. 1413–1426. doi: 10.1016/j.ijrmms.2004.09.010

Matheron, G. (1967) *Eléments pour une théorie des milieux poreux*. Paris: Masson.

Mouzannar, H., Bost, M., Leroux, M. and Virely, D. (2017) Experimental study of the shear strength of bonded concrete–rock interfaces: surface morphology and scale effect, *Rock Mechanics and Rock Engineering*, 50(10), pp. 2601–2625. doi: 10.1007/s00603-017-1259-2

Neby, A. (1990) *Permeabilitetsmålinger og hydrauliske splitte/jekke-tester i kloakkrenseanlegg på Ladehammeren*. (SINTEF Rapport STF36 F90104). Trondheim: SINTEF.

NGI (2017) *Using the Q-system. Rock mass classification and support design*. Oslo: NGI.

NNRA (2009) *Hovedløpet Muruvik - Hell NØ. Ingeniørgeologisk tunnelkartlegging. Sikring, sonderboring og injeksjon.* Norwegian National Rail Administration (NNRA) [Jernbaneverket].

Odling, N. E. (1997) Fluid flow in fractured rocks at shallow levels in the Earth´s crust: an overview, in Holness, M. B. (ed.) *Deformation-enhanced Fluid Transport in the Earth's Crust and Mantle.* 1st edn. London: Chapman & Hall, pp. 289–320.

Olsson, M., Markström, I., Petterson, A. and Sträng, M. (2009) *Examination of the Excavation Damaged Zone in the TASS tunnel, Äspö HRL*. (SKB R-09-39). Stockholm:

Svensk kärnbränslehantering AB (SKB). Available at: https://www.skb.se/publikation/2005118/ (accessed: 30 January 2019).

Palmström, A. and Stille, H. (2015) *Rock engineering*. 2 edn. London: ICE Publishing.

Panet, M. (1993) Understanding deformations in tunnels, in Hudson, J. A. (ed.) *Comprehensive rock engineering: principles, practice & projects.* Oxford: Pergamon Press, pp. 663–690.

Panet, M. (1995) *Le calcul des tunnels par la méthode convergence-confinement*. Paris: Presses ENPC.

Panet, M. and Guenot, A. (1982) Analysis of convergence behind the face of a tunnel, in Jones, M. J. (ed.) *Tunnelling '82 : papers presented at the third international symposium*, Brighton, UK, 7–11 June 1982. London: IMM, pp. 197–204.

Paraskevopoulou, C. and Diederichs, M. (2018) Analysis of time-dependent deformation in tunnels using the convergence-confinement method, *Tunnelling and Underground Space Technology*, 71, pp. 62–80. doi: 10.1016/j.tust.2017.07.001

Perras, M. A. and Diederichs, M. S. (2016) Predicting excavation damage zone depths in brittle rocks, *Journal of Rock Mechanics and Geotechnical Engineering*, 8(1), pp. 60–74. doi: 10.1016/j.jrmge.2015.11.004

Poteri, A. and Laitinen, M. (1999) *Site-to-canister scale flow and transport in Hästholmen, Kivetty, Olkiluoto and Romuvaara*. (Posiva 99-15). Helsinki: Posiva Oy. Available at: https://www.skb.se/publikation/2480345/ (accessed: 3 January 2019).

Rocscience Inc. (2019) *RS2*, *Ver. 9.030*. Toronto: Rocscience Inc.

Rocscience Inc. (n.d.) *3D Tunnel Simulation Using Core Replacement.* Available at: https://www.rocscience.com/help/rs2/tutorials/RS2__3D_Tunnel_Simulation.htm (accessed: 15 May 2019).

Rong, G., Peng, J., Wang, X., Liu, G. and Hou, D. (2013) Permeability tensor and representative elementary volume of fractured rock masses, *Hydrogeology Journal*, 21(7), pp. 1655–1671. doi: 10.1007/s10040-013-1040-x

Rutqvist, J., Börgesson, L., Chijimatsu, M., Hernelind, J., Jing, L., Kobayashi, A. and Nguyen, S. (2009) Modeling of damage, permeability changes and pressure responses during excavation of the TSX tunnel in granitic rock at URL, Canada, *Environmental Geology*, 57(6), pp. 1263–1274. doi: 10.1007/s00254-008-1515-6

Saw, H., Villaescusa, E., Windsor, C. R. and Thompson, A. G. (2013) Laboratory testing of steel fibre reinforced shotcrete, *International Journal of Rock Mechanics and Mining Sciences*, 57, pp. 167–171. doi: 10.1016/j.ijrmms.2012.08.008

Snow, D. T. (1965) *A parallel plate model of fractured permeable media.* PhD dissertation, University of California, Berkeley.

Song, S., Sun, F., Chen, J., Zhang, W., Han, X. and Zhang, X. (2017) Determination of RVE size based on the 3D fracture persistence, *Quarterly Journal of Engineering Geology and Hydrogeology*, 50(1), pp. 60–68. doi: 10.1144/qjegh2016-127

Tsang, C.-F., Bernier, F. and Davies, C. (2005) Geohydromechanical processes in the Excavation Damaged Zone in crystalline rock, rock salt, and indurated and plastic clays—

in the context of radioactive waste disposal, *International Journal of Rock Mechanics and Mining Sciences*, 42(1), pp. 109–125. doi: 10.1016/j.ijrmms.2004.08.003

Tveit, M. (2018) *Undersøkelser av sprengningsskadesonen for vurdering av hydraulisk konduktivitet i bergmassen rundt sprengte tunneler.* MSc thesis, NTNU.

Unlu, T. and Gercek, H. (2003) Effect of Poisson's ratio on the normalized radial displacements occurring around the face of a circular tunnel, *Tunnelling and Underground Space Technology*, 18(5), pp. 547–553. doi: 10.1016/S0886-7798(03)00086-5

Vlachopoulos, N. and Diederichs, M. S. (2009) Improved longitudinal displacement profiles for convergence confinement analysis of deep tunnels, *Rock Mechanics and Rock Engineering*, 42(2), pp. 131–146. doi: 10.1007/s00603-009-0176-4

Windsor, C. R. and Thompson, A. G. (1999) The design of shotcrete linings for excavations created by drill and blast methods, in Villaescusa, E., Windsor, C. R. and Thompson, A. G. (eds.) *Rock Support and Reinforcement Practice in Mining.* Rotterdam: Balkema.

Witherspoon, P. A., Wang, J. S., Iwai, K. and Gale, J. E. (1980) Validity of cubic law for fluid flow in a deformable rock fracture, *Water Resources Research*, 16(6), pp. 1016–1024. doi: 10.1029/WR016i006p01016

Zhang, W., Chen, J.-p., Liu, C., Huang, R., Li, M. and Zhang, Y. (2012) Determination of geometrical and structural representative volume elements at the Baihetan Dam site, *Rock Mechanics and Rock Engineering*, 45(3), pp. 409–419. doi: 10.1007/s00603-011-0191-0

Zhang, W., Chen, J., Chen, H., Xu, D. and Li, Y. (2013) Determination of RVE with consideration of the spatial effect, *International Journal of Rock Mechanics and Mining Sciences*, 61, pp. 154–160. doi: 10.1016/j.ijrmms.2013.02.013

Zhu, W. C. and Bruhns, O. T. (2008) Simulating excavation damaged zone around a circular opening under hydromechanical conditions, *International Journal of Rock Mechanics and Mining Sciences*, 45(5), pp. 815–830. doi: 10.1016/j.ijrmms.2007.09.007

Zimmerman, R. W. and Bodvarsson, G. S. (1996) Hydraulic conductivity of rock fractures, *Transport in Porous Media*, 23(1), pp. 1–30. doi: 10.1007/BF00145263

Appendix A: Data from Joint Mapping in the Field

Table A.1: Joint orientations.

Chainage	Joint ID	Joint set	Dip	Dip Direction
120	1	J3	71°	353°
	2	J3	82°	005°
	3	J1	40°	276°
	4	J2	84°	080°
	5	J2	50°	085°
	6	J1	25°	254°
	7	J3	55°	359°
	8	J2	70°	088°
	9	J1	25°	276°
	10	J1	34°	064°
	11	J3	40°	357°
	12	J1	32°	158°
	13	J3	83°	332°
255	14	J2	86°	242°
	15	J3	68°	000°
	16	J1	30°	270°
	17	Random	82°	285°
	18	J2	86°	243°
	19	J1	10°	111°
	20	J3	70°	351°
	21	J3	62°	333°
	22	J2	80°	082°
	23	J2	70°	082°
	24	J1	08°	045°
	25	Random	85°	035°
	26	Random	64°	279°
	27	J1	12°	018°
430	28	J3	70°	323°
	29	J1	20°	187°
	30	J3	73°	003°
	31	J2	89°	072°
	32	J1	44°	138°
	33	J2	86°	076°

Table A.2: Schmidt L hammer rebound values. θ = impact direction (upward is negative).

Joint 1	Joint 32	Joint 33
θ = -19°	θ = 46°	θ = -4°
30	54	43
28	42	40
34	36	37
33	45	41
54	50	23
35	41	37
41	54	38
42	48	22
52	38	28
47	29	23
38	56	41
44	62	36
41	52	28
44	56	36
45	48	37
44	38	39
28	59	46
44	57	37
38	43	37
31	33	41

Appendix B: Joint Profiles Collected in the Field

SET J1

Joint no. 16, 30°/270° (dip/dip dir.):

Joint no 32, 44°/138° (dip/dip dir.)

SET J3

Joint no. 1, 71°/353° (dip/dip dir.):

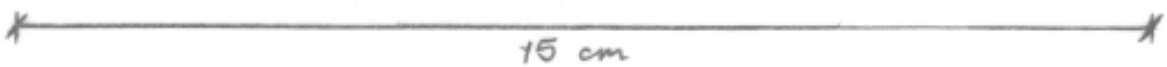

Joint no. 15, 68°/000° (dip/dip dir.):

SET J2

Joint no. 14, 86°/242° (dip/dip dir.)

Joint no. 33, 86°/076° (dip/dip dir.):

Appendix C: Point Load Test Results

Sample Details

Date: 13.02.19

Four block sample from emergency exit tunnel R1 of the Gevingåsen tunnel in Trøndelag, Norway.

Fine-grained, grey metasedimentary rock, varying from relatively homogeneous metasandstone to banded phyllite with pyrite crystals. Both the metasandstone and the phyllite contain quartz bands and lenses.

Specimens:
1–8 Cores from block no. 1 (metasandstone) tested diametrally.
9–16 Cores from block no. 2 (phyllite) tested diametrally.
17–21 Cores from block no. 3 (metasandstone) tested diametrally.
22–25 Cores from block no. 4 (metasandstone) tested diametrally.
26–40 Generated from testing of specimens 1–8, plus additional pieces of core from block 1.
41–54 Generated from testing of specimens 9–16, plus additional pieces of core from block 2.
55–61 Generated from testing of specimens 17–21, plus additional pieces of core from block 3.
62–69 Generated from testing of specimens 62–69, plus additional pieces of core from block 4.

—Stored indoors in the laboratory for 24 hours before preparation, and another 24 hours before testing.
—Tested with a GCTS PLT-100 Point Load Test System.

Specimen	Block no.	Type	W (mm)	D (mm)	P (kN)	D_e (mm)	I_s	F	$I_{s(50)}$
1	1	d ∥	43.8	43.8	8.01	43.8	4.2	0.94	3.9
2	1	d ∥	43.8	43.8	5.77	43.8	3.0	0.94	2.8
3	1	d ∥	43.8	43.8	2.60	43.8			
4	1	d ∥	43.8	43.8	1.96	43.8	1.0	0.94	1.0
5	1	d ∥	43.8	43.8	9.03	43.8	4.7	0.94	4.4
6	1	d ∥	43.8	43.8	6.45	43.8	3.4	0.94	3.1
7	1	d ∥	43.8	43.8	6.39	43.8	3.3	0.94	3.1
8	1	d ∥	43.8	43.8	5.77	43.8	3.0	0.94	2.8
9	2	d ∥	43.8	43.8	4.89	43.8	2.6	0.94	2.4
10	2	d ∥	43.8	43.8	4.14	43.8	2.2	0.94	2.0
11	2	d ∥	43.8	43.8	2.03	43.8	1.1	0.94	1.0
12	2	d ∥	43.8	43.8	2.30	43.8	1.2	0.94	1.1
13	2	d ∥	43.8	43.8	3.75	43.8	2.0	0.94	1.8
14	2	d ∥	43.8	43.8	3.47	43.8	1.8	0.94	1.7
15	2	d ∥	43.8	43.8	4.85	43.8	2.5	0.94	2.4
16	2	d ∥	43.8	43.8	4.16	43.8	2.2	0.94	2.0
17	3	d ∥	43.8	43.8	2.16	43.8	1.1	0.94	1.1
18	3	d ∥	43.8	43.8	3.82	43.8	2.0	0.94	1.9
19	3	d ∥	43.8	43.8	2.77	43.8	1.4	0.94	1.4
20	3	d ∥	43.8	43.8	4.39	43.8	2.3	0.94	2.1
21	3	d ∥	43.8	43.8	6.03	43.8	3.1	0.94	2.9
22	4	d ∥	43.8	43.8	8.15	43.8	4.3	0.94	4.0
23	4	d ∥	43.8	43.8	9.56	43.8	5.0	0.94	4.7
24	4	d ∥	43.8	43.8	4.42	43.8	2.3	0.94	2.2
25	4	d ∥	43.8	43.8	3.63	43.8	1.9	0.94	1.8
26	1	a ⊥	43.8	31.7	13.46	42.0			
27	1	a ⊥	43.8	30.3	17.22	41.1	10.2	0.91	9.3
28	1	a ⊥	43.8	29.7	9.00	40.7			
29	1	a ⊥	43.8	32.2	15.61	42.4			
30	1	a ⊥	43.8	27.3	11.88	39.0			
31	1	a ⊥	43.8	20.8	11.85	34.1	10.2	0.83	8.4
32	1	a ⊥	43.8	24.8	5.30	37.2			
33	1	a ⊥	43.8	22.2	4.37	35.2			
34	1	a ⊥	43.8	24.9	15.18	37.2	11.0	0.86	9.5
35	1	a ⊥	43.8	26.1	12.17	38.1	8.4	0.87	7.3
36	1	a ⊥	43.8	20.8	10.54	34.1	9.1	0.83	7.5
37	1	a ⊥	43.8	28.0	15.90	39.5			
38	1	a ⊥	43.8	27.5	13.69	39.2			
39	1	a ⊥	43.8	36.51	13.41	45.1			
40	1	a ⊥	43.8	33.7	7.79	43.3			
41	2	a ⊥	43.8	41.7	9.82	48.2	4.2	0.98	4.2
42	2	a ⊥	43.8	25.9	9.04	38.0	6.3	0.87	5.5
43	2	a ⊥	43.8	24.7	10.14	37.1	7.4	0.86	6.3

44	2	a ⊥	43.8	20.0	9.66	33.4	8.7	0.82	7.1
45	2	a ⊥	43.8	20.6	7.03	33.8	6.1	0.82	5.1
46	2	a ⊥	43.8	26.0	7.45	38.0	5.1	0.87	4.5
47	2	a ⊥	43.8	26.4	13.36	38.3			
48	2	a ⊥	43.8	26.8	7.26	38.7	4.9	0.88	4.3
49	2	a ⊥	43.8	34.0	11.07	43.5	5.8	0.93	5.5
50	2	a ⊥	43.8	25.1	8.35	37.4	6.0	0.86	5.2
51	2	a ⊥	43.8	22.6	10.11	35.5	8.0	0.84	6.8
52	2	a ⊥	43.8	25.7	11.69	37.8	8.2	0.87	7.1
53	2	a ⊥	43.8	24.3	10.22	36.8	7.5	0.86	6.5
54	2	a ⊥	43.8	28.1	6.43	39.5			
55	3	a ⊥	43.8	12.4	2.26	26.3			
56	3	a ⊥	43.8	27.1	5.26	38.9			
57	3	a ⊥	43.8	30.5	7.85	41.2	4.6	0.91	4.2
58	3	a ⊥	43.8	28.4	11.32	39.7			
59	3	a ⊥	43.8	27.5	6.60	39.1			
60	3	a ⊥	43.8	23.2	6.04	36.0	4.7	0.85	4.0
61	3	a ⊥	43.8	17.9	11.58	31.5	11.6	0.79	9.2
62	4	a ⊥	43.8	15.5	8.45	29.4	9.8	0.77	7.5
63	4	a ⊥	43.8	25.2	10.26	37.5	7.3	0.87	6.3
64	4	a ⊥	43.8	22.0	14.95	35.0	12.2	0.84	10.2
65	4	a ⊥	43.8	23.4	12.53	36.1	9.6	0.85	8.2
66	4	a ⊥	43.8	23.1	13.10	35.9	10.2	0.85	8.6
67	4	a ⊥	43.8	25.4	14.03	37.6			
68	4	a ⊥	43.8	31.0	13.50	41.6	7.8	0.91	7.1
69	4	a ⊥	43.8	33.0	12.25	42.9	6.7	0.93	6.2

d = diametral	∥ = parallel to foliation
a = axial	⊥ = perpendicular to foliation

Comments: Red font colour indicates an invalid mode of failure. For subsamples consisting of <5, 5-7, and >7 tests, respectively 0, 1 and 2 extreme values on either side are discarded.

Block(s)	Mean $I_{s(50)\perp}$	Mean $I_{s(50)\parallel}$	$I_{a(50)}$
1	8.4	3.2	2.7
2	5.7	1.9	3.0
3	5.8	1.8	3.2
4	7.5	3.1	2.4
1 and 4	8.0	3.1	2.5
2 and 3	5.5	1.8	3.0

Eirik Nilsen

Groundwater Pressure on a Partially Drained Tunnel Lining

NTNU
Norwegian University of
Science and Technology